CHARACTERISTICS OF SUBCRITICAL FLOW IN A MEANDERING CHANNEL

by

Ben-Chie Yen

Project Sponsored
by the
National Science Foundation
under
Grant No. G-18988

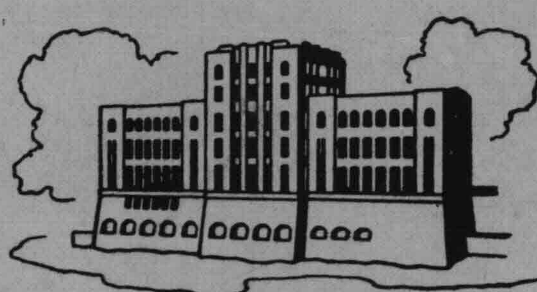

Institute of Hydraulic Research
The University of Iowa
Iowa City

1965

26-E-81

CHARACTERISTICS OF SUBCRITICAL FLOW IN A MEANDERING CHANNEL

by

Ben-Chie Yen

Project Sponsored
by the
National Science Foundation
under
Grant No. G-18988

Institute of Hydraulic Research
The University of Iowa
Iowa City

1965

ABSTRACT

The flow in a meandering channel is complicated by its curvilinear characteristics. Consequently, spiral motion and superelevation develop, and the velocity and boundary-shear distributions are modified. Through an approximate theoretical solution and experiments in a fixed-bed model of constant radius, central angle, and uniform cross section, the influence of the Froude number, and the width-depth ratio of subcritical flow with sufficiently high Reynolds number in a relatively wide meandering channel were determined. The velocity and boundary-shear distributions, the superelevation, and the growth and decay of the spiral motion were studied in detail through analysis of the experimental results. The turbulence intensity of the flow was also measured. Experimental results are presented in generalized form.

ACKNOWLEDGMENTS

During the three-year period of work on this project, the writer received assistance and suggestions from many persons, to whom he would like to express appreciation. Special gratitude is due Professor Hunter Rouse, for his constant advice, attention, and guidance; Professor Lucien M. Brush, Jr., who was initially in charge of the project; and Professor Eduard Naudascher, for his advice and encouragement during the last phase of this study. The writer wishes to thank Mr. C.-L. Yen for his skillful assistance, and Mr. H. W. Tieleman for performing the air-model experiment independently and also for the assistance he gave. Suggestions and critical reviews of the manuscript by Dr. H.-W. Ho, Mr. E. M. O'Loughlin, and Dr. S. R. Singamsetti are greatly appreciated. Thanks are also due Professor P. G. Hubbard and Mr. J. R. Glover for their help in the hot-wire techniques; Messrs. S. Hayat, B. Hunt, and C. Key for their assistance with the drawings; Miss Frieda Sievers for typing the manuscript; and Mr. Dale C. Harris and his shop staff for the construction and maintenance of the experimental equipment. The financial support of the National Science Foundation under Grant No. G-18988 is gratefully acknowledged.

TABLE OF CONTENTS

TABLE OF FIGURES

Figure

I. INTRODUCTION

One of the riddles of nature is the meandering of rivers. The present study is by no means an attempt to give a comprehensive answer to this complicated phenomenon, but to obtain information about flow in an idealized river bend which would be helpful in many practical problems and further research work.

The flow in a curved open channel differs from that in a straight channel because of the presence of centripetal acceleration. As a consequence, the water surface is superelevated, spiral motion may be set up, and the velocity and boundary-shear distributions are modified. Furthermore, the flow characteristics change from section to section unless the bend is relatively long. The effect of the bend extends both upstream and downstream. The bend acts as an obstacle to the flow, causing additional energy losses and a rising backwater upstream. In bends with large curvature, separation may also occur. In natural rivers, the flow is further complicated by irregular channel geometry and movable bed material.

Since the present work is an initial attempt to study the meandering-river problem systematically, the laboratory model is idealized as a fixed-bed channel of uniform cross section of large width-depth ratio with clear-water subcritical flow. In addition to the mean-flow characteristics - namely, velocity, direction of flow, water-surface profiles, and boundary shear stresses - the turbulence intensity was also measured. The experimental results are compared with an approximate theoretical solution for fully developed bend flow.

Because of the difficulties involved in turbulence measurements in water, the possibility of using a double-image type of air model of similar geometry for turbulence study was considered, and the result was compared with that obtained for the water channel.

II. DIMENSIONAL ANALYSIS

In the analysis of flow in a meandering river, the parameters involved can be classified into four groups: the channel-geometry characteristics, the flow characteristics, the fluid properties, and the sediment properties.

The channel-geometry characteristics can in turn be grouped as:

A. Cross-sectional factors, which include the depth h, the width B, and the parameters which describe the shape of the cross section.

B. Planimetric pattern factors, which describe the pattern of the meander.

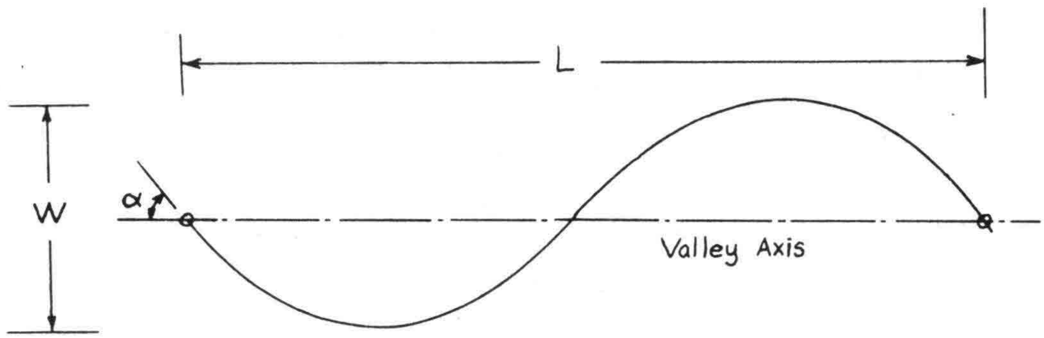

Fig. 1.

These include the amplitude of the meander W, the "wave length" of the meander L, the angle α which the initial tangent at the nodal point makes with the axis of the meander belt, and the radius of curvature of the channel at any distance from the nodal point (Fig. 1).

C. Longitudinal-profile factors, which include the valley slope s_v and the channel-bed slope s_b.

The flow characteristics include the magnitude and direction of the mean velocity at any point, the distribution of pressure, the water-surface profiles, the turbulence characteristics, the flow condition at the entrance, and the gravitational acceleration g.

Obviously, there are too many variables to be handled in a laboratory model study at the present stage. Therefore, sediment was eliminated from the study; clear water was used as fluid; the movable bed was replaced by a surface of specific roughness; the channel was built with a uniform trapezoidal cross section and with bends of constant curvature and reverse directions connected by short tangents. The entrance flow condition was no longer an independent variable, because the flow was considered to be uniquely determined by the preceding bends and was an inverse image of the entrance condition of the following bend.

For this simplified model (Fig. 2), the geometry of the channel can be defined by the central angle of the bend θ_c, the centerline radius r_c, the tangent length T, the width of the channel B, the depth of flow h, and the cross-sectional shape. By using cylindrical coordinates r, θ, and z within the bend, with z measured vertically from the bed, and Cartesian coordinates x, y, and z for the straight tangent, with y along the longitudinal direction as shown in Fig. 2, any one of the local mean-flow velocity components and pressure can be expressed as

$$\bar{u}, \bar{v}, \bar{w}, \bar{p} = F_{1,2,3,4}\left(\rho, \mu, g, \begin{matrix} r, & \theta, & z, \\ x, & y, & z, \end{matrix}\ T, r_c, \theta_c, B, h, \right.$$

$$\left. Q, \text{ cross-section shape}, \text{ roughness} \right) \qquad (1)$$

where $\bar{u}$, $\bar{v}$, and $\bar{w}$, are the temporal mean velocity components at a point along the r, θ, z, or x, y, z directions, respectively; and $\bar{p}$ is the temporal mean pressure at that point. The symbol F represents a functional relationship. The parameters ρ and μ are the density and dynamic viscosity of the fluid, respectively; and Q is the volume rate of flow, or discharge, which is used here instead of the bed slope.

If V_0 and h_0 are the mean velocity and the hydraulic mean depth of uniform flow in a straight channel having the same discharge Q, the same boundary roughness, and the same cross section as the curved channel, then one obtains

$$V_0 = F_5 \, (\rho, \mu, g, B, h_0, R, Q, \text{roughness}) \tag{2}$$

where the shape factor is assumed to be sufficiently described by the hydraulic radius R. Substitution of the functional relationship (2) into (1) and application of dimensional considerations yield the following dimensionless relationships:

$$\frac{\bar{u}}{V_0}, \frac{\bar{v}}{V_0}, \frac{\bar{w}}{V_0}, \frac{\bar{p}}{\rho V_0^2/2} = F_{6,7,8,9} \left[\left(\begin{matrix} \frac{r}{r_c}, \theta, \frac{z}{h_0} \\ \frac{x}{B}, \frac{y}{r_c}, \frac{z}{h_0} \end{matrix} \right), \frac{V_0 R \rho}{\mu}, \right.$$

$$\left. \frac{V_0}{\sqrt{g h_0}}, \frac{T}{r_c}, \theta_c, \frac{r_c}{B}, \frac{B}{h_0}, \frac{B}{R}, \text{roughness} \right] \tag{3}$$

Likewise, the temporal mean boundary-shear stress $\bar{\tau}_0$ is expressed as

$$\frac{\bar{\tau}_0}{\rho V_0^2/2} = F_{10} \left[\left(\begin{matrix} \frac{r}{r_c}, \theta \\ \frac{x}{B}, \frac{y}{r_c} \end{matrix} \right), \frac{V_0 R \rho}{\mu}, \frac{V_0}{\sqrt{g h_0}}, \frac{T}{r_c}, \theta_c, \right.$$

$$\left. \frac{r_c}{B}, \frac{B}{h_0}, \frac{B}{R}, \text{roughness} \right] \tag{4}$$

The term $V_0 R \rho / \mu$ is the Reynolds number $\mathbb{R}$, which indicates the relative importance of inertial effect compared to viscous effects. If the value of $\mathbb{R}$ is sufficiently large, the influence of the change of $\mathbb{R}$ on the flow characteristics is expected to be negligible.

The Froude number $\mathbb{F} = V_0/\sqrt{g h_0}$ describes the relative importance of inertia compared to gravity effects. If $\mathbb{F}$ is greater than unity, the flow is supercritical and characterized by cross waves in the bend [33, Chap. VIII, Sec. D]* [3, Sec. 16-5]. In most natural rivers

*Numbers in brackets refer to the numbers listed in the References.

the flow is subcritical and $\mathbb{F}$ is less than unity. In alluvial channels $\mathbb{F}$ usually ranges from 0.1 to 0.4. The present study is limited to subcritical flow.

One of the important geometric parameters is the width-depth ratio B/h_0. The flow pattern for the case of large width-depth ratio is different from that for a small ratio because of the difference in relative importance of the surface resistance of the bed and that of the banks or side walls. For the case of $B/h_0 \ll 1$, there may be no spiral motion at all, because the side-wall resistance prevents it. However, in river bends the width-depth ratio is much greater than unity, and the bottom contributes the major part of the surface resistance.

For the present study, in order to have a model which would be representative of a natural large river, the geometry of the model channel was based on a statistical analysis of rivers. From the navigation maps published by the Corps of Engineers [25, 26], the planimetric characteristics of the bends in the Mississippi River from Cairo, Illinois, to Baton Rouge, Louisiana, and in the Missouri River from Sioux City, Iowa, to its mouth were measured. Cumulative frequency curves for r_c/B_s, θ_c, and T_1/r_c were obtained (Figs. 3, 4, and 5), where B_s was the water-surface width. The maps used for this analysis were for average low-water conditions. At higher stages, θ_c and T_1/r_c would change presumably little; the values of r_c/B_s, however, would decrease appreciably because of the rapid increase of B_s at higher stage. Because of the variation of B_s with stage, more information was needed to decide the value of r_c/B_s for the model. Leopold and Wolman gave an average value of r_c/B_s of 2.3 for many rivers and canals, and an average value of 3.24 for the few data they obtained for the Mississippi [24]. Based on all this information, with less weight given to the Missouri River data because that river has mostly been trained, the planimetric geometry of the model was chosen as $\theta_c = 90^\circ$, $T_1/r_c = 2.5$, and $r_c/B_b = 4.67$.

III. PREVIOUS WORK ON FLOW IN BENDS

Since Thomson recorded in 1876 [39] the spiral motion in a river bend based on his experimental observation, many investigations have been conducted on flow in bends. However, only a few controlled laboratory experiments have been made for the case of subcritical flow with relatively high Reynolds numbers in open-channel bends of large width-depth ratios. A brief summary of important experiments on flow in open-channel bends is given in Table 1. Most of the values in this Table were computed from the data given in the original publications; the Russian investigations (Milovich and following) were taken from References [19] and [35]. A more detailed description of Russian work can be found in Reference [10].

During the late nineteenth and the early twentieth century, studies on meandering channels were mainly based on field observations of rivers. Fargue [9] systematically summarized his observations of the Garonne since 1849 and proposed his empirical laws on meandering rivers with movable bed which were widely accepted in Europe for river-training works. Leliavsky verified Fargue's laws from field observations by means of a specially designed device for velocity-direction measurements [21]. In 1934, Blue, Herbert, and Lancefield published results of measurements in the Iowa River near Iowa City [1]; and in 1935, Eakin published a study on a bend of the Mississippi [5]. The latter two investigations showed the existence of spiral motion.

Among the analytical and experimental investigations, Böss [2] assumed free-vortex velocity distribution in the radial direction to evaluate analytically the transverse superelevation of the water surface and checked it experimentally. The width-depth ratios of his experiments were too low compared to those of natural rivers and only the transverse water-surface profiles were measured. As will be shown later, the superelevation is not sensitive to the lateral distribution of the longitudinal velocity component if r_c/B of the channel is greater than unity. Thus, the study is interesting only because of its consideration of free-vortex velocity distribution.

Yarnell and Woodward conducted extensive experiments on flow in bends at the Iowa Institute of Hydraulic Research [42]. It was found that the entrance condition was important for the flow in the bend. Near the beginning of the bend, the pressure or water depth decreased and the velocity increased near the inside boundary. The effects of the bend persisted for a considerable distance downstream. Spiral motion was also observed. However, the width-depth ratios for this series of experiments were relatively small and the Froude numbers were high compared to those of alluvial rivers.

Mockmore proposed a theoretical study on flow in open-channel bends by arbitrarily assumed distributions of velocity components [27]; his study showed the streamlines to be helicoidal. He also gave the equations for the streamlines, angular velocities, and accelerations for the free-vortex case. However, his assumed velocity distributions could not be verified experimentally, and hence the result of his study could not be accepted quantitatively.

Shukry presented the results of his experiments [37], which covered a wide range of central angle θ_c, of Froude numbers, and of radius-width ratios. Water-surface profiles were measured to evaluate the resistance coefficient. In several runs he also measured the velocity in magnitude and direction and found that the spiral motion persisted in the straight flume near the curve and that the strength of the spiral is made to decrease by decreasing θ_c, or by increasing either r_c/B or $\mathbb{R}$. The last result is probably due to the relatively low Reynolds numbers tested. It was also stated that the kinetic energy of the lateral currents in a bend is relatively small and that the tangential velocity component and the water-surface profile at the section of maximum surface depression can be predicted by free-vortex theory. The major limitation of Skukry's work is the relatively small width-depth ratio. His conclusion that the strength of the spiral motion decreases as B/h decreases is a consequence of this limitation and is true only for B/h of about unity and smaller. Experimental results by Liatkher and Prudovskii [22] show that the redistribution of velocity, and hence the spiral flow, is most intense when the width-depth ratio is about unity.

The main purpose of a recent experimental investigation at MIT [17, 18] was to determine the boundary-shear distribution. It was found that the flow patterns on a 60° bend are essentially those of free-vortex flow. The maximum boundary shear was generally found at locations of high velocity. The relative boundary-shear patterns were not strongly affected by variations in depth and velocity distribution at the entrance section; they seemed to depend primarily on the channel geometry.

Another group of investigators, such as Raju [31], Yen and Howe [44], Denzler [4], and Shanmugam [36], were interested mainly in the evaluation of the loss coefficient in a bend.

Friedkin performed a series of experiments on the development of meanders in a movable bed [11]. He also observed the trace of the bed material. Leopold and Wolman collected field data and studied the problem from a physiographic point of view [24].

Among Russian investigations, the work of Rozovskii is most noteworthy [35]. With the aid of order-of-magnitude considerations and assumptions about eddy viscosity, vertical distribution of longitudinal velocity components, and zero net lateral discharge, he derived an approximate solution for the radial velocity component from the Reynolds equations of motion. Through further assumptions, he tried to solve for the radial distribution of the longitudinal velocity component and the growth and decay of the spiral motion. Because some of his assumptions are very questionable and cannot be verified experimentally, as will be discussed further in Chapters IV and VII, the results of his attempt are not satisfactory. In order to verify his theoretical study, he performed extensive experiments and field measurements. He concluded that the solution for the vertical distribution of the radial velocity component based on a logarithmic distribution of the longitudinal velocity component along the vertical direction is acceptable, whereas those based on exponential, parabolic, or elliptical velocity distributions have their defects. It is to be noted, however, that the Reynolds numbers for his experiments were generally low, and that the results were valid only for a single bend with uniform approaching flow.

It can be noted that most of the previous experimental studies of flow in open-channel bends have certain shortcomings. Either the Reynolds number is too low to be free from the change of flow pattern due to the change of $\mathbb{R}$; the width-depth ratio is too small as compared to those of natural rivers; or the variation of depth due to a difference between the average surface slope and the bed slope is not negligible. For the few experiments done under favorable conditions, such as those at MIT, only a limited amount of information has been obtained. Therefore, a systematic detailed experimental investigation of flow in a meandering channel having a geometry compatible with that of natural rivers, with relatively high Reynolds numbers and various Froude numbers, is needed and appropriate.

The flow in retangular conduit bends which is closely related to the present subject, has been studied by Wattendorf [41], Hawthorne [12], Eskinazi and Yeh [8], Yeh, Ross and Lien [43], Nippert [28], Richter [32], Eichenberger [6], and Yarnell and Woodward [42]. However, all these studies dealt with the case of small width-depth ratios.

IV. THEORETICAL CONSIDERATIONS

1. Velocity Distribution of Fully Developed Flow in Curved Channel of Large Width-Depth Ratio

In terms of cylindrical coordinates, the Reynolds equations of motion are [34, p. 433]

$$\frac{\partial \bar{u}}{\partial t} + \bar{u}\frac{\partial \bar{u}}{\partial r} + \bar{v}\frac{\partial \bar{u}}{r\partial \theta} + \bar{w}\frac{\partial \bar{u}}{\partial z} - \frac{\bar{v}^2}{r} = -\frac{\partial}{\partial r}\left(\frac{\bar{p}}{\rho} + \Omega\right) + \frac{\partial}{\partial r}\left[\nu\left(\frac{\partial \bar{u}}{\partial r} + \frac{\bar{u}}{r}\right) - \overline{u'^2}\right]$$
$$+ \frac{\partial}{r\partial \theta}\left[\frac{\nu}{r}\left(\frac{\partial \bar{u}}{\partial \theta} - 2\bar{v}\right) - \overline{u'v'}\right] + \frac{\partial}{\partial z}\left(\nu\frac{\partial \bar{u}}{\partial z} - \overline{u'w'}\right) - \frac{\overline{u'^2}}{r} + \frac{\overline{v'^2}}{r} \qquad (5)$$

$$\frac{\partial \bar{v}}{\partial t} + \bar{u}\frac{\partial \bar{v}}{\partial r} + \bar{v}\frac{\partial \bar{v}}{r\partial \theta} + \bar{w}\frac{\partial \bar{v}}{\partial z} + \frac{\bar{u}\bar{v}}{r} = -\frac{\partial}{r\partial \theta}\left(\frac{\bar{p}}{\rho} + \Omega\right) + \frac{\partial}{\partial r}\left[\nu\left(\frac{\partial \bar{v}}{\partial r} + \frac{\bar{v}}{r}\right) - \overline{u'v'}\right]$$
$$+ \frac{\partial}{r\partial \theta}\left[\frac{\nu}{r}\left(\frac{\partial \bar{v}}{\partial \theta} + 2\bar{u}\right) - \overline{v'^2}\right] + \frac{\partial}{\partial z}\left(\nu\frac{\partial \bar{v}}{\partial z} - \overline{v'w'}\right) - 2\frac{\overline{u'v'}}{r} \qquad (6)$$

$$\frac{\partial \bar{w}}{\partial t} + \bar{u}\frac{\partial \bar{w}}{\partial r} + \bar{v}\frac{\partial \bar{w}}{r\partial \theta} + \bar{w}\frac{\partial \bar{w}}{\partial z} = -\frac{\partial}{\partial z}\left(\frac{\bar{p}}{\rho} + \Omega\right) + \frac{\partial}{\partial r}\left[\nu\left(\frac{\partial \bar{w}}{\partial r} + \frac{\bar{w}}{r}\right) - \overline{u'w'}\right]$$
$$+ \frac{\partial}{r\partial \theta}\left(\nu\frac{\partial \bar{w}}{r\partial \theta} - \overline{v'w'}\right) + \frac{\partial}{\partial z}\left(\nu\frac{\partial \bar{w}}{\partial z} - \overline{w'^2}\right) - \frac{\overline{u'w'}}{r} + \nu\frac{\bar{w}}{r^2} \qquad (7)$$

and the continuity equation is

$$\frac{\partial \bar{u}}{\partial r} + \frac{\bar{u}}{r} + \frac{\partial \bar{v}}{r\partial \theta} + \frac{\partial \bar{w}}{\partial z} = 0 \qquad (8)$$

where z being measured vertically from the channel bed; $\bar{u}$, $\bar{v}$, $\bar{w}$, are the temporal means and u', v', w' are the fluctuations of the velocity components in the corresponding r, θ, z directions; $\bar{p}$ is the temporal mean of the pressure, $\nu = \mu/\rho$ is the kinematic viscosity of the fluid, and Ω is the gravitational potential energy per unit mass of the fluid.

For steady, fully developed flow in a curved channel, i.e., in a very long continuous bend such that the flow does not change from section to section, all the derivatives with respect to θ of the temporal mean terms are zero, except that of the pressure and gravitational-potential term, which is a constant since in a fully developed flow the loss of energy is the same for equal increments of θ, or $\partial(\bar{p} + \rho\Omega)/\partial\theta = \rho K$. For the part of the flow which is away from the solid boundaries, if the Reynolds number of the flow is sufficiently high for the viscous stresses to be negligible as compared to the turbulent stresses, the Reynolds equations and the continuity equation can be simplified to yield

$$\bar{u}\frac{\partial \bar{u}}{\partial r} + \bar{w}\frac{\partial \bar{u}}{\partial z} - \frac{\bar{v}^2}{r} = -\frac{\partial}{\partial r}\left(\frac{\bar{p}}{\rho} + \Omega\right) - \frac{\partial \overline{u'^2}}{\partial r} - \frac{\partial \overline{u'w'}}{\partial z} - \frac{\overline{u'^2}}{r} + \frac{\overline{v'^2}}{r} \qquad (9)$$

$$\bar{u}\frac{\partial \bar{v}}{\partial r} + \bar{w}\frac{\partial \bar{v}}{\partial z} + \frac{\bar{u}\,\bar{v}}{r} = -\frac{K}{r} - \frac{\partial \overline{u'v'}}{\partial r} - \frac{\partial \overline{v'w'}}{\partial z} - 2\,\frac{\overline{u'v'}}{r} \qquad (10)$$

$$\bar{u}\frac{\partial \bar{w}}{\partial r} + \bar{w}\frac{\partial \bar{w}}{\partial z} = -\frac{\partial}{\partial z}\left(\frac{\bar{p}}{\rho} + \Omega\right) - \frac{\partial \overline{u'w'}}{\partial r} - \frac{\partial \overline{w'^2}}{\partial z} - \frac{\overline{u'w'}}{r} \qquad (11)$$

$$\frac{\partial \bar{u}}{\partial r} + \frac{\bar{u}}{r} + \frac{\partial \bar{w}}{\partial z} = 0 \qquad (12)$$

Unfortunately, even in this simplified form there are still ten unknowns in these four nonlinear differential equations. Hence additional conditions are necessary if the problem is to be solved at least approximately. However, even if our present knowledge of turbulence could provide rigorous information on the relationship between the turbulent stresses and the mean velocity components, the solution of such highly nonlinear differential equations would still be extremely difficult, if possible at all. Therefore, further approximations and simplifications have to be introduced.

If the channel is assumed to be wide compared to its depth, say $B/h > 10$, and the width of the channel and the radius to be of the same order of magnitude, then from experimental observations, the ratio

$\bar{u}/\bar{v}$ of the radial to the longitudinal velocity component would be of the order of h/r, and the ratio $\bar{w}/\bar{v}$ of the vertical to the longitudinal component would be of the order of (h/r)(h/B) except very close to the banks, where the order of $\bar{w}$ approaches that of $\bar{u}$. As to the turbulent stresses, $\overline{u'^2}$, $\overline{v'^2}$, and $\overline{w'^2}$ are assumed to be of the same order of magnitude, and $\overline{u'v'}$, $\overline{v'w'}$ and $\overline{u'w'}$ as well. From experimental observations, $\overline{v'^2}/\bar{v}^2$ is of the order of $(h/r)(\bar{u}/\bar{v})$, or $(h/r)^2$; and $\overline{u'v'}$ is of the same order or one order less than $\overline{v'^2}$. Therefore, the relative orders of magnitude of the terms in Eqs. (9) and (10) are:

$$O\left[\left(\frac{h}{r}\right)^2\right] + O\left[\left(\frac{h}{r}\right)^3\right] - O\left[1\right] = \left[\frac{r}{\bar{v}^2}\frac{\partial}{\partial r}\left(\frac{\bar{p}}{\rho}+\Omega\right)\right] - O\left[\left(\frac{h}{r}\right)^2\right] - O\left[\left(\frac{h}{r}\right)\right]$$
$$- O\left[\left(\frac{h}{r}\right)^2\right] - O\left[\left(\frac{h}{r}\right)^2\right] \qquad (9')$$

$$O\left[\frac{h}{r}\right] + O\left[\frac{h}{r}\right] + O\left[\frac{h}{r}\right] = \left[\frac{r}{\bar{v}^2}\frac{\partial}{r\partial\theta}\left(\frac{\bar{p}}{\rho}+\Omega\right)\right] - O\left[\left(\frac{h}{r}\right)^2\right]$$
$$- O\left[\frac{h}{r}\right] - O\left[\left(\frac{h}{r}\right)^2\right] \qquad (10')$$

From Eq. (10'), by neglecting terms of the order of $(h/r)^2$, the term $[(\bar{p}/\rho) + \Omega]/r$ is seen to be of the order of $(h/r)(\bar{v}^2/r)$. Thus, the relative order of magnitude of the terms in Eq. (11) is

$$O\left[\left(\frac{h}{r}\right)^2\right] + O\left[\left(\frac{h}{r}\right)^2\right] = O\left[1\right] - O\left[\left(\frac{h}{r}\right)^2\right] - O\left[\frac{h}{r}\right] - O\left[\left(\frac{h}{r}\right)^2\right] \qquad (11')$$

By neglecting the small-order terms, Eqs. (9), (10), and (11) can hence be written as

$$-\frac{\bar{v}^2}{r} = -\frac{\partial}{\partial r}\left(\frac{\bar{p}}{\rho}+\Omega\right) - \frac{\partial\overline{u'w'}}{\partial z} \qquad (13)$$

$$\bar{u}\frac{\partial\bar{v}}{\partial r} + \bar{w}\frac{\partial\bar{v}}{\partial z} + \frac{\bar{u}\bar{v}}{r} = -\frac{\partial}{r\partial\theta}\left(\frac{\bar{p}}{\rho}+\Omega\right) - \frac{\partial\overline{v'w'}}{\partial z} \qquad (14)$$

$$0 = \frac{\partial}{\partial z}\left(\frac{\overline{p}}{\rho} + \Omega\right) \tag{15}$$

From Eq. (15), it is evident that the pressure distribution along any vertical in the flow is hydrostatic and the possible relative percentage error involved is less than h/r. Integrating Eq. (15) with respect to z, and noting that $\partial(\overline{p} + \rho\Omega)/\partial\theta = \rho K$ and $\Omega = gz$, one obtains

$$\frac{\overline{p}}{\rho} + \Omega = \frac{\overline{p}}{\rho} + gz = f(r) + K\theta \tag{16}$$

Since $\overline{p} = 0$ on the water surface, $z = h$, so that

$$\left.\frac{\overline{p}}{\rho}\right|_z = \left.\frac{\overline{p}}{\rho}\right|_z - \left.\frac{\overline{p}}{\rho}\right|_h = g(h-z)$$

Therefore

$$\frac{\partial}{\partial r}\left(\frac{\overline{p}}{\rho} + \Omega\right) = \frac{\partial}{\partial r}\left(\frac{\overline{p}}{\rho}\right) = f'(r) = g\frac{\partial h}{\partial r}$$

or

$$\frac{\partial}{\partial r}\left(\frac{\overline{p}}{\rho} + \Omega\right) = g\, s_r \tag{16'}$$

where $s_r = \partial h/\partial r$ is the slope of the water surface in the lateral direction.

Following Boussinesq's concept of turbulent mixing and neglecting viscous stresses, one can write the turbulent-shear terms in Eqs. (13) and (14) as

$$-\overline{u'w'} = \epsilon_{zr}\left(\frac{\partial \overline{w}}{\partial r} + \frac{\partial \overline{u}}{\partial z}\right) \tag{17}$$

$$-\overline{v'w'} = \epsilon_{z\theta}\left(\frac{\partial \overline{v}}{\partial z} + \frac{\partial \overline{w}}{r\partial\theta}\right) \tag{18}$$

where ϵ_{zr} and $\epsilon_{z\theta}$ are the eddy viscosities in the corresponding planes. Different opinions have been expressed about the mathematical nature of the eddy viscosity. According to Boussinesq, it is a pure scalar. Others considered it a vector. Hinze pointed out [14, p. 20] that it is more reasonable for ϵ to be a tensor of second or higher even order. Since no better information is available, and for the sake of simplicity, ϵ is assumed to be a scalar at a point, i.e., $\epsilon_{zr} = \epsilon_{z\theta} = \epsilon$.

For the present problem, the term $\partial\bar{w}/\partial r$ in Eq. (17) is much smaller than $\partial\bar{u}/\partial z$, and in Eq. (18), $\partial\bar{w}/\partial\theta = 0$. Therefore, by introducing Eqs. (16'), (17), and (18), one can write Eqs. (13) and (14) as

$$-\frac{\bar{v}^2}{r} = -g s_r + \frac{\partial}{\partial z}\left(\epsilon \frac{\partial \bar{u}}{\partial z}\right) \tag{19}$$

$$\bar{u}\frac{\partial \bar{v}}{\partial r} + \bar{w}\frac{\partial \bar{v}}{\partial z} + \frac{\bar{u}\bar{v}}{r} = -\frac{K}{r} + \frac{\partial}{\partial z}\left(\epsilon \frac{\partial \bar{v}}{\partial z}\right) \tag{20}$$

For solving $\bar{u}$, $\bar{v}$, and $\bar{w}$ from Eqs. (12), (19), and (20), further assumptions are needed, because all the velocity gradients and s_r and ϵ are still unknown. For the steady uniform flow in a straight, two-dimensional open channel, the velocity distribution along any vertical is

$$\bar{v} = \bar{v}_h + \frac{\bar{v}_\tau}{\kappa} \ln \frac{z}{h}$$

where $\bar{v}_h$ is the velocity at the surface $z = h$, $\bar{v}_\tau = \sqrt{\bar{\tau}_0/\rho}$ is the temporal mean shear velocity, and κ is the Kármán universal constant. The temporal mean shear stress at any elevation z from the bed in the flow is $\bar{\tau} = \bar{\tau}_0\,[1 - (z/h)]$, and by definition $\bar{\tau} = \rho\epsilon\,(d\bar{v}/dz)$. Therefore,

$$\epsilon = \kappa\, \bar{v}_\tau\, z\, \left(1 - \frac{z}{h}\right) \tag{21}$$

For the fully developed flow in an open-channel bend, it is reasonable to assume that ϵ is not only a function of z but also a function of its relative radial position r/h_0, i.e.,

$$\epsilon = \kappa \bar{v}_\tau F\left(\frac{r}{h_0}\right) z \left(1 - \frac{z}{h}\right) \tag{22}$$

where $F(r/h_0)$ should approach unity as r/h_0 approaches infinity. The corresponding velocity distribution along a vertical, if the relationship $\bar{\tau} = \bar{\tau}_0[1 - (z/h)]$ is still assumed to hold, becomes

$$\bar{v} = \bar{v}_h + \frac{\bar{v}_\tau F}{\kappa} \ln \frac{z}{h} \tag{23}$$

This logarithmic velocity distribution in a bend is by no means as exact as that of the flow in a straight channel, for it will be most likely modified by the transverse velocity components. However, with no better information available, Eq. (23) and the corresponding ϵ will be substituted into Eq. (19) in order to solve for $\bar{u}$.

By order-of-magnitude considerations, $\rho\epsilon(\partial\bar{u}/\partial z)$ is the only appreciable radial component of shear stress, so that $\bar{\tau}_{zr} = \rho\epsilon(\partial\bar{u}/\partial z)$, where $\bar{\tau}_{zr}$ is the temporal mean shear stress acting on a surface perpendicular to z along the r direction. Moreover, the shear stress is approximately zero on the free surface, i.e., $\bar{\tau}_{zr} = 0$ at $z = h$, and $(\bar{\tau}_{zr})_0 = \bar{\tau}_0 \sin\phi$ at the bottom, where ϕ is the angle of deviation from the tangential direction. Thus, integration of Eq. (19) from the bottom to the surface, with $\bar{v}$ from Eq. (23), yields

$$S_r = \frac{1}{gr}\left(\bar{v}_h^2 - 2\bar{v}_h \bar{v}_\tau \frac{F}{\kappa} - 2\bar{v}_\tau^2 \frac{F^2}{\kappa^2}\right) - \frac{\bar{v}_\tau^2}{gh} \sin\phi \tag{24}$$

With the aid of the boundary conditions $\bar{\tau}_{zr} = 0$ at $z = h$ and $\int_{\epsilon \to 0}^{h} \bar{u} dz = 0$ for fully developed curved-channel flow, substitution of Eqs. (22), (23), and (24) into Eq. (19) and integration twice with respect to z yield

$$\bar{u} = \frac{\bar{v}_\tau}{F\kappa} \sin\phi \left(1 + \ln\frac{z}{h}\right) + 2\frac{h}{r}\frac{\bar{v}_h}{\kappa^2} I_1 + \frac{h}{r}\frac{\bar{v}_\tau F}{\kappa^3}\left(I_2 - 2I_1\right) \tag{25}$$

where

$$I_1 = -\int \frac{\ln(z/h)}{1-(z/h)} d\frac{z}{h} + \int_0^1 \int \frac{\ln(z/h)}{1-(z/h)} d\frac{z}{h} d\frac{z}{h}$$

$$= \ln\frac{z}{h} \ln(1-\frac{z}{h}) + \sum_{j=1}^{\infty} \frac{(z/h)^j}{j^2} - 1$$

$$I_2 = \int \frac{\ln^2(z/h)}{1-(z/h)} d\frac{z}{h} - \int_0^1 \int \frac{\ln^2(z/h)}{1-(z/h)} d\frac{z}{h} d\frac{z}{h}$$

The numerical values of I_1 and I_2 for different z/h are plotted in Fig. 6.

In order to solve for the lateral distribution of the tangential velocity component $\overline{v}$, the continuity equation (12) is multiplied by $\overline{v}$ and added to Eq. (20) to yield

$$\frac{\partial r^2 \overline{u}\overline{v}}{r^2 \partial r} + \frac{\partial \overline{v}\overline{w}}{\partial z} = -\frac{K}{r} + \frac{\partial}{\partial z}(\epsilon \frac{\partial \overline{v}}{\partial z})$$

By expressing $\epsilon(\partial\overline{v}/\partial z) = \overline{\tau}_{z\theta}/\rho$, and with the boundary conditions $\overline{\tau}_{z\theta}/\rho = \overline{v}_\tau^{\,2}\cos\phi$ at $z = 0$, $\overline{\tau}_{z\theta} = 0$ at $z = h$, and $\overline{w} = 0$ at $z = 0$ and $z = h$, integration of the above equation with respect to z from the bottom to the surface yields

$$\frac{\partial r^2 \int_0^h \overline{u}\overline{v}\,dz}{r^2 \partial r} = -\frac{Kh}{r} - \overline{v}_\tau^{\,2} \cos\phi \tag{26}$$

By substituting $\overline{u}$ and $\overline{v}$ from Eqs. (23) and (25) and noting that $\int_0^1 I_1 d(z/h) = \int_0^1 I_2 d(z/h) = 0$, $\int_0^1 I_1 \ln(z/h)\, d(z/h) = 0.38$, and $\int_0^1 I_2 \ln(z/h)\, d(z/h) = 0.44$, one obtains

$$\frac{\partial}{\partial r}\left\{h^2 r \frac{\overline{v}_\tau}{\kappa^2}\left[\overline{v}_\tau \frac{r}{h}\sin\phi + 0.76\frac{F}{\kappa}(\overline{v}_h - \overline{v}_\tau\frac{F}{\kappa}) + 0.44\,\overline{v}_\tau \frac{F^2}{\kappa^2}\right]\right\}$$

$$= -Khr - \overline{v}_\tau^{\,2} r^2 \cos\phi \tag{27}$$

As a first approximation, the change of pressure and gravitational potential energy can be assumed equal to the rate at which work is done by the bed shear per unit increment of θ, so that $\overline{v}_\tau^2 \cos\phi = -Kh/r$. Herewith, integration of Eq. (27) gives

$$\overline{v}_\tau r h^2 \left[\overline{v}_\tau \frac{r}{h} \sin\phi + 0.76 \frac{F}{\kappa}(\overline{v}_h - \overline{v}_\tau \frac{F}{\kappa}) + 0.44 \overline{v}_\tau \frac{F^2}{\kappa^2} \right] = c\kappa^2 \qquad (28)$$

where c is the integration constant.

For a steady uniform flow in a two-dimensional straight channel, one has

$$\frac{v_{av}}{\overline{v}_\tau} = \sqrt{\frac{8}{f}} = \frac{1.49}{\sqrt{g}} \frac{h^{1/6}}{n} = m \qquad (29)$$

where v_{av} is the average velocity over a vertical, f is the Weisbach resistance factor, and n is the Manning coefficient. This relationship can be assumed to hold for flow in bends if the radius-width ratio is not too small. The value of m, which indicates the boundary-roughness effects, increases only slightly with r, and its value is of the order of 20.

From Eq. (23), it follows that

$$v_{av} = \int_0^1 \overline{v}\, d\frac{z}{h} = \overline{v}_h - \overline{v}_\tau \frac{F}{\kappa} \qquad (30)$$

Thus, Eqs. (28), (29), and (30) can be solved to give

$$v_{av} = \frac{m\kappa}{h}\left(\frac{r}{h} \sin\phi + 0.76\, m \frac{F}{\kappa} + 0.44 \frac{F^2}{\kappa^2} \right)^{-1/2} \sqrt{\frac{c}{r}} \qquad (31)$$

where c is given by $\int_{\text{inner bank}}^{\text{outer bank}} v_{av} h\, dr = Q$. Combining Eqs. (23), (29), and (30), one has the expression for the vertical distribution of the relative longitudinal velocity component as

$$\frac{\overline{v}}{v_{av}} = 1 + \frac{F}{m\kappa}\left(1 + \ln\frac{z}{h}\right) \qquad (32)$$

With the aid of Eqs. (29) and (30), one obtains from Eq. (25) the solution for the relative radial velocity component

$$\frac{\bar{u}}{V_{av}} = \frac{1}{m\kappa}\frac{h}{r}\left[\frac{r}{h}\frac{\sin\phi}{F}\left(1 + \ln\frac{z}{h}\right) + 2\frac{m}{\kappa}I_1 + \frac{F}{\kappa^2}I_2\right] \tag{33}$$

Rozovskii proceeded in a similar way [35], assuming a logarithmic velocity distribution along a vertical, with ϵ given by Eq. (21), and arrived at

$$\frac{\bar{u}}{V_{av}} = \frac{1}{\kappa^2}\frac{h}{r}\left[2I_1 + \frac{\sqrt{g}}{\kappa C}I_2\right] \tag{33'}$$

where C is the Chézy coefficient. This equation agrees formally with Eq. (33) if the $\sin\phi$ term accounting for the effects of boundary shear is neglected. However, Rozovskii assumed C to be a constant in a bend, while in Eq. (33) m could be a function of r.

In Eq. (33), the second term inside the bracket is much larger than either the first or the last term. Thus it can be seen that $\bar{u}/v_{av}$ is hardly affected by the boundary roughness, and is directly proportional to h/r.

The expression for the relative vertical velocity component corresponding to Eqs. (32) and (33) can be obtained from the continuity relationship, Eq. (12), and Eqs. (31) and (32). Since $\bar{w}$ is relatively small except very near the banks, where the solutions for $\bar{u}$ and $\bar{v}$ are at any rate not valid, a cumbersome and more accurate solution is not worthy. If the terms in Eqs. (31) and (33) containing $\sin\phi$ as well as the terms $\partial F/\partial r$, $\partial m/\partial r$, and $(\partial h^{1/6}/\partial r)$ are neglected, then one has

$$\frac{\bar{w}}{V_{av}} = \frac{h^2}{r^2}\frac{1}{2m\kappa^3}\left(2m\kappa\int I_1\, d\frac{z}{h} + F\int I_2\, d\frac{z}{h}\right) \tag{34}$$

For the completion of the solution for the velocity, the function $F(r/h_0)$ should be known. Unfortunately, only its limiting value of unity is known for reasonably large values of r/h_0. Until further information is available, this function is approximated by F = 1.

From Eq. (31), the longitudinal velocity variation in the radial direction is obtained approximately as proportional to $1/\sqrt{r}$; this disagrees with the free-vortex velocity distribution proposed by Böss and others. It appears to be reasonable that for fully developed turbulent flow in a bend the tangential velocity should vary less with respect to the radius than in the case of potential flow.

It is seen from Eqs. (32), (33), and (34) that, provided the superelevation of the water surface is small compared to the depth of flow, the dimensionless velocity components are only functions of the geometry and boundary roughness, and not a function of the Froude number. It also becomes evident that both $\bar{u}$ and $\bar{w}$ increase as the depth increases or the radius decreases, and that $\bar{u}/\bar{v}$ and $\bar{w}/\bar{v}$ are of the order of h/r and $(h/r)^2$ or (h/r) (h/B), respectively, as assumed earlier.

2. Effects of Side Walls on Fully Developed Flow in a Bend

In the preceding section, the flow was assumed to be far away from the side walls, so that the terms $\partial\overline{u'^2}/\partial r$ in Eq. (9) and $\partial\overline{u'v'}/\partial r$ in Eq. (10) are negligible. Near either bank, the side wall contributes as much resistance to the flow as the bed; therefore, the aforementioned two turbulent-stress terms are no longer negligible. The simplified equations of motion corresponding to Eqs. (13), (14), and (15) are then

$$-\frac{\bar{v}^2}{r} = -gs_r + 2\frac{\partial}{\partial r}\left(\epsilon\frac{\partial\bar{u}}{\partial r}\right) + \frac{\partial}{\partial z}\left(\epsilon\frac{\partial\bar{u}}{\partial z}\right) \tag{35}$$

$$\bar{u}\frac{\partial\bar{v}}{\partial r} + \bar{w}\frac{\partial\bar{v}}{\partial z} + \frac{\bar{u}\bar{v}}{r} = -\frac{K}{r} + \frac{\partial}{\partial r}\left[\epsilon\left(\frac{\partial\bar{v}}{\partial r} - \frac{\bar{v}}{r}\right)\right] + \frac{\partial}{\partial z}\left(\epsilon\frac{\partial\bar{v}}{\partial z}\right) \tag{36}$$

$$0 = \frac{\partial}{\partial z}\left(\frac{\bar{p}}{\rho} + \Omega\right) + \frac{\partial}{\partial r}\left[\epsilon\left(\frac{\partial\bar{w}}{\partial r} + \frac{\partial\bar{u}}{\partial z}\right)\right] + 2\frac{\partial}{\partial z}\left(\epsilon\frac{\partial\bar{w}}{\partial z}\right) \tag{37}$$

In Eq. (37), the two turbulent-stress terms are each of the order of h/r compared to the potential energy and can be neglected. This implies that the pressure distribution along any vertical can still be regarded as approximately hydrostatic. However, one should note that the error involved in neglecting the turbulent stresses is larger near the side walls than in the central region.

It is obvious that Eqs. (35), (36), and (37), together with the continuity equation, cannot give a solution for the velocity components. The eddy viscosity ϵ, which is a function of r as well as of z, is actually an unknown.

Ananyan and Rozovskii [35] both proceeded from Eqs. (35) and (37), neglecting the $\epsilon(\partial\bar{u}/\partial z)$ term in Eq. (37); by introducing a stream function Ψ and assuming ϵ to be a constant everywhere, they obtained

$$\frac{\partial^4 \Psi}{\partial r^4} + 2\frac{\partial^4 \Psi}{\partial r^2 \partial z^2} + \frac{\partial^4 \Psi}{\partial z^4} = \frac{2\bar{v}}{\epsilon}\frac{\partial \bar{v}}{\partial z} \tag{38}$$

Furthermore, Ananyan assumed the distribution of $\bar{v}$ to solve for Ψ, and consequently $\bar{u}$ and $\bar{w}$. He showed that the effect of the wall is a function of B/h; when B/h is equal to 2, this effect extends over the entire cross section. When B/h is 5 or 10, only the central portion of 1/10 or 6/10 of the total width, respectively, is practically unaffected.

Rozovskii assumed that $\bar{v}$ at any radial position in Eq. (38) is equal to $\bar{v}$ at $r = r_c$ and solved the problem numerically. He concluded that the wall effect is limited to only a narrow strip extending one to two depths from either side wall.

Although both solutions are not acceptable - chiefly because of the assumptions concerning ϵ, the variation of $\bar{v}$, and the neglect of the $\epsilon(\partial\bar{u}/\partial z)$ term - their conclusions that the direct wall effect is not important for the central portion of a relatively wide channel are correct as verified experimentally. Therefore, the approximate solution for mean velocity components in the preceding section can be expected to apply except in regions extending about twice the depth from either wall.

Physically, it is due to the side walls that the flow is forced to follow a curved passage. As suggested by Einstein and Harder [7], for a fully developed flow in a bend, the flow consists of two regions, one directly and one indirectly affected by boundary resistance. Following the spiral motion, as the flow approached the outer bank, a boundary layer starts to develop along the outer wall. This boundary layer grows continuously along the bottom of the flow until it approaches the inner wall, where the flow is forced to turn upward and thus the boundary layer is destroyed. This boundary layer occupies only the lower portion of the whole depth. It never extends to the water surface. The upper portion of the cross section, where the flow is directed outward, is only indirectly affected by the solid boundary. The transition from the boundary-layer region to the upper region is gradual and continuous. The boundary-layer development is quite complicated because of the three-dimensional effect and the varying pressure gradient, particularly near the side walls. As a more rapid change of the boundary layer - its growth and decay - occurs near the side walls while in the central region of a section the change is gradual, especially if the channel is relatively wide, one can expect that in the regions close to the side walls Eqs. (13), (14), and (15) are not applicable.

3. Transverse Water-Surface Profiles

The difference in transverse water-surface elevations, usually called superelevation, is described by the equations

$$\Delta h = \int_{r_1}^{r_2} S_r \, dr \tag{39}$$

and

$$S_r = \frac{1}{gh}\left(\int_0^h \frac{\bar{v}^2}{r} dz - \int_0^h \bar{v}\frac{\partial \bar{u}}{r\partial\theta} dz - \bar{v}_\tau^2 \sin\phi\right) = C_r \frac{V_{av}^2}{2gr} \tag{40}$$

the latter of which is obtained from Eq. (61).

For the fully developed flow in a bend with an assumed logarithmic velocity distribution, one obtains from Eqs. (24), (29), (30), and (31)

$$S_r = \frac{V_{av}^2}{gr}\left(1 - \frac{3F^2}{m^2\kappa^2} - \frac{r}{h}\frac{\sin\phi}{m^2}\right)$$

$$= \frac{c\left(m^2\kappa^2 - 3F^2 - \frac{r}{h}\kappa^2\sin\phi\right)}{gh^2r^2\left(\frac{r}{h}\sin\phi + 0.76\,m\frac{F}{\kappa} + 0.44\frac{F^2}{\kappa^2}\right)} \qquad (41)$$

Since the terms containing $\sin\phi$ are relatively small, they can be regarded as approximately independent of r for the purpose of integration. If F and m are also assumed to be approximately constant, then

$$\Delta h = \left.\frac{-c\left(m^2\kappa^2 - 3F^2 - \frac{r}{h}\kappa^2\sin\phi\right)}{gh^2r\left(\frac{r}{h}\sin\phi + 0.76\,m\frac{F}{\kappa} + 0.44\frac{F^2}{\kappa^2}\right)}\right|_{r_1}^{r_2} \qquad (42)$$

or

$$\frac{\Delta h}{(V_{av})_c^2/2g} = 2\frac{r_c}{r}\left.\left(1 - \frac{3F^2}{m^2\kappa^2} - \frac{r}{h}\frac{\sin\phi}{m^2}\right)\right|_{r_1}^{r_2} \qquad (43)$$

where $(v_{av})_c$ is the average longitudinal velocity component over the vertical $r = r_c$.

As it has been pointed out before [18, 37], the superelevation is very insensitive to the radial distribution of the velocity. Therefore, approximate formulas of simple form can be adopted. The simplest form is obtained by assuming $c_r = 1$ in Eq. (40). Substituting $c_r = 1$ into Eq. (39), one has

$$\Delta h \approx \int_{r_1}^{r_2} \frac{V_{av}^2}{gr}\,dr \qquad (39')$$

This equation yields

$$\frac{\Delta h}{V_0^2/2g} = 2\left(\ln\frac{r_2}{r_c} - \ln\frac{r_1}{r_c}\right) \qquad (44)$$

for concentric flow through the bend and uniform radial distribution of velocity with $v_{av} = V_0$;

$$\frac{\Delta h}{(v_{av})_c^2/2g} = \left(\frac{r_c}{r_1}\right)^2 - \left(\frac{r_c}{r_2}\right)^2 \tag{45}$$

for a free-vortex type of velocity distribution with $v_{av}r = c$; and

$$\frac{\Delta h}{(v_{av})_c^2/2g} = \left(\frac{r_2}{r_c}\right)^2 - \left(\frac{r_1}{r_c}\right)^2 \tag{46}$$

for a forced-vortex type of velocity distribution with $v_{av} = cr$.

4. Momentum and Energy Equations

a. Momentum equations

If the stress components are expressed as

$$\begin{aligned}
\bar{\sigma}_r &= -\bar{p} + 2\mu\frac{\partial \bar{u}}{\partial r} - \rho\overline{u'^2} \\
\bar{\sigma}_\theta &= -\bar{p} + 2\frac{\mu}{r}\left(\frac{\partial \bar{v}}{\partial \theta} + \bar{u}\right) - \rho\overline{v'^2} \\
\bar{\sigma}_z &= -\bar{p} + 2\mu\frac{\partial \bar{w}}{\partial z} - \rho\overline{w'^2} \\
\bar{\tau}_{r\theta} &= \mu\left(\frac{\partial \bar{v}}{\partial r} - \frac{\bar{v}}{r} + \frac{\partial \bar{u}}{r\partial \theta}\right) - \rho\overline{u'v'} \\
\bar{\tau}_{zr} &= \mu\left(\frac{\partial \bar{w}}{\partial r} + \frac{\partial \bar{u}}{\partial z}\right) - \rho\overline{u'w'} \\
\bar{\tau}_{\theta z} &= \mu\left(\frac{\partial \bar{v}}{\partial z} + \frac{\partial \bar{w}}{r\partial \theta}\right) - \rho\overline{v'w'}
\end{aligned} \tag{47}$$

then the Reynolds equations (9), (10), and (11) can be written as

$$\rho\left(\bar{u}\frac{\partial\bar{u}}{\partial r} + \bar{v}\frac{\partial\bar{u}}{r\partial\theta} + \bar{w}\frac{\partial\bar{u}}{\partial z} - \frac{\bar{v}^2}{r}\right) = \frac{1}{r}\left[\frac{\partial(r\bar{\sigma}_r)}{\partial r} + \frac{\partial(r\bar{\tau}_{r\theta})}{r\partial\theta}\right.$$

$$\left. + \frac{\partial(r\bar{\tau}_{rz})}{\partial z} - \bar{\sigma}_\theta\right] - \rho\frac{\partial\Omega}{\partial r} \tag{48}$$

$$\rho\left(\bar{u}\frac{\partial\bar{v}}{\partial r} + \bar{v}\frac{\partial\bar{v}}{r\partial\theta} + \bar{w}\frac{\partial\bar{v}}{\partial z} + \frac{\bar{u}\bar{v}}{r}\right) = \frac{1}{r}\left[\frac{\partial(r\bar{\tau}_{r\theta})}{\partial r} + \frac{\partial(r\bar{\sigma}_\theta)}{r\partial\theta}\right.$$

$$\left. + \frac{\partial(r\bar{\tau}_{\theta z})}{\partial z} + \bar{\tau}_{r\theta}\right] - \rho\frac{\partial\Omega}{r\partial\theta} \tag{49}$$

$$\rho\left(\bar{u}\frac{\partial\bar{w}}{\partial r} + \bar{v}\frac{\partial\bar{w}}{r\partial\theta} + \bar{w}\frac{\partial\bar{w}}{\partial z}\right) = \frac{1}{r}\left[\frac{\partial(r\bar{\tau}_{rz})}{\partial r} + \frac{\partial(r\bar{\tau}_{\theta z})}{r\partial\theta}\right.$$

$$\left. + \frac{\partial(r\bar{\sigma}_z)}{\partial z}\right] - \rho\frac{\partial\Omega}{\partial z} \tag{50}$$

which are also the momentum equations in differential form in radial, tangential, and vertical directions, respectively. With the aid of the continuity equation, after multiplying Eq. (49) by r and then integrating over a control volume $\forall$ with surface area S, and applying the Gaussian theorem

$$\int_\forall \frac{1}{r}\left[\frac{\partial(rX)}{\partial r} + \frac{\partial(rY)}{r\partial\theta} + \frac{\partial(rZ)}{\partial z}\right] d\forall = \int_S \left(X\frac{\partial r}{\partial n} + Y\frac{r\partial\theta}{\partial n} + Z\frac{\partial z}{\partial n}\right) dS$$

one obtains

$$\rho\int_S r\left(\bar{u}\bar{v}\frac{\partial r}{\partial n} + \bar{v}^2\frac{r\partial\theta}{\partial n} + \bar{v}\bar{w}\frac{\partial z}{\partial n}\right) dS$$

$$= \int_S r\left(\bar{\tau}_{r\theta}\frac{\partial r}{\partial n} + \bar{\sigma}_\theta\frac{r\partial\theta}{\partial n} + \bar{\tau}_{\theta z}\frac{\partial z}{\partial n}\right) dS - \rho\int_\forall \frac{\partial\Omega}{\partial\theta} d\forall \tag{51}$$

Equation (51) is the angular-impulse-momentum relationship for the volume $\forall$.

With the volume $\forall$ from section $\theta = \theta_0$ to $\theta = \theta$ in a trapezoidal channel of 1:1 side slope, the boundary conditions are:

on the bottom,

$$z = 0$$

$$\frac{\partial r}{\partial n} = \frac{r\partial\theta}{\partial n} = 0 \,, \qquad \frac{\partial z}{\partial n} \approx -1$$

$$\bar{u} = \bar{v} = \bar{w} = \overline{u'^2} = \overline{v'^2} = \overline{w'^2} = 0$$

$$\bar{p} = \rho g h(r, \theta)$$

on the free surface,

$$z = h(r, \theta)$$

$$\frac{\partial r}{\partial n} = -S_r \approx 0 \,, \qquad \frac{r\partial\theta}{\partial n} = S \approx 0 \,, \qquad \frac{\partial z}{\partial n} \approx 1$$

$$\bar{w} = \overline{w'^2} = 0$$

$$\bar{p} = 0 \,, \quad \bar{\tau}_{rz} = \bar{\tau}_{\theta z} = 0$$

on section $\theta = \theta_0$,

$$\frac{\partial r}{\partial n} = 0 \,, \qquad \frac{r\partial\theta}{\partial n} = -1 \,, \qquad \frac{\partial z}{\partial n} \approx 0$$

on section $\theta = \theta$,

$$\frac{\partial r}{\partial n} = 0 \,, \qquad \frac{r\partial\theta}{\partial n} = 1 \,, \qquad \frac{\partial z}{\partial n} \approx 0$$

on the inner bank,

$$\frac{\partial r}{\partial n} = -\cos 45^\circ \,, \qquad \frac{r\partial\theta}{\partial n} = 0 \,, \qquad \frac{\partial z}{\partial n} = -\cos 45^\circ$$

$$\bar{u} = \bar{v} = \bar{w} = \overline{u'^2} = \overline{v'^2} = \overline{w'^2} = 0$$

on the outer bank,

$$\frac{\partial r}{\partial n} = \cos 45^\circ \,, \qquad \frac{r\partial\theta}{\partial n} = 0 \,, \qquad \frac{\partial z}{\partial n} = -\cos 45^\circ$$

$$\bar{u} = \bar{v} = \bar{w} = \overline{u'^2} = \overline{v'^2} = \overline{w'^2} = 0$$

Hence from Eq. (51), by noting that $\partial\Omega/\partial r = 0$, $\partial\Omega/r\partial\theta = gs$, and $\partial\Omega/\partial z = g$, the angular-momentum equation for the flow in a trapezoidal channel with 1:1 side slope can be written nondimensionally as

$$\left.\int_{\frac{r_i - h_i}{r_c}}^{\frac{r_o + h_o}{r_c}} \int_0^{\frac{h}{h_m}} \left(\frac{\bar{v}}{V_0}\right)^2 \frac{r}{r_c}\, d\frac{z}{h_m}\, d\frac{r}{r_c}\right|_{\theta_0}^{\theta}$$

$$= \left.\int_{\frac{r_i - h_i}{r_c}}^{\frac{r_o + h_o}{r_c}} \int_0^{\frac{h}{h_m}} \frac{\overline{\sigma_\theta}}{\rho V_0^2} \frac{r}{r_c}\, d\frac{z}{h_m}\, d\frac{r}{r_c}\right|_{\theta_0}^{\theta} - \frac{r_c}{h_m} \left.\int_{\frac{r_i}{r_c}}^{\frac{r_o}{r_c}} \int_{\theta_0}^{\theta} \frac{\overline{\tau_{\theta z}}}{\rho V_0^2} \left(\frac{r}{r_c}\right)^2 d\theta\, d\frac{r}{r_c}\right|_{\frac{z}{h_m}=0}$$

$$+ \frac{r_c}{h_m}\left[\left.\int_{\frac{r_o}{r_c}}^{\frac{r_o + h_o}{r_c}} \int_{\theta_0}^{\theta} \left(\frac{\overline{\tau_{r\theta}}}{\rho V_0^2} - \frac{\overline{\tau_{\theta z}}}{\rho V_0^2}\right)\left(\frac{r}{r_c}\right)^2 d\theta\, d\frac{r}{r_c}\right|_{\substack{\text{outer}\\ \text{bank}}} - \left.\int_{\frac{r_i - h_i}{r_c}}^{\frac{r_i}{r_c}} \int_{\theta_0}^{\theta} \left(\frac{\overline{\tau_{r\theta}}}{\rho V_0^2} - \frac{\overline{\tau_{\theta z}}}{\rho V_0^2}\right)\left(\frac{r}{r_c}\right)^2 d\theta\, d\frac{r}{r_c}\right|_{\substack{\text{inner}\\ \text{bank}}}\right]$$

$$- \frac{g r_c}{V_0^2} \int_{\frac{\forall}{r_c^2 h_m}} s \frac{r}{r_c}\, d\frac{\forall}{r_c^2 h_m} \qquad (52)$$

where r_i and r_o are the inside and outside radii of the bottom, and h_i and h_o are the water-surface heights over the bed plane at the innermost and the outermost points.

b. Energy equation

The energy equation for turbulent flow in differential form and in terms of cylindrical coordinates is

$$\rho\Big[\bar{u}\frac{\partial}{\partial r}\Big(\frac{\bar{V}^2}{2}+\frac{\overline{V'^2}}{2}\Big)+\bar{v}\frac{\partial}{r\partial\theta}\Big(\frac{\bar{V}^2}{2}+\frac{\overline{V'^2}}{2}\Big)+\bar{w}\frac{\partial}{\partial z}\Big(\frac{\bar{V}^2}{2}+\frac{\overline{V'^2}}{2}\Big)$$

$$+\overline{u'\frac{\partial}{\partial r}\frac{V'^2}{2}}+\overline{v'\frac{\partial}{r\partial\theta}\frac{V'^2}{2}}+\overline{w'\frac{\partial}{\partial z}\frac{V'^2}{2}}$$

$$+\frac{\partial}{\partial r}(\bar{u}\,\overline{u'^2}+\bar{v}\,\overline{u'v'}+\bar{w}\,\overline{u'w'})+\frac{\partial}{r\partial\theta}(\bar{u}\,\overline{u'v'}+\bar{v}\,\overline{v'^2}+\bar{w}\,\overline{v'w'})$$

$$+\frac{\partial}{\partial z}(\bar{u}\,\overline{u'w'}+\bar{v}\,\overline{v'w'}+\bar{w}\,\overline{w'^2})+\bar{u}\frac{\overline{u'^2}}{r}+\bar{v}\frac{\overline{u'v'}}{r}+\bar{w}\frac{\overline{u'w'}}{r}\Big]$$

$$=-\Big[\bar{u}\frac{\partial(\bar{p}+\rho\Omega)}{\partial r}+\bar{v}\frac{\partial(\bar{p}+\rho\Omega)}{r\partial\theta}+\bar{w}\frac{\partial(\bar{p}+\rho\Omega)}{\partial z}\Big]$$

$$-\Big[\overline{u'\frac{\partial p'}{\partial r}}+\overline{v'\frac{\partial p'}{r\partial\theta}}+\overline{w'\frac{\partial p'}{\partial z}}\Big]$$

$$+\mu\Big[\bar{u}\nabla^2\bar{u}+\bar{v}\nabla^2\bar{v}+\bar{w}\nabla^2\bar{w}-\frac{\bar{u}^2+\bar{v}^2}{r^2}+\frac{2\bar{v}}{r^2}\frac{\partial\bar{u}}{\partial\theta}-\frac{2\bar{u}}{r^2}\frac{\partial\bar{v}}{\partial\theta}\Big]$$

$$+\mu\Big[\overline{u'\nabla^2u'}+\overline{v'\nabla^2v'}+\overline{w'\nabla^2w'}+\frac{\overline{u'^2}+\overline{v'^2}}{r^2}+\frac{2}{r^2}\overline{v'\frac{\partial u'}{\partial\theta}}-\frac{2}{r^2}\overline{u'\frac{\partial v'}{\partial\theta}}\Big] \qquad (53)$$

where

$$\bar{V}^2=\bar{u}^2+\bar{v}^2+\bar{w}^2, \qquad \overline{V'^2}=\overline{u'^2}+\overline{v'^2}+\overline{w'^2}$$

and

$$\nabla^2 = \frac{\partial^2}{\partial r^2} + \frac{1}{r}\frac{\partial}{\partial r} + \frac{1}{r^2}\frac{\partial^2}{\partial \theta^2} + \frac{\partial^2}{\partial z^2}$$

In Eq. (53), inside the bracket at the left of the equality sign, the first three terms represent the convection of kinetic energy by the mean motion; the following three terms represent the diffusion of turbulent energy by turbulence; the last six terms are the rate at which work is done by turbulence stresses. At the right of the equality sign, the terms in the first and the second brackets represent the rate at which work is done by the mean and the fluctuating pressure, respectively; the terms in the third and the fourth brackets are the rate at which work is done by the viscous stresses in the mean and the turbulent motion, respectively.

The energy equation (53) can be divided into two parts, one related to the mean motion and the other to the turbulence. The energy equation for the mean motion, which can also be obtained by multiplying the Reynolds equations by the corresponding components of the mean velocity and then by adding the resulting equations, is

$$\rho\Big[\bar{u}\frac{\partial}{\partial r}\frac{\overline{V}^2}{2} + \bar{v}\frac{\partial}{r\partial\theta}\frac{\overline{V}^2}{2} + \bar{w}\frac{\partial}{\partial z}\frac{\overline{V}^2}{2} + \bar{u}\Big(\frac{\partial}{\partial r}\overline{u'^2} + \frac{\partial}{r\partial\theta}\overline{u'v'} + \frac{\partial}{\partial z}\overline{u'w'}\Big)$$

$$+ \bar{v}\Big(\frac{\partial}{\partial r}\overline{u'v'} + \frac{\partial}{r\partial\theta}\overline{v'^2} + \frac{\partial}{\partial z}\overline{v'w'}\Big) + \bar{w}\Big(\frac{\partial}{\partial r}\overline{u'w'} + \frac{\partial}{r\partial\theta}\overline{v'w'} + \frac{\partial}{\partial z}\overline{w'^2}\Big)$$

$$+ \bar{u}\frac{\overline{u'u'}}{r} + \bar{v}\frac{\overline{u'v'}}{r} + \bar{w}\frac{\overline{u'w'}}{r} + \bar{v}\frac{\overline{u'v'}}{r} - \bar{u}\frac{\overline{v'^2}}{r}\Big]$$

$$= -\Big[\bar{u}\frac{\partial(\bar{p}+\rho\Omega)}{\partial r} + \bar{v}\frac{\partial(\bar{p}+\rho\Omega)}{r\partial\theta} + \bar{w}\frac{\partial(\bar{p}+\rho\Omega)}{\partial z}\Big] + \mu\Big[\bar{u}\nabla^2\bar{u}$$

$$+ \bar{v}\nabla^2\bar{v} + \bar{w}\nabla^2\bar{w} - \frac{\bar{u}^2+\bar{v}^2}{r^2} + \frac{2\bar{v}}{r^2}\frac{\partial\bar{u}}{\partial\theta} - \frac{2\bar{u}}{r^2}\frac{\partial\bar{v}}{\partial\theta}\Big] \qquad (54)$$

The energy equation for the turbulent motion is

$$\rho\Big[\bar{u}\frac{\partial}{\partial r}\frac{\overline{V'^2}}{2} + \bar{v}\frac{\partial}{r\partial\theta}\frac{\overline{V'^2}}{2} + \bar{w}\frac{\partial}{\partial z}\frac{\overline{V'^2}}{2} + \overline{u'\frac{\partial}{\partial r}\frac{V'^2}{2}} + \overline{v'\frac{\partial}{r\partial\theta}\frac{V'^2}{2}} + \overline{w'\frac{\partial}{\partial z}\frac{V'^2}{2}}$$

$$- \bar{v}\frac{\overline{u'v'}}{r} + \bar{u}\frac{\overline{v'^2}}{r} + \overline{u'^2}\frac{\partial\bar{u}}{\partial r} + \overline{u'v'}\frac{\partial\bar{u}}{r\partial\theta} + \overline{u'w'}\frac{\partial\bar{u}}{\partial z} + \overline{u'v'}\frac{\partial\bar{v}}{\partial r} + \overline{v'^2}\frac{\partial\bar{v}}{r\partial\theta}$$

$$+ \overline{v'w'}\frac{\partial\bar{v}}{\partial z} + \overline{u'w'}\frac{\partial\bar{w}}{\partial r} + \overline{v'w'}\frac{\partial\bar{w}}{r\partial\theta} + \overline{w'^2}\frac{\partial\bar{w}}{\partial z}\Big]$$

$$= -\Big[\overline{u'\frac{\partial p'}{\partial r}} + \overline{v'\frac{\partial p'}{r\partial\theta}} + \overline{w'\frac{\partial p'}{\partial z}}\Big] + \mu\Big[\overline{u'\nabla^2 u'} + \overline{v'\nabla^2 v'}$$

$$+ \overline{w'\nabla^2 w'} - \frac{\overline{u'^2} + \overline{v'^2}}{r^2} + \frac{2}{r^2}\overline{v'\frac{\partial u'}{\partial\theta}} - \frac{2}{r^2}\overline{u'\frac{\partial v'}{\partial\theta}}\Big] \tag{55}$$

From Eq. (54), with the aid of Eqs. (47), by integrating over a control volume of fluid $\forall$ and applying the Gaussian theorem one obtains the integral form of the energy equation for the mean motion:

$$\int_S \frac{\rho\bar{V}^2}{2}\Big(\bar{u}\frac{\partial r}{\partial n} + \bar{v}\frac{r\partial\theta}{\partial n} + \bar{w}\frac{\partial z}{\partial n}\Big)dS + \mu\int_{\forall}\Big[2\Big(\frac{\partial\bar{u}}{\partial r}\Big)^2 + 2\Big(\frac{\bar{u}}{r} + \frac{\partial\bar{v}}{r\partial\theta}\Big)^2$$

$$+ 2\Big(\frac{\partial\bar{w}}{\partial z}\Big)^2 + \Big(\frac{\partial\bar{u}}{\partial z} + \frac{\partial\bar{w}}{\partial r}\Big)^2 + \Big(\frac{\partial\bar{v}}{\partial r} + \frac{\partial\bar{u}}{r\partial\theta} - \frac{\bar{v}}{r}\Big)^2 + \Big(\frac{\partial\bar{w}}{r\partial\theta} + \frac{\partial\bar{v}}{\partial z}\Big)^2\Big]d\forall$$

$$- \rho\int_{\forall}\Big[\overline{u'^2}\frac{\partial\bar{u}}{\partial r} + \overline{v'^2}\frac{\partial\bar{v}}{r\partial\theta} + \overline{w'^2}\frac{\partial\bar{w}}{\partial z} + \overline{u'v'}\Big(\frac{\partial\bar{v}}{\partial r} + \frac{\partial\bar{u}}{r\partial\theta} - \frac{\bar{v}}{r}\Big)$$

$$+ \overline{u'w'}\Big(\frac{\partial\bar{u}}{\partial z} + \frac{\partial\bar{w}}{\partial r}\Big) + \overline{v'w'}\Big(\frac{\partial\bar{w}}{r\partial\theta} + \frac{\partial\bar{v}}{\partial z}\Big)\Big]d\forall$$

$$= \int_S \Big[(\bar{u}\bar{\sigma}_r + \bar{v}\bar{\tau}_{r\theta} + \bar{w}\bar{\tau}_{rz}) \frac{\partial r}{\partial n} + (\bar{u}\bar{\tau}_{r\theta} + \bar{v}\bar{\sigma}_\theta + \bar{w}\bar{\tau}_{\theta z}) \frac{r\partial\theta}{\partial n}$$

$$+ (\bar{u}\bar{\tau}_{rz} + \bar{v}\bar{\tau}_{\theta z} + \bar{w}\bar{\sigma}_z) \frac{\partial z}{\partial n} \Big] dS$$

$$- \rho \int_S \Omega \left(\bar{u}\frac{\partial r}{\partial n} + \bar{v}\frac{r\partial\theta}{\partial n} + \bar{w}\frac{\partial z}{\partial n} \right) dS \tag{56}$$

If the proper boundary conditions for the present experimental model are substituted, Eq. (56) can be reduced to

$$\int_{r_i-h_i}^{r_o+h_o}\int_0^h \frac{\rho\overline{V}^2}{2}\bar{v}\,dz\,dr\Big|_{\theta_0}^{\theta} - \rho\iiint_{\forall}\Big[\overline{u'^2}\frac{\partial\bar{u}}{\partial r} + \overline{v'^2}\frac{\partial\bar{v}}{r\partial\theta} + \overline{w'^2}\frac{\partial\bar{w}}{\partial z} + \overline{u'v'}\Big(\frac{\partial\bar{v}}{\partial r} + \frac{\partial\bar{u}}{r\partial\theta}$$

$$- \frac{\bar{v}}{r}\Big) + \overline{u'w'}\Big(\frac{\partial\bar{u}}{\partial z} + \frac{\partial\bar{w}}{\partial r}\Big) + \overline{v'w'}\Big(\frac{\partial\bar{w}}{r\partial\theta} + \frac{\partial\bar{v}}{\partial z}\Big)\Big]d\forall + \mu\iiint_{\forall}\Big[2\Big(\frac{\partial\bar{u}}{\partial r}\Big)^2 + 2\Big(\frac{\bar{u}}{r} + \frac{\partial\bar{w}}{r\partial\theta}\Big)^2$$

$$+ 2\Big(\frac{\partial\bar{w}}{\partial z}\Big)^2 + \Big(\frac{\partial\bar{u}}{\partial z} + \frac{\partial\bar{w}}{\partial r}\Big)^2 + \Big(\frac{\partial\bar{v}}{\partial r} + \frac{\partial\bar{u}}{r\partial\theta} - \frac{\bar{v}}{r}\Big)^2 + \Big(\frac{\partial\bar{w}}{r\partial\theta} + \frac{\partial\bar{v}}{\partial z}\Big)^2\Big]d\forall$$

$$= \int_{r_i-h_i}^{r_o+h_o}\int_0^h (\bar{u}\bar{\tau}_{r\theta} + \bar{v}\bar{\sigma}_\theta + \bar{w}\bar{\tau}_{\theta z})\,dz\,dr\Big|_{\theta_0}^{\theta} - \rho\int_{r_i-h_i}^{r_o+h_o}\int_0^h \Omega\,\bar{v}\,dz\,dr\Big|_{\theta_0}^{\theta}$$

Substituting for $\bar{\tau}_{r\theta}$, $\bar{\sigma}_\theta$, and $\bar{\tau}_{\theta z}$ the corresponding viscous and turbulent stresses, and applying order-of-magnitude considerations as in Sec. VI-1, one obtains in integral form the energy equation for the mean flow in a curved channel, nondimensionally, as

$$\int_{\frac{r_i-h_i}{r_c}}^{\frac{r_o+h_o}{r_c}} \int_0^{\frac{h}{h_m}} \frac{1}{2}\left[\left(\frac{\bar{u}}{V_0}\right)^2 + \left(\frac{\bar{v}}{V_0}\right)^2\right] \frac{\bar{v}}{V_0}\, d\frac{z}{h_m}\, d\frac{r}{r_c}\Bigg|_{\theta_0}^{\theta}$$

$$- \frac{r_c}{h_m}\left\{\int_{\frac{\forall}{r_c^2 h_m}} \left[\frac{\overline{u'w'}}{V_0^2} \frac{\partial \frac{\bar{u}}{V_0}}{\partial \frac{z}{h_m}} + \frac{\overline{v'w'}}{V_0^2} \frac{\partial \frac{\bar{v}}{V_0}}{\partial \frac{z}{h_m}}\right] d\frac{\forall}{r_c^2 h_m} + \frac{\nu}{V_0 h_m}\int_{\frac{\forall}{r_c^2 h_m}} \left[\left(\frac{\partial \frac{\bar{u}}{V_0}}{\partial \frac{z}{h_m}}\right)^2 + \left(\frac{\partial \frac{\bar{v}}{V_0}}{\partial \frac{z}{h_m}}\right)^2\right] d\frac{\forall}{r_c^2 h_m}\right\}$$

$$= \int_{\frac{r_i-h_i}{r_c}}^{\frac{r_o+h_o}{r_c}} \int_0^{\frac{h}{h_m}} \frac{g(h-z)}{V_0^2} \frac{\bar{v}}{V_0}\, d\frac{z}{h_m}\, d\frac{r}{r_c}\Bigg|_{\theta_0}^{\theta} - \int_{\frac{r_i-h_i}{r_c}}^{\frac{r_o+h_o}{r_c}} \int_0^{\frac{h}{h_m}} \frac{\overline{v'^2}}{V_0^2} \frac{\bar{v}}{V_0}\, d\frac{z}{h_m}\, d\frac{r}{r_c}\Bigg|_{\theta_0}^{\theta}$$

$$+ \frac{\nu}{V_0 h_m} \frac{h_m}{r_c} \int_{\frac{r_i+h_i}{r_c}}^{\frac{r_o+h_o}{r_c}} \int_0^{\frac{h}{h_m}} \left[\frac{\bar{u}}{V_0}\left(\frac{\partial \frac{\bar{v}}{V_0}}{\partial \frac{r}{r_c}} + \frac{\frac{\bar{v}}{V_0}}{\frac{r}{r_c}} + \frac{\partial \frac{\bar{u}}{V_0}}{\frac{r}{r_c}\partial\theta}\right) + \frac{2\frac{\bar{v}}{V_0}}{\frac{r}{r_c}} \frac{\partial \frac{\bar{v}}{V_0}}{\partial\theta}\right.$$

$$\left. + \frac{r_c}{h_m} \frac{\bar{w}}{V_0} \frac{\partial \frac{\bar{v}}{V_0}}{\partial \frac{z}{h_m}}\right] d\frac{z}{h_m}\, d\frac{r}{r_c}\Bigg|_{\theta_0}^{\theta} - s_c(\theta-\theta_0)\frac{gQ}{V_0^3 h_m} \tag{57}$$

where s_c is the tangential slope along the centerline of the channel. The terms in Eq. (57) represent: the first, the rate of convection of mean kinetic energy by the mean motion; the second, the rate at which energy is lost by the mean flow and gained by the turbulence; the third, the rate at which energy of the mean motion is dissipated directly through viscosity; the fourth, the fifth, the sixth, and the seventh, the cumulative rate at which work is done by the mean pressure, by the turbulent stresses, by the viscous stresses, and by the body force, respectively.

V. EXPERIMENTAL APPARATUS

1. Meandering Channel

In order to have a model with the geometry given in Chapter II, $\theta_c = 90^\circ$, $r_c/B_b = 4.67$, $T_1/r_c = 2.5$, with a trapezoidal cross section of 1:1 bank slope, in which subcritical flow at a sufficiently high Reynolds number could be obtained, the model was built with the following dimensions: $B_b = 6$ ft, $r_c = 28$ ft, and T = 14 ft. Two identical 90° curves of reversed direction were connected by the 14-ft straight reach, so that developed flow was obtained at the exit of the first bend. The general layout of the model is shown in Fig. 7. The channel, which was 116 ft long, was composed of nine reinforced-concrete slabs: two 7-ft straight slabs at the ends, one 14-ft straight slab at the center, and three 30° slabs for each bend. The slabs were supported by 1-1/2-in. screw-jacks embedded in corner pedestals. By turning the screws the slope of the channel could be adjusted. The channel bottom was a layer of 2-in. well-finished cement mortar. The joints were carefully filled with glazing compound. The downstream end of the channel was connected to a tail tank. An adjustable, 6-in.-high tail gate was built at the end of the channel so that backwater could be controlled. Two variable-speed pumps were used to recirculate water from the tail tank through two 10-in. pipelines to the upstream diffuser. Screens of different mesh sizes inserted at the exit of the diffuser, and 3/4-in. steel tubes placed with different spacing 1 ft downstream from the exit of the diffuser, were used for obtaining the desired velocity distribution at the entrance of the first bend. Downstream from the vertical tubes, a wooden grid, 6 ft wide 2.5 ft long and made of 7/8-in bars, was floated on the water surface to suppress the surface waves.

In each of the two 10-in. pipelines, a streamlined artificial contraction was obtained by welding a curved plate over a 4-in. recess cut into the pipe. This contraction, as a flow-measuring device, functions in the same way as a Venturi meter.

Atop each of the channel side walls, stainless-steel rails were mounted to support and guide the movement of a carriage for observer and instruments. An independently supported sensing-probe truss, moving together with the carriage, was so designed that it would always be perpendicular to the channel axis.

2. Instrumentation

A standard Prandtl-type Pitot tube of 3/16-in. outside diameter was adopted for velocity-head and piezometric-head measurements. For Runs 4 and 5, for which the velocity was so low that too much time would have been spent for each reading with the 3/16-in. Pitot, a stainless-steel Prandtl-type Pitot tube of 7/32-in. outside diameter was adopted.

In either case the Prandtl tube was connected to two manometers simultaneously. A water manometer, rigidly fixed to the sensing-probe truss, was read to the nearest 0.001 ft and could be opened to the atmosphere or used as a differential manometer as desired. This manometer was adopted for measuring piezometric head as well as velocity head. When the local velocity head was smaller than 1 in., a more precise manometer was needed. After several attempts, a modified micromanometer with water and n-Heptane (sp. gr. = 0.682 at 20°C) separated by a small volume of air was adopted. With the aid of microscrews the differential head could be read to the nearest 0.001 in. of Heptane (Fig. 9).

A Preston tube connected to the modified micromanometer was used for boundary-shear measurements. The outside and the inside diameters of the tube were 0.125 in. and 0.096 in., respectively. Since the pressure distribution along any vertical was approximately hydrostatic, a 1/8-in. side-hole tube located 1 in. above the Preston tube was used for static-head measurements. The size of the Preston tube was determined from velocity measurements at several critical points of the flow in the model channel to ensure that the tube always lay within the region of the flow where the inner law held. The tube was calibrated in uniform flow in a straight, 3-ft-wide and 90-ft-long tilting flume of comparable boundary roughness - that is, a flume with carefully finished cement-mortar surface. The calibration curve lay between Preston's experimental curve [29] and Hsu's theoretical curve for inside-to-outside diameter ratio 0.77 [15]; it was 5.5% off Preston's curve and 1.3% off Hsu's.

A light-weight thread mounted on a needle at the end of a probe was used for direction measurements. By rotating the probe, the free end of the thread could be made to align itself with another needle placed 1-3/4 in. away from the first needle. When alignment was obtained, the imaginary line drawn between the two needles was the direction of the flow. The averaging of the fluctuation of the direction was made by eye. The measurements were read to the nearest half degree.

For turbulence measurements, two types of hot-wire probe were adopted (Fig. 8). The 90-degree probe was for longitudinal-velocity-fluctuation measurements, and the 45-degree probe was for $\overline{u'v'}$ measurements. The end of each probe was filled with streamlined, well-finished Epoxy, so that it was water tight. The hot-wire was Hytemco wire 0.0007-in. in diameter and was approximately 0.09 in. long. Signals from the probe were sent to a single-channel constant-temperature hot-wire anemometer and in turn to a root-mean-square analyzer. The circuit of the anemometer was only slightly modified from that of Type CAW described in Ref. [16]. The overheating ratio was changed to 7% and a reactance-balance circuit was incorporated to compensate for the capacitor effect of the probe when submerged in water.

One of the most severe problems in hot-wire measurements in water is drift of the reading as the result of foreign particles adhering to the wire and changing its heat-transfer characteristics. Therefore, during the experiments the water was kept very clean and the wire was cleaned with a soft brush before every measurement, using clean water or CCl_4 as cleaning agent.

The accuracy of turbulence measurements depends primarily on the correctness of the calibrations. The calibrations were performed with the wire placed in the potential core of a submerged water jet from a 3/4-in. orifice. Although the water used during the calibrations was very clean, to avoid the effect of drifting, anemometer-current readings were taken 15, 30, and 60 seconds after the probe was put into the flow to detect any drift. The 30-second readings were used to plot the calibration curves, the other two sets of readings serving as a check.

In order that the measurement probes could be placed at any desired point in the flow at any orientation, a slider was mounted on the sensing-probe truss so that it could be moved laterally across the channel. A circular disk with scales of angles marked on it and its axis of rotation on the plane of the truss was attached to the slider. A Lory-type gage fixed to the disk permitted accurate vertical movement to the nearest 0.001 ft. Any one of the probes was fixed to the Lory-type gage. This system was so designed that turning the disk would not change the position of the point of measurement.

VI. EXPERIMENTAL PROCEDURES AND DATA ANALYSIS

In accordance with Eq. (3) from dimensional analysis, with the geometry and boundary roughness adopted for the present model, one can express any flow characteristic, say $\bar{v}/V_0$, as

$$\frac{\bar{v}}{V_0} = F_{11}\left[\left(\begin{matrix} r/r_c, & \theta, \\ x/B_b, & y/r_c, \end{matrix}\ \frac{z}{h_m}\right),\ \mathbb{R},\ \mathbb{F},\ \frac{B_b}{h_m}\right] \tag{58}$$

in which h_m is the average of the elevation of the water surface measured from the channel bottom z = 0 at the midsection of the straight reach. In order to investigate the effects of the width-depth ratio and the Froude number, data were obtained from the following five runs:

Run	h_m ft	h_0 ft	R ft	V_0 fps	B_b/h_m	B_s/h_0	$\mathbb{F}$	$\mathbb{R}/10^5$	s
1	0.353	0.334	0.320	2.68	17.0	20.1	0.82	0.86	0.00144
2	0.502	0.465	0.440	3.14	11.9	15.0	0.81	1.38	0.00144
3	0.512	0.475	0.450	2.27	11.7	14.8	0.58	1.00	0.00072
4	0.515	0.477	0.450	1.40	11.7	14.8	0.36	0.63	0.00029
5	0.751	0.675	0.626	1.73	8.0	11.1	0.37	1.08	0.00029

where $\mathbb{F} = V_0/\sqrt{gh_0}$, in which h_0 was the hydraulic mean depth - the cross-sectional area A divided by the water-surface width B_s - and V_0 was from the discharge divided by A, all computed at the midsection of the straight reach. The Reynolds number was kept at the order of 10^5, which is sufficiently high for the viscosity to play no role in the change of the flow pattern.

In each of the runs, water-surface profile, direction of flow, boundary shear, and velocity were measured, following the order mentioned. The measurements were performed in cross sections at every $\pi/16$-rad increment of θ in the second bend, and at the entrance, the upper quarter, middle, and the lower quarter points of the center-tangent reach; the sections in the bend were named by their angle in radians from the bend entrance, and in the tangent by S0, S1, S2, and S3. In Runs 1, 4, and 5, no velocity and direction measurements were taken at Sections $3\pi/16$ and $5\pi/16$. In Run 1 those at $\pi/16$ and $7\pi/16$ were also omitted, and the water surface was measured at every 10 degress in the second bend. In each section, flow characteristics were measured at ten to fifteen points along each of the seven equally spaced verticals. Moreover, measurements along additional verticals were performed whenever it was felt necessary.

In each of the runs, with the aid of a surveyor's level, the channel was first adjusted to the desired slope by turning the pedestal screws. The deviation of the channel bed from the plane surface following the slope was within ± 0.005 ft and in most cases within ± 0.003 ft. This deviation arose mainly from the uneveness of the cement surface. The channel was then run with flow at a precalculated approximate depth and discharge. The velocity distributions at the entrances of both bends and the depths along the centerline of the channel at every $\pi/16$ rad were measured. This procedure was repeated, by adjusting discharge, depth of flow, and the upstream screens and the steel tubes, until the velocity distributions at the entrances of both bends were simulated as inverse images of each other, as well as the depth of flow at corresponding points of the two curves, after taking account of the unevenness of the bed, were the same. Thus the flow was considered to be established. However, since the spiral motion at the entrance of the first bend could not be simulated, the effect of the entrance condition was checked by running a test with a laterally uniform velocity distribution at the entrance of the first bend. It was found that the velocity distribution at the entrance of the second bend was altered less than $\pm 5\%$ from the simulated flow case. Therefore, it was concluded that the first bend with partially adjusted entrance condition was by itself sufficient to establish developed flow at its exit.

The constancy of the flow condition during a run was checked by readings of discharge meters and three piezometers located along the centerline of the channel (at 0.46 rad in the first bend, at 1.34 rad in the second bend, and at 1 ft upstream from the midsection of the tangent).

Since the boundary roughness is one of the factors that may influence the flow pattern, it is desirable that it be known. However, the channel did not include a straight reach long enough for the evaluation of the resistance coefficient f. Another possible way to compute f is from velocity measurements near the boundary, by assuming that the logarithmic velocity distribution holds, i.e.,

$$\frac{\bar{v}}{V_0} = 2\sqrt{f}\,\log\left(\frac{z}{h}\right) + c \tag{59}$$

where c is a constant. Because of the redistribution of boundary shear in the bend and the energy consumed by the spiral motion, this resistance coefficient varies from point to point as well as with different flow conditions. Therefore, a calculation of f for the flow in bends does not have significance. However, an approximate indication of the surface roughness of the channel was obtained from the average values of f at the midsection of the straight reach. This average f was computed as 0.017 for Run 2 and 0.014 for Run 4. The value of the Manning n of the channel surface was 0.0103.

The water-surface profile was measured with the side holes of the pitot tube. The tube was pointed upstream and set at 0.4 h_m from the channel bottom. It was found from direction measurements that at this depth the flow is very nearly along the tangential direction and consequently the error due to orientation of the Pitot tube is negligible. The results of the water-surface measurements are represented nondimensionally in Figs. 10 and 11.

The direction of flow measured with the thread-needle probe is shown in Figs. 13. Only angles in the horizontal plane were recorded;

ϕ is the angle of deviation from the tangential direction, being positive outward. No device was provided to measure vertical angles, and it will be shown in Sec. VII-1 that they are relatively negligible. The observed angles were then plotted for each vertical, and a faired curve was drawn to be used for velocity and boundary-shear measurements.

No separation of the flow was observed throughout the experiments. In fact, Rozovskii [35] showed that no separation occurred in a 180° open-channel bend of rectangular cross section with $r_c/B = 1$ and $B/h = 13.3$, and the tendency of separation is greater as the depth increases, keeping other factors unchanged. For the same bend just mentioned, separation appeared when $B/h = 5.33$. Therefore with $r_c/B_b = 4.67$ for the present model, no separation should be expected.

The temporal-mean boundary shear was measured by means of a Preston tube resting on the bed. The orientation of the tube was that given by the direction measurements. With the help of the calibration curve, the measured boundary shear was plotted nondimensionally as $\bar{\tau}_0/(\frac{1}{2}\rho V_0{}^2)$ for each cross section and, for the purpose of cross checking, for longitudinal sections as well. The shear contours were then plotted and integrated over the channel boundary to evaluate the average boundary-shear stress over the whole channel $(\bar{\tau}_0)_{av}$. In Fig. 14, $\bar{\tau}_0/(\frac{1}{2}\rho V_0{}^2)$ is plotted longitudinally along the channel, and Figs. 15 show the contours of $\bar{\tau}_0/(\bar{\tau}_0)_{av}$.

For velocity measurements, the Pitot tube was set in a plane parallel to the bed at the angle given by the direction measurements. The local velocity $\bar{V}$ was computed through $\Delta h = \bar{V}^2/2g$, where Δh is the difference in head between the stagnation hole and the side holes. Since $\overline{v'^2}/\bar{V}^2$ was found to be of the order of 0.003, if $\overline{u'^2}$ and $\overline{w'^2}$ are assumed to be of the same order or smaller than $\overline{v'^2}$, the error in neglecting the effects of turbulence in the computation of $\bar{V}$ would be less than 1%. The radial and the longitudinal velocity components were computed by $\bar{u} = \bar{V}\cos\phi$ and $\bar{v} = \bar{V}\sin\phi$. Since $\bar{v}$ was generally not much different from $\overline{V}$ for the present study, only $\overline{V}$ was plotted nondimensionally in Figs. 16. The experimental results of $\overline{u}/V_0$ were plotted in Figs. 17 for different verticals.

In Runs 2 and 3, the root-mean-square values of the longitudinal velocity fluctuation $\sqrt{\overline{v'^2}}$ were measured by means of the 90° hot-wire device described earlier. For Run 2, $\overline{u'v'}$ was also measured by rotating the 45° hot-wire probe through 180° and taking the $+45^\circ$ and -45° readings separately.

With the temporal-mean velocity at a point known from the Pitot-tube measurements, the corresponding mean current through the wire was obtained from the calibration curve. This mean current was maintained during the measurement of turbulence at this point by increasing the sensitivity of the anemometer circuit as the output drifted. It was found that the root-mean-square analyzer gave reliable turbulence readings with this procedure, provided the sensitivity adjustment was within a small range. The values of $\sqrt{\overline{v'^2}}$ and $\overline{u'v'}$ were computed by following the procedures described in Ref. [16].

Since the Hytemco wire adopted was approximately 0.09 in. long and 0.0007 in. in diameter, it was desirable to determine whether this size of wire gave correct turbulence readings. A Wollaston wire (platinum alloy, silver plated) of 0.000197-in. diameter approximately 0.04 in. long with a resistance of 2882 Ohm/ft was adopted for this checking purpose. The Wollaston wire was too thin to be cleaned by brushing; therefore, the water in the channel was specially cleaned for this test run. These two wires of different lengths gave good agreement at all points tested, and thus it was concluded that the Hytemco wire was satisfactory.

As a further check of the sensitivity of both the probe and the anemometer, a wave analyzer together with an RMS analyzer was employed during Run 3 to measure the relative energy spectrum. Both the Hytemco and the Wollaston wires were tested. The result showed that the frequencies of the energy-containing eddies were surprisingly low, mainly of the order of 10 cps. Comparatively, the averaging time of the anemometer was short. This resulted in the unsteadiness of the indicators of the meters, and the mean values of the readings had to be interpreted by naked-eye observations.

Because of the aforementioned drawbacks, the turbulence measurements were repeated two to four times at each point. It was found that the readings were in agreement within $\pm 10\%$, with about two thirds within $\pm 5\%$. The measured turbulence intensity $\sqrt{\overline{v'^2}}/V_0$ was plotted in Figs. 23. Since $\overline{u'v'}$ was evaluated from the difference between two very close values of only two significant figures each, the computed turbulent shear was not reliable. As an illustration, the measurements for $\overline{u'v'}$ at section CIIO for Run 2 are shown in Fig. 24.

VII. DISCUSSION OF RESULTS

1. Spiral Motion

The existence of the spiral motion in a curved channel can be explained as follows. Assuming that at the beginning there is no spiral motion, so that $\bar{u} = \bar{w} = 0$; differentiation of Eqs. (5) and (7) with respect to z and r, respectively, and subtracting the latter from the former, noting that $\eta = (\partial \bar{u}/\partial z) - (\partial \bar{w}/\partial r)$ is the vorticity component on an axis along the tangential direction, one obtains

$$\frac{\partial \eta}{\partial t} = \frac{2\bar{v}}{r}\frac{\partial \bar{v}}{\partial z} - \frac{\partial^2}{\partial r\,\partial z}(\overline{u'^2} - \overline{w'^2}) - \frac{\partial^2 \overline{u'w'}}{\partial z^2} + \frac{\partial^2 \overline{u'w'}}{\partial r^2} + \frac{\partial}{\partial r}\left(\frac{\overline{u'w'}}{r}\right)$$

$$- \frac{\partial^2}{r\partial\theta\partial z}\left(\nu\frac{2\bar{v}}{r} + \overline{u'v'}\right) + \frac{\partial}{\partial r}\left(\frac{\partial \overline{v'w'}}{r\partial\theta}\right) + \frac{1}{r}\frac{\partial}{\partial z}(\overline{v'^2} - \overline{u'^2}) \qquad (60)$$

For potential flow, all the turbulent-stress and the viscous-stress terms drop out; if $\partial\bar{v}/\partial z = 0$, then $\partial\eta/\partial t = 0$; hence the flow is steady and no spiral motion exists. For laminar flow, all the turbulence terms drop out; unless $\bar{v}(\partial\bar{v}/\partial z) = \partial^2(\nu\bar{v})/r\partial\theta\partial z$, $\partial\eta/\partial t$ does not vanish; that is, the flow is unsteady and the spiral motion is growing. For turbulent flow, only for very special conditions that the combination of the values of the eight terms at the right side of the equality sign in Eq. (60) is zero; in general, $\partial\eta/\partial t \neq 0$, the spiral motion must exist.

Besides the consumption of the energy of the flow, the spiral motion modifies the distribution of the velocity. Following the direction of the spiral, high-momentum fluid from the upper flow filaments is transported outward and the low-momentum fluid near the bed is transported inward. However, near the inner wall, the reverse occurs, as will be explained later in this section.

For flow in a bend of large width-depth ratio, the vertical velocity component is much smaller than either the radial or the tangential component except very near the banks. As can be seen intuitively by changing imaginarily the vertical length scale so that the distorted depth would be of the same order as the undistorted width, the distorted vertical velocity would then be of the same order as the undistorted radial velocity component. Since the width is of one order or more larger than the undistorted depth, the undistorted vertical velocity component is expected to be one order smaller than the radial one. This fact is also clearly indicated by Eq. (34). It is primarily because of this reason and the difficulty in experimental technique that the vertical angle of the velocity vector was not measured. Besides, computations from measured velocities showed that, except very near the banks, this vertical angle of streamlines is negligible.

The measured horizontal angle of the velocity vector, which is practically the same as the angle made on a plane parallel to the bed, since the bed slope is small, is shown in Figs. 13; and it indicates clearly the existence as well as the growth and decay of the spiral motion, and the helicoidal shape of the streamlines. This measured direction is the time average of the tangent of the streamlines projected on a horizontal plane. If the measured angles are the same at the corresponding point of two different runs, then the two corresponding streamlines coincide at that point. The experimental results show that the direction of flow at corresponding points for Runs 2, 3, and 4 is in general the same. Thus, when the geometry is the same — that is, the width-depth ratio is a constant and the amount of superelevation is small as compared to the depth — the flow pattern is independent of the Froude number. This can be explained by the fact that, since the pressure distribution along the vertical direction is practically hydrostatic, as long as the flow is subcritical and the value of $\mathbb{F}$ of the flow is not too close to unity, the role of gravity played in this flow is similar to that in closed conduits. This fact provides a basis for the study of flow in bends by using a different fluid, e.g., air, in closed conduits. However, the lack of dependence of the flow pattern upon the Froude number does not actually prevail everywhere in the bend. As indicated by experimental results, the measured directions, and hence the streamlines, do show minor differences at the entrance of the bend, because of the high acceleration effects and the difference in response with respect to adjustment of the water surface, both of which are affected by gravity.

Analytically, in considering the growth and decay of the spiral motion near the entrance or the exit of a bend, the derivatives with respect to θ in Eqs. (5), (6), (7), and (8) no longer vanish. Dropping terms of small order of magnitude as in Sec. IV-1, one can rewrite the equations of motion as

$$\bar{v}\frac{\partial \bar{u}}{r\partial\theta} - \frac{\bar{v}^2}{r} = -\frac{\partial}{\partial r}\left(\frac{\bar{p}}{\rho} + \Omega\right) + \frac{\partial}{\partial z}\left(\epsilon\frac{\partial \bar{u}}{\partial z}\right) \tag{61}$$

$$\bar{u}\frac{\partial \bar{v}}{\partial r} + \bar{v}\frac{\partial \bar{v}}{r\partial\theta} + \bar{w}\frac{\partial \bar{v}}{\partial z} + \frac{\bar{u}\bar{v}}{r} = -\frac{\partial}{r\partial\theta}\left(\frac{\bar{p}}{\rho} + \Omega\right) + \frac{\partial}{\partial z}\left(\epsilon\frac{\partial \bar{v}}{\partial z}\right) \tag{62}$$

$$0 = \frac{\partial}{\partial z}\left(\frac{\bar{p}}{\rho} + \Omega\right) \tag{15}$$

From Eq. (15), once again the condition of hydrostatic pressure distribution is obtained. From Eq. (62), adding the continuity equation (8) multiplied by $\bar{v}$, then integrating with respect to z from the bottom to the surface, and noting that $\bar{w} = 0$ at both $z = 0$ and $z = h$ and that $\rho\epsilon(\partial\bar{v}/\partial z) = \bar{\tau}_{\theta z}$ has the value of zero on the free surface, one obtains

$$\frac{1}{r}\frac{\partial}{\partial r}\left(r^2\int_0^h \bar{u}\,\bar{v}\,dz\right) + \frac{\partial}{\partial\theta}\int_0^h \bar{v}^2\,dz = -h\frac{\partial}{\partial\theta}\left(\frac{\bar{p}}{\rho} + \Omega\right) - r\frac{(\bar{\tau}_{z\theta})_0}{\rho} \tag{63}$$

The counterparts of Eqs. (61) and (63) for the straight reach of the channel, in terms of Cartesian coordinates, are

$$\bar{v}\frac{\partial \bar{u}}{\partial y} = -\frac{\partial}{\partial x}\left(\frac{\bar{p}}{\rho}+\Omega\right)+\frac{\partial}{\partial z}\left(\epsilon\frac{\partial \bar{u}}{\partial z}\right) \tag{64}$$

$$\frac{\partial}{\partial x}\int_0^h \bar{u}\bar{v}\,dz + \frac{\partial}{\partial y}\int_0^h \bar{v}^2\,dz = -h\frac{\partial}{\partial y}\left(\frac{\bar{p}}{\rho}+\Omega\right) - \frac{(\bar{\tau}_{zy})_0}{\rho} \tag{65}$$

Equations (61), (63), (15), (64), and (65) serve as the basic equations for the description of the growth and decay of the spiral motion from a bend. Since their solution is impossible, Rozovskii neglected the potential-energy term in Eq. (64) and assumed that $\bar{u} = \bar{u}_h F_{12}(z/h)$, where $\bar{u}_h$ is the transverse velocity component on the free surface and $F_{12}(z/h)$ is independent of y. Substituting Eq. (33') for $\bar{u}$, he found the decay to be approximately

$$\bar{u} = \bar{u}_0 \exp\left(-2\frac{\kappa\sqrt{g}}{C}\frac{y}{h}\right)$$

where $\bar{u}_0$ is the radial velocity component at the exit y = 0. For the growth of the spiral, he obtained

$$\bar{u} = \bar{u}_0\left[1 - \exp\left(-2\frac{\kappa\sqrt{g}}{C}\frac{r\theta}{h}\right)\right]$$

where $\bar{u}_0$ is the radial velocity component for fully developed flow. Since, first, the centripetal-acceleration term and the potential-energy term are not negligible, and, second, his assumption concerning $\bar{u}$ is not justified, because the lateral discharge $\int_0^h \bar{u}dz$ is not zero in the zone of developing flow, neither of his solutions is acceptable. Moreover, the value of $\bar{u}_0$ in the region of decay and the location of the cross section of $\bar{u}_0$ in the case of growth are both undefined, and actually $\bar{u}$ is not zero at the entrance of the bend $\theta = 0$.

For a meandering channel with bends connected by short tangents, like that of the present study, the growth of the spiral in a bend is strongly affected by the residual spiral from the preceding bend, while the decay of the spiral from the preceding bend is accelerated by the growth of the new spiral.

The relative strength of the spiral motion along the axis of the channel, expressed as $\int_0^{h/h_m} |\bar{u}/V_0| \, d\frac{z}{h_m}$, can be obtained from the sum of the inward and outward dimensionless radial discharges in Fig. 21. It is evident that the spiral from the preceding bend decays very fast in the straight reach because of the absence of a curved boundary and the growth of a reverse spiral due to the following bend. At the midsection of the straight reach, the spiral is only half as strong as at the entrance, while at the exit it is only about one quarter as strong.

The spiral motion of the following bend starts to grow at about the latter quarter of the straight reach. It starts to develop near the water surface a little upstream from the inside bank of the following bend. At the entrance section of the following bend, this new developing spiral motion is still confined to a very small area at the upper inside corner of the section, and its strength is very small in comparison with the decaying spiral motion. However, the pressure gradient on the bed due to the deformed water surface has already reduced the lateral flow of the decaying spiral near the bed, giving rise to the growth of the new spiral. Without the residual spiral motion from the preceding bend, the new spiral would develop much earlier along the inner side in the straight reach.

As the flow enters the bend, the new spiral motion grows rapidly. At Section $\pi/16$, it has already penetrated the whole width of the channel in the bottom region, as well as the upper portion very near the inner bank, while the decaying spiral motion still occupies three quarters of the upper portion of the flow, as sketched in Fig. 20. As the fluid flows farther downstream, the new spiral motion grows continuously and constrains the decaying spiral to an ever-decreasing region at the upper outside corner. While the new spiral motion is still growing at Section $5\pi/16$, the residual spiral motion has practically vanished. From this section on downstream there still exists a small spiral motion with the same sense of rotation as the decayed spiral motion in a very small region in the upper outside corner. Since its strength is constant along the channel, it is believed that this small spiral motion is due to the sidewall corner effect just as that of the secondary current in a straight channel which is essentially a three-dimensional boundary-layer effect.

The main spiral motion in the bend attains the maximum of its relative strength in a region between Sections $3\pi/8$ and $7\pi/16$. Maximum angles of deviation of the velocity vector from the tangential direction occur in the central portion of the cross sections in this region, of about 12° inward on the bottom and about 6° to 8° outward near the surface. Near the exit of the bend, the spiral motion starts to decay, yet at the exit section the spiral motion still has more than 80% of its maximum strength.

From the experimental result that the flow pattern is not a function of the Froude number, it can be reasoned that the spiral motion should also be independent of the Froude number. On the other hand, the direction of flow at the corresponding points varies as the width-depth ratio changes; hence the flow pattern including the growth and decay of the spiral motion is a function of the width-depth ratio. From Fig. 21 it is evident that in the straight reach, although the relative rate of decay of the spiral motion is similar, the strength of the spiral is greater if the width-depth ratio is smaller; this agrees qualitatively with the conclusion drawn from Eq. (33). However, because of different effects due to the residual spiral motion for different geometries, the initial growth of the spiral is faster for greater width-depth ratios. For $B_b/h_m = 17$ and even 12, the rate of growth becomes very slow once Section $\pi/4$ is reached, and the maximum strength occurs near Section $3\pi/8$. For $B_b/h_m = 8$, however, the spiral motion does not reach its maximum strength before Section $7\pi/16$ and thereafter decreases rapidly as the exit of the bend is approached. For the width-depth ratio of 8 the shape of the radial-flow curves in Figs. 21 and 22 indicates that, should the bend be longer, i.e., $\theta_c > 90^o$, the spiral motion would continue to grow. In other words, the bend of the present model is too short for the flow to be fully developed. For smaller depths, $B_b/h_m = 12$ and 17, although the strength of the spirals has not approached a constant and the lateral discharges are not yet zero, as indicated in Fig. 22, the very small variation in the longitudinal direction of both the spiral strength and the lateral discharge indicates that the flow has almost approached the fully developed condition. Moreover, the two curves of lateral discharge for $B_b/h_m = 12$ and 17 in Fig. 22 are similar in shape, except near the entrance of the bend. From Fig. 21 one can see that at corresponding sections the ratio between the spiral strengths for the width-depth ratios of 12 and 17 is between 1.25 and 1.45, which is very close to the ratio of the depths of 1.4. As indicated in Eq. (33), the spiral strength of fully developed flow should indeed be almost proportional to the depth provided r unchanged. Hence it can be concluded that for $B_b/h_m \geqslant 12$ the growth and the decay of the spiral motion in the central region of a cross section become independent of the width-depth ratio and, as a first approximation, the relative strength becomes inversely proportional to the radius-depth ratio.

2. Pressure and Velocity Distributions

a. Pressure distribution

The pressure distribution along any vertical of the flow, as described in Eqs. (15) and (37), is approximately hydrostatic with a possible error of the order of h/r — that is, for the present experimental model, less than 1.5% to 3% of the measured pressure. During the experiments, the pressure distribution was checked at different locations, near either bank as well as near the center, in high-acceleration as well as low-acceleration regions. It was found that, for all runs and locations, the pressure distribution was practically hydrostatic. If there is any deviation of pressure from the hydrostatic, it is much smaller than the variation of pressure due to the fluctuation of the water surface. Hence the conclusion is verified that the pressure distribution along any vertical is hydrostatic when h/r is small.

b. Longitudinal velocity component

Owing to the small deviation of the direction of velocity vectors from the axial direction of the channel, the longitudinal velocity component $\bar{v}$ is practically equal to the total velocity. Even at the position of maximum deviation the error involved in this approximation is less than 3%. Therefore, Figs. 16 and 18 can well be used for the discussion of the variation of $\bar{v}$.

As shown in Fig. 18, the radial distribution of the average longitudinal velocity v_{av} over a vertical is fairly uniform at the entrance section of the straight reach, and this is a very good inverse image of the average velocity distribution at the exit section of the following bend. As the flow enters the straight reach, the water near the bank adjoining the outside of the following curve decelerates, while the water near the opposite bank flows faster. This is primarily due to the residual spiral motion from the preceding curve and is indicated clearly by the longitudinal slope of the water surface. As the following bend is approached, this adjustment of velocity distribution is furthered by the acceleration of the fluid near the inner side of that bend. At the entrance section of the following bend, the radial distribution of v_{av} follows approximately that of a free vortex, i.e., $V \backsim 1/r$, from the centerline of the section to almost the inner bank, while in the outer half of the section the velocity varies more rapidly than the inverse proportionality requires. This increase of v_{av}/V_0 near the inner bank continues until a region between Sections $\pi/16$ and $\pi/8$ is reached, where the radial distribution of the velocity varies more rapidly than that of a free vortex, and the maximum v_{av} is equal to $1.24V_0$. From

Section $\pi/8$ on downstream, the maximum v_{av} of a section gradually shifts outward. The close relationship between the water-surface slope and the distribution of velocity is noteworthy. Downstream from Section $3\pi/8$, the effect on the flow of the exit of the bend is no longer negligible; the depth of flow near the inner bank starts to increase. From Section $7\pi/16$ on downstream the depth decreases near the outer bank; thus the local surface slope increases, and the radial distribution of the average velocity is readjusted rapidly. At the exit section of the bend, this distribution of v_{av} is fairly uniform. Although the maximum v_{av}/V_0 of a section shifts from the inside half of the channel at the entrance of the bend to the outside half at the exit the average velocity v_{av} at center-line verticals remains almost constant, varying from $1.04V_0$ in the straight reach to $1.06V_0$ in the downstream half of the bend.

The foregoing discussion is obtained from Run 3 with $B_b/h_m = 12$ and $\mathbb{F} = 0.58$. However, the same has been found to be true for different Froude numbers. As the width-depth ratio decreases, v_{av}/V_0 tends to be slightly higher near the central region of the channel and lower near the banks, owing to the stronger spiral motion and the relatively higher bank resistance; yet qualitatively the discussion in the preceding paragraph still holds.

The lack of dependence of the relative velocity v_{av}/V_0 upon the Froude number is justified by the following analytical consideration. The integration constant c in Eq. (31) is given by

$$Q = AV_0 = \int_{r_i-h_i}^{r_o+h_o} h\,v_{av}\,dr = \int_{r_i-h_i}^{r_o+h_o} \frac{m\kappa}{\sqrt{\frac{r}{h}\sin\phi + 0.76m\frac{F}{\kappa} + 0.44\frac{F^2}{\kappa^2}}}\sqrt{\frac{c}{r}}\,dr$$

where V_0 is the average velocity over the sectional area A at the mid-section of the straight reach. Then Eq. (31) can be written as

$$\frac{v_{av}}{V_0} = \frac{Am\kappa}{h\sqrt{\frac{r}{h}\sin\phi + 0.76m\frac{F}{\kappa} + 0.44\frac{F^2}{\kappa^2}}}\,\frac{1}{\sqrt{r}} \Bigg/ \int_{r_i-h_i}^{r_o+h_o} \frac{m\kappa}{\sqrt{\frac{r}{h}\sin\phi + 0.76m\frac{F}{\kappa} + 0.44\frac{F^2}{\kappa^2}}}\,\frac{dr}{\sqrt{r}}$$

Assuming that as an approximation, the product mk is a constant and the quantities under the square-root signs cancel each other, one obtains

$$\frac{v_{av}}{V_0} \approx \frac{A}{h}\frac{1}{\sqrt{r}} \Bigg/ \int_{r_i-h_i}^{r_o+h_o} \frac{dr}{\sqrt{r}} = \frac{A}{h}\frac{1}{\sqrt{r}} \frac{1}{2(\sqrt{r_o+h_o} - \sqrt{r_i-h_i})}$$

In this equation only h is affected by the Froude number. However, if the superelevation is small compared to the depth of flow, then h is approximately constant. Hence v_{av}/V_0 is, as a first approximation, not a function of Froude number. Moreover, because $A = h_m(B_b + h_m)$ and $h_m \approx h$, this same equation shows that v_{av}/V_0 is only slightly affected by the width-depth ratio, provided B_b/h_m is large, as verified experimentally. The same — that the lack of dependence upon $\mathbb{F}$ and that only slightly affected by B_b/h_m — is true for $\bar{v}/V_0$.

The radial variation of v_{av}/V_0 as predicted by Eq. (31) is plotted as a short dashed line at Section 5 π/16 on Fig. 18. The integration constant is eliminated by making the measured v_{av}/V_0 at the centerline vertical equal to that of Eq. (31). The justification for this procedure is that Eq. (31) is not valid near the banks. The agreement between the measured and the predicted distributions of v_{av}/V_0 is only fair. This is to be expected, because Eq. (31) applies to the case of fully developed flow in a bend, which was not attained in the present experiment.

In Sec. IV-1, the vertical distribution of the longitudinal velocity component was assumed to follow a logarithmic law. But due to the lateral momentum transfer brought about by the spiral motion it is not possible for every vertical to have logarithmic distribution, even in a region far away from the banks. Although a better approximation could probably be obtained numerically by successive approximations using the continuity relationship, once the first approximation is given by Eqs. (32) and (33), it is always worthwhile to check this variation of $\bar{v}/V_0$ along verticals experimentally. As shown in Figs. 16, the vertical distribution of $\bar{v}/V_0$ changes from vertical to vertical as expected. In every cross section, there is always a vertical near the central region on which $\bar{v}$ varies approximately according to the logarithmic law. In the neighborhood of this vertical, the velocity deviates slightly from the logarithmic distribution, and the deviation is a maximum near the surface. For inner regions, the velocity near the surface is smaller than that predicted by the logarithmic law, and the maximum $\bar{v}$ along a vertical occurs at ever greater depths as r decreases. At $r/r_c = 0.90$, which is not far from the inner bank, the maximum velocity occurs at about mid-depth; this rapid decrease of the velocity near the surface is clearly due to the spiral motion, by which the low-velocity fluid is carried upwards to the water surface. Near the outer bank, the point of maximum $\bar{v}$ again moves downwards from the water surface; however, because of the supply of high-momentum fluid from the central region by the main spiral motion, the decrease of the velocity near the surface is smaller than that near the inner bank. Adjacent to the entrance of the bend, around $r/r_c = 0.9$, the velocity near the surface, rather than decreasing as in the downstream part of the bend, becomes nearly constant because of the acceleration of the flow adjacent to the inner bank; while near the opposite bank the surface velocity is further reduced because of the strongly decaying spiral motion.

The trace of the maximum surface velocity is almost the same as that of the maximum v_{av}; in the downstream half of the bend the former is slightly closer to the outer bank. The trace of the maximum velocity near the bottom in the downstream half of the bend is much closer to the inner bank than v_{av}. This difference in traces of the maximum velocity at different depths is explained by the momentum transfer due to the spiral motion.

Very near the bottom, the viscous effect is more dominant than the effect of the width-depth ratio or the Froude number; thus locally the Reynolds number should be expected to be the most significant parameter to show the variation of the velocity. A plot of the velocity distribution near the bed along the central vertical of the midsection S2 of the straight reach for different runs is shown in Fig. 19 in terms of $z\bar{v}_\tau/\nu$ vs. $\bar{V}/\bar{v}_\tau$. Velocity variations near the bed for several other verticals along the centerline of the channel for Run 3 are also shown in this figure. The experimental points agree well with the data obtained by Smith and Walker for flat plates [38]. In the present experiment, if a viscous sublayer exists, its thickness would range from 0.00035 ft to 0.0007 ft, or $0.0007h_m$ to $0.0014h_m$, when $\delta\bar{v}_\tau/\nu$ is assumed to be equal to 4. The thickness of the transition zone of the boundary layer, by taking $z\bar{v}_\tau/\nu = 30$, ranges from 0.0025 ft to 0.0055 ft, or approximately $0.005h_m$ to $0.011h_m$. However, measurements were not made close enough to the bed to verify the existence of a viscous sublayer. Furthermore, by taking $z\bar{v}_\tau/\nu = 200$ as the upper limit of validity of the inner law, the corresponding thickness of the inner-law region is 0.017 ft for Run 2 and 0.036 ft for Run 4, or approximately $0.03h_m$ to $0.08h_m$ for all five runs. Since this thickness is small and the velocity in this inner-law region is relatively low, the effect on the velocity distribution of the change of thickness of the inner-law region due to different B_b/h_m or $\mathbb{F}$ is negligible over the whole depth. Nevertheless, when the Reynolds number is of the order of 10^4 or smaller, this viscous effect is expected to be no longer negligible; and the flow pattern will be a function of the Reynolds number as well.

c. Radial velocity component

The experimental results of the variation of the relative radial velocity component $\bar{u}/V_0$, which illustrate clearly the growth and decay of the spiral motion, are shown in Figs. 17. The variation of this radial velocity component is closely related to the variation of the spiral motion described in Sec. VII-1. For the width-depth ratios of this experimental study, the radial velocity component is one order smaller than the longitudinal one.

Since the measured direction and magnitude of the total velocity are not functions of the Froude number except in the region near the inner bank from Section S3 to Section $\pi/16$ and over most of the section $\pi/16$ where the acceleration effects are dominant, $\bar{u}/V_0$ is evidently not a function of $\mathbb{F}$. This lack of dependence on $\mathbb{F}$ of $\bar{u}/V_0$ agrees with the prediction of Eq. (33). However, Eq. (33) predicts $\bar{u}/V_0$ to be proportional to h/r, whereas experimentally this is roughly verified only at the vertical $r/r_c = 0.90$ in Section $3\pi/8$; this poor agreement is probably due to the fact that the bend is too short to have a fully developed flow for which Eq. (33) is applicable. Nevertheless, the experimental results show that in the downstream half of the bend as well as in the straight reach the relative radial velocity is smaller, the larger the width-depth ratio, which agrees qualitatively with the theoretical prediction.

The relative radial velocity component predicted by Eq. (33) is plotted for the central region verticals at Section $5\pi/16$. It is seen that except very near the bottom and the surface, the shape of the predicted curves agrees with that of the experimental curves. But in general, Eq. (33) gives a smaller algebraic value of the radial velocity component. Once again, this is explained by the fact that the flow is not fully developed. At these verticals, the net discharge is outward. If one of the integration constants in solving for Eq. (33) is evaluated by setting $\int_0^h \bar{u}dz$ equal to the actual lateral discharge instead of zero, the agreement between the experimental and theoretical results would be much better; and Eq. (33) can be used as a first approximation to predict the relative velocity component of the flow in a bend.

d. Lateral discharge

In Sec. IV-1 the theoretical analysis is based on fully developed bend flow and consequently on the condition $\int_0^h \bar{u}dz = 0$. Since there is neither a section with zero lateral discharge nor flow characteristics independent of θ in the present experimental study, it is clear that the bend is too short for such a fully developed flow to be established. As discussed earlier, the trace of maximum v_{av} moves from the inside outward in a bend; in accordance with continuity considerations, a net lateral transport of fluid must exist. This lateral discharge can be evaluated by integration of the radial velocity component over an area on the tangential plane. The integration of $\bar{u}/V_0$ over centerline verticals is shown separately in Fig. 21 for radially outward and inward flow. The radially outward flow is subtracted from the radially inward flow at the same location and the resulting net rate of lateral discharge per unit length along the longitudinal direction is shown in Fig. 22. The lateral discharge is zero for a centerline around $\pi/32$ rad in the bend, while through other verticals in this cross section the net rate of lateral volume transfer is not zero. From Section $\pi/32$ on downstream, the lateral discharge through the centerline section is increasing almost up to the exit of the bend. Then it starts to decrease as the flow approaches the straight reach, and the maximum v_{av} moves across the centerline to the outer half of the channel. For B_b/h_m equal to 12 and 17, the curves in Fig. 22 are similar in shape as discussed in Sec. VII-1; the relative net lateral discharge is larger for smaller width-depth ratios. For $B_b/h_m = 8$, the net relative lateral discharge increases more rapidly in the downstream part of the bend as compared to that for $B_b/h_m = 12$ and 17, yet its magnitude is between those of the latter two width-depth ratios, which indicates that the behavior of the flow for $B_b/h_m = 8$ is different from that of smaller relative depths as discussed in Sec. VII-1.

3. Water-Surface Profiles

As the flow is curvilinear in a channel bend, the water surface is higher at the outside of the bend than at the inside. The measured transverse water-surface profiles are represented nondimensionally in Figs. 10. In the middle half of the tangent section, the water surface is practically horizontal in the transverse direction. For a flow approaching the bend from a long straight channel, the acceleration due to the geometry causes higher velocity near the inner bank as well as curved streamlines and thus superelevation starts to develop far upstream from the entrance of the bend. However, in the present model, since the flow from the preceding bend has already shifted the high-velocity fluid near the inner bank, the superelevation at the entrance section is not very large, and the sloping water surface does not extend very far into the tangent. As soon as the fluid enters the bend, the boundary confines the flow and the superelevation develops quickly. At Section $\pi/32$, the superelevation is almost fully developed, and the water surface is convex. At Section $\pi/8$, the water surface attains its maximum curvature; from this section on downstream, the transverse water-surface profile tends to approach a sloping straight line. At Section $3\pi/8$, the transverse surface slope s_r is already a constant, and the superelevation starts to decrease. At the exit of the bend, the water surface is slightly concave, and the superelevation is reduced to approximately one half of its maximum value in the bend. This change of shape of the water surface and the superelevation at different sections is evident from Eq. (39'). For sections in the bend near its entrance, high-velocity fluid is close to the inner bank where r is small; hence a convex water surface is expected. Farther downstream, the high-velocity fluid gradually shifts towards the outer bank; thus the curvature of the surface gradually decreases until Section $3\pi/8$, where the slope is practically a constant. Farther downstream, the low-velocity fluid near the inner bank and the high-velocity fluid in the central region of the section cause the surface to be concave.

The expressions for the transverse water-surface profile obtained analytically in Sec. IV-3 are plotted in Fig. 12 for the case of $(v_{av})_c/V_0 = 1.05$ by making the water surface for the different expressions coincided at $r/r_c = 1$. From Eq. (43), with the aid of data of Run 3 and by assuming $F = 1$, a convex transverse surface of hyperbolic shape is obtained. The transverse surface profiles predicted by a uniform velocity distribution, Eq. (44), and by a free-vortex velocity distribution, Eq. (45), are also convex in shape; the former has a smaller curvature, and the latter has a larger curvature, respectively, as compared to that predicted by Eq. (43). The profiles predicted by Eq. (44), with $r/r_c < 1$, and by Eq. (45), with $r/r_c > 1$, are very close to that predicted by Eq. (43), provided r/r_c does not deviate much from unity. The transverse surface profile predicted by a forced-vortex velocity distribution is a concave parabola. In spite of the differences in the shape of the water surface, the superelevations between the inside and the outside bank predicted by the four equations are in agreement within 2% of Δh.

Comparing the analytical to the experimental results, one sees that Eqs. (43) and (44) fit very well with the measured surface from Section $\pi/8$ to $5\pi/16$, while Eqs. (45) and (46) can be used as an approximation. However, from Section $5\pi/16$ to $7\pi/16$, Eqs. (43) and (44) can only be used as approximations. From Section $7\pi/16$ on downstream, none of the equations is applicable, because of the decrease of curvature of the streamlines.

It is seen from Figs. 10 that, for the ranges of $\mathbb{R}$ and $\mathbf{F}$ tested, the relative superelevation, $(h - h_m)/V_0{}^2/2g)$, is only a function of location, but not of either the Froude number or the width-depth ratio of the flow. This fact can be justified analytically by modifying Eq. (43), noting that $h_m \approx h_c$ where h_c is the depth at $r = r_c$, to yield

$$\frac{h - h_m}{V_0^2/2g} = 2\,\frac{(V_{av})_c^2}{V_0^2}\,\frac{r_c}{r}\left(1 - \frac{3F^2}{m^2k^2} - \frac{r}{h}\,\frac{\sin\phi}{m^2}\right)\Bigg|_r^{r_c}$$

The value of the terms in the parenthesis is approximately unity. Moreover, as has been discussed in Sec. VII-2, a change of width-depth ratio does not change the distribution of v_{av}/V_0 appreciably; neither does the Froude number, provided the ratio of the total superelevation to the depth, $\Delta h/h$, is small. As a consequence, the relative superelevation is uniquely determined by the location in the bend.

From Fig. 11 it is seen that the nondimensional longitudinal profiles of $(h - h_m)/(V_0^2/2g)$ are, within the experimental accuracy, a function of neither the Froude number nor the width-depth ratio. The centerline water surface is almost parallel to the bed, except around the entrance of the bend, where it is depressed slightly. Because the flow characteristics in a bend are the inverse image of those in the following bend, the longitudinal water-surface profile along $(r_c + \Delta r)/r_c$ at Section $\pi/2$ can be followed continuously by the longitudinal water surface along $(r_c - \Delta r)/r_c$ at Section S0 $(y/r_c = -0.5)$, which is the entrance section of the straight reach of the following bend.

It should be noted here that, in spite of the variation of the depth, the water surface is always sloping downstream in the longitudinal direction. At rising depths the slope is flatter and at falling depths the slope is steeper.

4. Boundary-Shear Distribution

The measured variation of $\bar{\tau}_0/(\frac{1}{2}\rho V_0^2)$ along the longitudinal direction for different r/r_c is shown in Fig. 14. The boundary shear contours of $\bar{\tau}_0/(\bar{\tau}_0)_{av}$, where $(\bar{\tau}_0)_{av}$ is the overall average boundary-shear stress of the whole channel, are shown in Figs. 15. The measured boundary shear is a vector and its direction can be found from Figs. 13.

As has been discussed earlier, the flow pattern is independent of the Froude number, provided $\mathbb{F}$ is smaller than and not too close to unity and the nondimensional geometry remains unchanged. Consequently, the ratio of boundary shear force to inertia force $\bar{\tau}_0/(\frac{1}{2}\rho V_0^2)$ should also be independent of $\mathbb{F}$. The experimental results of Runs 2, 3, and 4 verify this. On the other hand, the change of width-depth ratio slightly alters the distribution of boundary shear, corresponding to the change in flow pattern, as shown in Figs. 15.

The trace of maximum boundary shear, starting from the downstream quarter section S3 of the straight reach, is located on the bed very near its junction with the inner bank. This trace follows almost a circular arc with its center coinciding with the center of the bend until Section $5\pi/16$, downstream from which the trace moves outward gradually with decreasing magnitude of the boundary shear stress. At the exit section of the bend, the point of maximum boundary shear is slightly inside the centerline of the section, where the boundary shear distribution is fairly uniform across the section. In the following first quarter of the straight reach, the trace of maximum boundary shear shifts abruptly to the other side of the channel, followed by the high-shear region of the next bend. Since the boundary shear stress is proportional to the velocity gradient at the boundary, i.e., $\bar{\tau}_0 = \mu(\partial \bar{V}/\partial z)_{z=0}$, the redistribution of the boundary shear is closely related to the velocity distribution discussed in Sec. VII-2.

In Sec. VI-1, it is assumed that $v_{av}/\bar{v}_\tau = 1.49h^{1/6}/\sqrt{g}\, n = m$. Since both $h^{1/6}$ and n are nearly constant, m should also be approximately a constant. Whether this is actually true is checked experimentally. For Run 3, with $h_m = 0.512$ ft and $n = 0.0103$, the computed m is 23.2. The experimental values of the ratio $v_{av}/\bar{v}_\tau$ vary from 20.5 to 24.1, being higher near the inner bank around the entrance of the bend, and lower near the inner bank of the downstream half of the bend and near the outer bank around the bend entrance. The average value of $v_{av}/\bar{v}_\tau$ is 22.5. Thus as a first approximation, $v_{av}/\bar{v}_\tau = m$ can be regarded as a constant.

Despite the fact that high boundary shear prevails near the inner bank, it has been observed in natural rivers as well as in some models with movable bed that scour occurs at the outer bank. This is mainly due to the orientation of the boundary shear stresses. At the inner bank, although the shear is high, the spiral motion is in a direction that stabilizes the bank. At the outer bank, the spiral motion has a downward direction and thus helps to carry bed material away. Because of the existence of the residual spiral from upstream, in the first three quarters of the bend the orientation of the boundary shear also helps to stabilize the outer bank. Near the exit of the bend, the boundary shear stress is not only higher than elsewhere on the outer bank, but also directed downwards; hence this is the location most seriously exposed to scour.

5. Turbulence

The measured root-mean-square values of the fluctuation of the longitudinal velocity component for $B_b/h_m = 12$ are shown nondimensionally in Figs. 23. Since the magnitude of V_0 is very close to that of the average velocity over any cross section in the channel, $\sqrt{\overline{v'^2}}/V_0$ can be regarded as the turbulence intensity relative to the average velocity. In general, the turbulence intensity approaches a constant near the surface with a value of 3 to 4%, increases gradually with the depth, and approaches rapidly 7 to 9% near the bottom. It is expected that the turbulence intensity approaches a maximum in the transition zone of the boundary layer, the thickness of which is $0.005h_m$ to $0.011h_m$. The variation of turbulence intensity is generally the same for all verticals in the same cross section, except for the verticals very near the banks, where the values of $\sqrt{\overline{v'^2}}/V_0$ are smaller; the latter is due to the low local mean velocity there. Near the entrance of the bend, in the region of highly accelerated flow, the turbulence intensity is low. From Section $3\pi/16$ to Section $7\pi/16$, along verticals between $r/r_c = 0.90$ and 1.00, the turbulence intensity is found to increase linearly from the free surface down towards the bottom instead of having nearly a constant value near the surface.

Measurements of the turbulent shear $\overline{u'v'}$, although not precise enough to give quantitative results, as discussed in Chapter VI, do yield qualitative conclusions. In general, $\overline{u'v'}/V_0^2$ is a maximum near the banks, where its value approaches that of $\overline{v'^2}/V_0^2$. In the region away from the banks the value of $\overline{u'v'}/V_0^2$ approaches zero near the surface, increases slowly from about mid-depth on down, and reaches the same order of magnitude as $\overline{v'^2}/V_0^2$ very close to the bottom within the inner-law region.

Since the mean flow pattern is not a function of the Froude number, it may be expected that the turbulence characteristics are also not functions of $\mathbb{F}$. Experimental results of Runs 2 and 3 for $\mathbb{F} = 0.81$ and 0.58 and $B_b/h_m = 12$, as plotted in Figs. 23, show that the turbulence intensity is approximately independent of the Froude number. Near the bottom, because turbulence is more sensitive to viscous effects than the mean flow, and the thickness of the inner-law region varies for different Reynolds numbers, differences of turbulence characteristics are to be expected near the solid boundary for different values of $\mathbb{R}$.

No attempt has been made to investigate the effect of the width-depth ratio on the turbulence characteristics. Since the mean-flow characteristics do not change appreciably for different values of B_b/h_m, it may be expected that the turbulence characteristics will not change appreciably for flows of large width-depth ratios.

6. Energy Considerations

A bend in an open channel acts as an obstacle similar to bridge piers, sudden contractions, etc., and causes an additional energy loss. As has been discussed in Sec. IV-4, between two control sections Θ_0 and Θ with enclosed fluid volume $\mathbf{V}$, the rate of loss of energy from the mean flow to turbulence is expressed by the volume integral in Eq. (57) containing the turbulent-shear stresses, and the rate of loss directly through viscous action is represented by the volume integral containing the viscous stresses; the sum of these two is the total rate of loss of mean-flow energy from Θ_0 to Θ. Among the seven terms in Eq. (57), these two volume-integral terms are the most significant ones. Unfortunately, $\overline{u'w'}$ and $\overline{v'w'}$ were not measured because of experimental difficulties, so that the integral containing these turbulent shears could not be evaluated. Moreover, the experimental results regarding the two integrals of the viscous terms are not reliable, because the velocity measurements were not made close enough to the bed where the viscous stresses are relatively large. The other four terms in the energy equation were evaluated from the experimental data according to Eq. (57) and plotted in Fig. 25 for Run 3. The integrals, representing the rate at which work is done by pressure and the rate of convection of kinetic energy of the mean motion, are both approximately constant with values of about 0.35 and 0.12, respectively, except near the entrance of the bend where the kinetic energy is slightly higher because of acceleration effects. The rate at which work is done on the mean motion by turbulence stresses is smaller than 1/1000 of the magnitude of the former two and is nearly constant in the upstream three quarters of the straight reach. This rate at which work is done on the mean motion by turbulence stresses decreases sharply in the downstream quarter of the straight reach due to the acceleration effects, and is about 25% smaller at Section $\pi/16$ than that at the midsection of the straight reach; farther downstream, it increases gradually until Section $3\pi/8$ is reached; from there on downstream it is again a constant.

Theoretically, the two energy-loss terms could be evaluated from the requirement of the balance of the energy equation. However, this procedure is not practical for the present study because of the differences in order of magnitude of the terms involved. Both energy-loss terms are two to three orders smaller than either the potential-energy or the kinetic-energy term. With the accuracy of the measurements, the computed result of the energy loss is not reliable.

The loss of energy for a bend is equal to the work which is done to overcome the surface resistance along the solid boundary, the form resistance which associates with the formation of spiral motion and separation if there is any, and the wave resistance owing to the deformation of the free surface. (An accurate subdivision of the total energy loss would be difficult to achieve.) The difference between the total energy loss for a bend and the loss of energy of uniform flow in a corresponding straight channel, i.e., a channel with the same cross-sectional shape, the same roughness, the same discharge, but slightly flatter slope, should give the additional loss due to the bend. The ratio of this additional loss of head to the average velocity head ${V_0}^2/2g$ can then be defined as the loss coefficient of the bend. The variation of the loss coefficient was investigated by Hayat [13] in a specially constructed meandering channel of six 90° bends inserted in the 90-ft tilting flume at the Iowa Institute of Hydraulic Research. Except for the cross section, which was rectangular instead of trapezoidal, and that the meandering channel was with uniform valley slope instead of uniform channel slope, the geometry of the small channel was the same as that of the big model described in Chapter V. Despite the writer's conclusion that the flow pattern was approximately independent of the Froude number, Hayat's experimental results show that the loss coefficient (and hence the wave resistance) increases as $\mathbb{F}$ increases so long as $\mathbb{F}$ is less than 1.5. Hayat also found the loss coefficient to increase with increasing width-depth ratio. Experimental results of Runs 2, 3, and 4 of the present study confirm the tendency of the loss coefficient to increase with Froude number.

VIII. AIR MODEL

The importance of turbulence in the transfer of energy of flow in bends is clearly shown by Eq. (57). Moreover, the knowledge of the spatial variation of the eddy-diffusion coefficient ϵ from turbulence measurements would further the understanding of the flow. In order to obtain such information, because of the difficulties involved in measuring turbulence in water, the possibility of using an air model of similar geometry was studied [40].

A wooden-frame air duct with its upper half section a mirror image of the lower half was constructed for this purpose. Each half of the section was geometrically similar to the midsection of the straight reach in Run 5 of the open-channel model, with a scale ratio of 1 to 4. Thus, $B_b = 1.5$ ft and $r_c = 7$ ft. A bellmouth entrance was constructed 3.33 ft upstream from the entrance of the first bend. Screens were used at the end of the bellmouth for the simulation of the velocity distribution at the entrance of the bends. Air was drawn into the conduit by a squirrel-type fan located 4.75 ft downstream from the exit of the second bend. The surface of the conduit was carefully varnished. The average value of the resistance coefficient f, computed from Eq. (59), at the midsection of the straight reach was found to be 0.0163.

The top of the conduit consisted of removable panels. One special panel had a travelling mechanism on which a rotatable disk was attached, and together they could be moved laterally. The disk was similar to that described in Sec. V-2, with a Lory-type gage fixed to it for vertical movement to the nearest 0.001 ft. Any one of the sensing probes could be mounted on the gage for measurement at any desired location.

The direction of the flow was measured with a yaw meter made from two 0.035-in. hypodermic needles soldered together side by side. The tips of both needles were cut at 45° to the probe axis and the cut surfaces were perpendicular to each other. By rotating the disk to obtain equal pressure readings for each of the two holes of the yaw meter, the direction was determined to the nearest half degree. It was verified that the error due to the velocity gradient along the direction normal to the axis of the yaw meter on the flow direction measurements was negligible.

Total and static pressures were measured with probes made from hypodermic needles pointing in the direction indicated by the yaw meter. The total-pressure probe was 0.035 in. in outside diameter and 0.023 in. in inside diameter. The static-pressure probe was 0.051 in. in outside diameter and had a half ellipsoid nose with four 0.010-in. holes, 90° apart, at 15 probe diameters from the tip. A water manometer open to the atmosphere with readings to the nearest 0.001 ft was employed for pressure measurements.

The Reynolds number for the experiment was 0.85×10^{5}. Details of experimental equipment and procedure can be found in Ref. [40]. Measurements were made along nine verticals in each of the cross sections at every 15° in the second bend, and at the entrance, the midsection, and the exit of the preceding straight reach. The data were then converted by interpolation to the verticals where the open-channel measurements were performed, and plotted in the appropriate figures for comparison with Run 5, for which the width-depth ratio was the same.

The agreement of intensities of the spiral motion, shown in Fig. 21, is fair, except at the exits of both the first and the second bends. There the outward flow is about forty percent larger for the air model. Consequently, the net lateral discharges through the axial section of the channel, shown in Fig. 22, agree very well except in the straight reach and near the exit of the second bend.

From Fig. 16 it is seen that the relative longitudinal velocity components $\bar{v}/V_0$ for air and open-channel models agree qualitatively;

quantitatively, however, they deviate as much as $\pm 10\%$. The same is true for the relative radial velocity component $\bar{u}/V_0$ (Figs. 17), except for the upstream one third of the bend where the deviation is even more. The air-model experiment also indicates that, as in the open-channel case, the vertical velocity component $\bar{w}$ is negligible compared to $\bar{v}$ and the static pressure is constant along any vertical.

The piezometric heads measured in the air model are compared to the respective transverse water-surface profiles in Figs. 10. The agreement is fairly good. The variation of the piezometric head in the air model was computed through

$$\frac{h - h_m}{V_0^2/2g} = \frac{h_l - (h_{S2} + sl)}{V_0^2/2g}$$

where h_l is the piezometric head on the vertical in a section at distance l from the midsection S2 of the straight reach of the air model, h_{S2} is the average piezometric head at section S2, and s is the hydraulic gradient of the line of best fit through points of average piezometric head at each section.

There are several possible reasons for the disagreement between the experimental results of the air model and those of Run 5. First, there is a slight difference in Reynolds number between the two. The value of $\mathbb{R}$ for the air model was 0.85×10^5 and that for Run 5 was 1.08×10^5. However, for such relatively high Reynolds numbers the viscous effects can be regarded as the same for both cases despite this difference. Secondly, there is a slight difference in geometry due to the superelevation of the free surface. But the maximum superelevation for Run 5 was only 2.9% of the average depth, and the variation of the average depth for cross sections was negligible; hence, this difference probably contributes only a small part of the disagreement. Thirdly, the local depth of the flow was self-adjusted to fulfill the energy requirement in the open-channel model, and consequently, the amount of lateral flow required by continuity was reduced as compared to the air model, in which the depth was a constant. Fourthly, the free surface was a natural boundary for turbulence in the open-channel case, while in the air model no such boundary existed at the plane of symmetry. Fifthly, the entrance conditions, especially the turbulence level, at the first bends of the two models were different; however, the effect of this difference was checked experimentally at the exits of the first bends and was found to be negligible. Lastly, the relative roughness might have been different in the two models. Although it was not possible to determine the surface resistance accurately, as has been discussed in Chapter VI, the average values of f of 0.016 and 0.014 at the midsections of the straight reaches for the air model and for Run 5, respectively, determined by velocity measurements, can be used as a roughness indication. But the velocity measurements were not made close enough to the bed, so the accuracy of f obtained is questionable. Moreover, it can be seen from Eq. (33) that $\bar{u}/V_0$ is only slightly affected by the change of the boundary roughness.

Thus, despite the fact that similarity exists between the flow in an open-channel meander and that in an air model of similar geometry, the experimental results do not lead to a quantitative conclusion. Further experimental studies on this question with similar boundary roughness and Reynolds numbers are desirable.

IX. CONCLUSIONS

Through a series of experiments, the characteristics of subcritical flow in a meandering channel of large width-depth and radius-depth ratios, at Reynolds numbers of the order of 10^5 or higher, have been determined and compared with an approximate theoretical solution for fully developed bend flow. It has been confirmed that the spiral motion and the superelevation are two of the most evident characteristics of the flow, and that the effect of the bend extends both upstream and downstream. For a meandering channel with finite central angle, the highest velocity occurs very near the inner bank around the entrance of the curve and gradually shifts outward with distance downstream. The magnitude of the radial velocity component is one order smaller than that of the longitudinal component, and the vertical velocity component is negligible except very near the banks. Because the flow pattern changes from section to section, in general there is a lateral discharge through any longitudinal section, although its magnitude is very small compared to the longitudinal discharge. The nondimensional flow pattern is a function of the width-depth ratio but not of the Froude number, provided that the relative superelevation is small and $\mathbb{F}$ is appreciably less than unity. Moreover, the pressure distribution along a vertical is very nearly hydrostatic.

For flow in bends connected by short tangents, like those of the present model, there exist two spirals through most of each bend — a decaying spiral from the preceding bend near the outer bank, and a growing spiral of reversed rotation near the inner bank. The boundary-shear stress is generally higher near the inner bank, and its distribution is similar to that of the longitudinal component of the mean velocity averaged over verticals. However, due to the direction of the spiral motion, the location most seriously exposed to scour is not along the inner bank but at the outer bank near the exit of the bend.

Although fully developed bend flow was not obtained for the channel geometry investigated, the theoretical solution for this type of flow was found to provide a useful approximation to such mean-flow characteristics as the velocity and boundary-shear distributions and the transverse water-surface profiles; it also substantiates the experimental indications that the spiral motion becomes stronger as the radius-depth ratio decreases and that the flow in the central region becomes independent of the width-depth ratio for values of this ratio greater than roughly 12.

The measured turbulence intensity of the flow ranges from 3 to 9 percent. In general, it is lower and almost constant near the surface and higher near the solid boundary. Since it is through the turbulence stresses that part of the energy of the mean flow is converted into turbulence energy and eventually dissipated into heat, further and more detailed information on the turbulence in a meandering channel is important and desirable. Concerning the possibility of using an air model of similar geometry to facilitate the measurement of mean-flow and, especially, turbulence characteristics, the experimental results did not lead to a conclusion, because only a limited investigation of this sort was conducted. They do indicate, however, that the loss of energy of flow in an open-channel meander is greater than that of its air-duct simulation, and increases with the Froude number because of wave resistance.

NOTATION

A	cross-sectional area
B	channel width
B_b	bottom width
B_s	surface width
C	Chézy coefficient
c	a constant
F	a function
$\mathbb{F}$	Froude number, $V_0/\sqrt{gh_0}$
f	resistance coefficient
g	acceleration of gravity
h	depth of flow
h_i	water-surface elevation above channel bottom at innermost point
h_m	average depth of flow at midsection of straight reach
h_o	water-surface elevation above channel bottom at outermost point
h_0	hydraulic mean depth of flow, A/B_s
K	loss of energy per unit change of angle of bend, $= \partial[(\bar{p}/\rho) + \Omega]/\partial\theta$
L	wave length of meander as defined in Fig. 1
m	boundary-roughness coefficient, defined as $v_{av}/\bar{v}_\tau$
n	Manning roughness coefficient
p	pressure intensity
Q	total discharge
q_r	radial discharge per unit width, positive outward
R	hydraulic radius
$\mathbb{R}$	Reynolds number, VR/ν
r	radial coordinate
r_c	centerline radius of bend
r_i	innermost radius of bed
r_o	outermost radius of bed
S	surface area
s	water-surface slope in longitudinal direction

s_b	bed slope
s_c	water-surface slope along centerline of channel
s_r	water-surface slope in radial direction
s_v	valley slope
T	length of tangent
T_1	distance between tangents of bends as defined in Fig. 2
u	radial velocity component
V	total velocity
V_0	average velocity over midsection of straight tangent, Q/A
$\mathbf{V}$	volume
v	longitudinal velocity component
v_{av}	average longitudinal component of mean velocity over a vertical
$(v_{av})_c$	average longitudinal component of mean velocity over centerline vertical
v_τ	shear velocity, $\sqrt{\tau_0/\rho}$
W	amplitude of meander as defined in Fig. 1
w	vertical velocity component
x	transverse coordinate in tangent section
y	longitudinal coordinate in tangent section, positive downstream
z	vertical coordinate
α	meander angle at nodal point, as defined in Fig. 1
δ	thickness of viscous sublayer
ϵ	eddy diffusion coefficient
ϵ_{ij}	eddy diffusion coefficient in i-j plane
θ	angular coordinate
θ_c	central angle of bend
κ	Kármán universal constant
μ	dynamic viscosity
ν	kinematic viscosity
ρ	mass density
σ_i	normal stress in i-direction
τ_{ij}	shear stress on plane perpendicular to i-direction along j-direction

REFERENCES

1. Blue, F. L., Jr., Herbert, J. K., and Lancefield, R. L., "Flow Around a River Bend Investigated," Civil Engineering, Vol. 4, May, 1934.

2. Böss, P., "Anwendung der Potentialtheorie auf die Bewegung des Wassers in gekrümmten Kanal-oder Fluszstrecken," Der Bauingenieur, Vol. 15, June, 1934.

3. Chow, V. T., Open Channel Hydraulics, McGraw-Hill, New York, 1959.

4. Denzler, C. E., "Optimum Shape of a 90° Bend in a Rectangular Channel," M.S. Thesis, University of Iowa, February, 1960.

5. Eakin, H. M., "Diversity of Current-direction and Load-distriubtion on Stream-bends," Transactions, American Geophysical Union, pt. II, 1935.

6. Eichenberger, H. P., "Shear Flow in Bends," Office of Naval Research Technical Report, No. 2, 1952.

7. Einstein, H. A., and Harder, J. A., "Velocity Distribution and the Boundary Layer at Channel Bends," Transactions, American Geophysical Union, Vol. 35, No. 1, 1954.

8. Eskinazi, S., and Yeh, H., "An Investigation on Fully Developed Turbulent Flows in a Curved Channel," Jour. of Aero. Sciences, Vol. 23, No. 1, 1956.

9. Fargue, L., La Forme du Lit des Rivieres a Fond Mobile, Gauthier-Villars, Paris, 1908.

10. Fedorov, N. N., "Experimental Investigations of Meander Processes," Trudy GGI, USSR, No. 44, 1954.

11. Friedkin, J. F., A Laboratory Study of the Meandering of Alluvial Rivers, Waterways Experiment Station, Corps of Engineers, U.S. Army, Vicksburg, Miss., 1945.

12. Hawthorne, W. R., "Secondary Circulation in Fluid Flow," Proceedings, Royal Soc. of London, Vol. 206A, 1951.

13. Hayat, S., "The Variation of Loss Coefficient with Froude Number in an Open-Channel Bend," M.S. Thesis, University of Iowa, January, 1965.

14. Hinze, J. O., Turbulence, McGraw-Hill, New York, 1959.

15. Hsu, E. Y., "The Measurement of Local Turbulent Skin Friction by Means of Surface Pitot Tubes," Report 957, David Taylor Model Basin, 1955.

16. Hubbard, P. G., Operating Manual of the IIHR Hot-Wire and Hot-Film Anemometers, Bull. 37, University of Iowa Studies in Engineering, 1957.

17. Ippen, A. T., and Drinker, P. A., "Boundary Shear Stresses in Curved Trapezoidal Channels," Proceedings, ASCE, Vol. 88, No. HY5, September, 1962.

18. Ippen, A. T., Drinker, P. A., Jobin, W. R., and Shemdin, O. H., "Stream Dynamics and Boundary Shear Distributions for Curved Trapezoidal Channels," Report 47, Hydrodynamic Lab., MIT, 1962.

19. Kondratév, N. E., Ed., River Flow and River Channel Formation, partly translated by Prushansky, Y., Israel Program for Scientific Translations, 1962.

20. Landweber, L., "Reanalysis of Boundary Layer Data on a Flat Plate," 9th Internatl. Towing Tank Conference, Paris, 1960.

21. Leliavsky, N., "Des Courants Fluviaux et de la Formation du Lit Fluvial," 6th Internatl. Cong. Intérieure Navagation, The Hague, 6e question, No. 4, 1894.

22. Liatkher, V. M., and Prudovskii, A. M., "Conditions of Fluid Motion in a Bend as a Function of the Resistance Coefficient and the Corresponding Width of Flow," Hydraulics of Constructions and Dynamics of River Flows, Academy of Science, USSR, Moscow, 1959.

23. Leopold, L. B., Bagnold, R. A., Wolman, M. G., and Brush, L. M., Jr., "Flow Resistance in Sinuous Channels," U.S. Geol. Survey Professional Paper 282-D, 1960.

24. Leopold, L. B., and Wolman, M. G., "River Meanders," Bull. Geol. Soc. Am., Vol. 71, 1960.

25. Mississippi River, Flood Control and Navigation Maps, Cairo, Ill. to the Gulf of Mexico, 28th ed., Corps of Engineers, U.S. Army, Vicksburg, Miss., 1960.

26. Missouri River, Navigation Charts, Sioux City, Iowa to Mouth, Corps of Engineers, U.S. Army, Omaha, Neb., 1960.

27. Mockmore, C. A., "Flow Around Bends in Stable Channels," Transactions, ASCE, Vol. 109, 1944.

28. Nippert, H., "Neuere Versuche über den Strömungsvorgang in gebrümmten Kanalen," Der Bauingenieur, Vol. II, January, 1930.

29. Preston, J. H., "The Determination of Turbulent Skin Friction by Means of Pitot Tubes," Jour. Royal Aero. Soc., Vol. 54, 1954.

30. Prus-Chacinski, T. M., "Patterns of Motion in Open-Channel Bends," Assoc. Internatl. d'Hydrologie, Pub. 38, Vol. 3, 1954.

31. Raju, S. P., "Resistance to Flow in Curved Open Channels," in Abridged Translations of Hydraulic papers, Proceedings, ASCE, 1937.

32. Richter, H., "Der Druckabfall in gekrümmten glatten Rohrleitungen," Forschungsarbeiten auf dem Gebiet des Ingenieurwesens, No. 338, 1930.

33. Rouse, H., Ed., Engineering Hydraulics, John Wiley & Sons, New York, 1950.

34. Rouse, H., Ed., Advanced Mechanics of Fluids, John Wiley & Sons, New York, 1959.

35. Rozovskii, I. L., Flow of Water in Bends of Open Channels, Academy of Sciences of Ukranian SSR., Kiev, 1957, Translated by Prushansky, Y., The Israel Program for Scientific Translations, 1961.

36. Shanmugam, A., "Optimum Shape of a 90^{o} Bend in a Trapezoidal Channel," M. S. Thesis, State University of Iowa, August, 1963.

37. Shukry, A., "Flow Around Bends in an Open Flume," Transactions, ASCE, Vol. 115, 1950.

38. Smith, D. W., and Walker, J. H., "Skin-Friction Measurements in Incompressible Flow," NACA Tech. Note 4231, March, 1958.

39. Thomson, J., "On the Origin and Winding of Rivers in Alluvial Plains, with Remarks on Flow Around Bends in Pipes," Proceedings, Royal Soc. of London, Vol. 25, 1876.

40. Tieleman, H. W., "Air Tunnel Study of a Meander Model," M. S. Thesis, University of Iowa, February, 1964.

41. Wattendorf, F. L., "A Study of the Effect of Curvature on Fully Developed Turbulent Flow," Proceedings, Royal Soc. of London, Vol. 148, June, 1935.

42. Yarnell, D. L., and Woodward, S. M., "Flow of Water Around 180° Bends," Tech. Bull. No. 526, U.S. Dept. of Agriculture, 1936.

43. Yeh, H., Rose, W. G., and Lien, H., "Further Investigations on Fully Developed Turbulent Flows in a Curved Channel," Report, Dept. of Mechanical Engineering, the Johns Hopkins University, September, 1956.

44. Yen, C. H., and Howe, J. W., "Effects of Channel Shape on Losses in a Canal Bend," Civil Engineering, January, 1942.

TABLE AND FIGURES

(See Page 2 for Fig. 1)

TABLE I Important Experimental Work on Flow in Open-Channel Bends

Investigator	No. of Bends	θ_c Deg.	Cross-Sectional Shape	r_c in.	B in.	h in.	V_0 fps	r_c/B	r_c/h	B/h	B/R	Bed Slope	$F=\frac{V_0}{\sqrt{gh_0}}$	$R=\frac{V_0 R}{\nu}$ in 10^5	Items Investigated	Remarks	Ref.
Raju	1	90	Rectangular	59 11.8	11.8 11.8	<7.9 2.76- 7.3	1.15- 2.30	1-3		1.6- 4.3		0	<1	0.15- 0.45	V_0, loss coefficient		31
Böss	1		Rectangular	25.5 25.5	11.8 11.8	3.54 4.3	1.96 1.63	2.16 2.16	6.1 5.9	3.33 2.72	5.35 4.57		0.64 0.48	0.36 0.34	Superelevation		2
Yarnell and Woodward	1	180	Rectangular	7.5- 12.5	5-10	7.5	2.6- 2.9	1.0- 2.5	1.07- 1.67	0.67- 1.33	2.66- 3.33	0	0.6- 0.7	0.42- 0.68	Longitudinal velocity distribution, water surface, different entrance velocity distributions		42
Mockmore	2	180	Rectangular	21 21	18 18	5.6 ~4.5	~0.57 ~0.5	1.17	3.75 4.6	3.2 4.0	5.2 6.0	0.00005 0.00005	0.15 0.14	0.17 0.13	Longitudinal velocity distribution, water surface	$\frac{T}{r_c} = 2.3$	27
Shukry	1	45- 180	Rectangular	5.9- 35.5	11.8	7.1- 14.2	0.36- 3.2	0.5- 3.0	0.42- 5.0	0.83 1.67	2.83- 3.67	0	0.1- 0.8	0.10- 0.78	Velocity components, water surface		37
Prus-Chacinski	5	45	Rectangular	39	6	2.5		6.5	16	2.4	4.4			0.055	Spiral motion, effects of entrance condition	$\frac{T}{r_c} = 0.46$	30
Einstein and Harder		120	Rectangular	120	16	1.3- 3.3	0.4- 0.8	7.5	37- 91	4.9- 12.2	7.0- 14.2	~0.0003	~0.2- 0.4	~0.05- 0.13	$\bar{V}$ to verify that $\frac{r}{\bar{V}}\frac{d\bar{V}}{dr}$ could be >1	Spiral transition approach	7
Leopold, Bagnold, Wolman and Brush	Sinusoidal		Trapezoidal 1:1 side slope		4.5 (bottom)	0.18- 1.6	0.37- 1.53			2.9 4.3	4.3- 5.8	0.00035 -0.0118 (surface)	0.2- 0.9	0.14- 0.24	resistance		24
Ippen, Drinker, Jobin, and Shemdin	1	60	Trapezoidal 2:1 side slope	60	24 (bottom)	2.98- 6	1.33- 1.91	2.5	10- 20	4-8	5.6- 10.0	0.00064	0.38- 0.55	0.30- 0.75	Longitudinal velocity distribution, water surface, boundary shear	Smooth n=0.010	17,18
	1	60		60	24 (bottom)	3.94 6.04	0.94 1.18	2.5	9.9 15.2	4-6	5.9- 8.0	0.00064	0.32 0.34	0.24 0.36		Rough n=0.017	
	1	60		70	12 (bottom)	2.01- 3.98	0.87- 1.40	5.8	19.3- 34.7	3-6	4.5- 7.9	0.00055	0.42- 0.51	0.11- 0.31		Smooth n=0.010	
	1	60		60	24 (bottom)	3.86 6.00	1.50 1.91	2.5	10 15.5	4.0 6.2	5.6 8.1	0.00064	0.52 0.55	0.408 0.75		Simulated entrance condition n=0.010	

TABLE I (Continued)

Investigator	No. of Bends	θ_c Deg.	Cross-Sectional Shape	r_c in.	B in.	h in.	V_0 fps	r_c/B	r_c/h	B/h	B/R	Bed Slope	$F=\frac{V_0}{\sqrt{gh_0}}$	$R=\frac{V_0 R}{\nu}$ in 10^5	Items Investigated	Remarks	Ref.
Milovich	1	180	Rectangular	11.0	9.5	1.8-5.4	0.02-0.16	1.16	2.0-6.2	1.7-5.3	3.7-5.5	0	< 1	0.0016-0.012	Trace of bottom particles, surface velocity		19,35
Daneliya	1	180	Rectangular	23.6	15.8	4.7	~1	1.5	5.0	3.33	5.33	0	0.28	0.21	Distribution of longitudinal and radial velocity components		19,35
Kozhevnikov	1	180	Rectangular Triangular Trapezoidal	63-73	12.1-31.5	0.8-3.9	0.65-1.9	2-6	16-90	6.7-40		0.0004-0.00125	<1	0.031-0.45	Traces and velocity of bottom and surface particles, water surface		19,35
	3	180	Rectangular	31.4	15.7	0.79-2.4	0.46-1.2	2	13.3-40	6.7-20	8.7-22	0.0005-0.0015	0.2-0.7	0.023-0.15			
Ter-Asvatsatryan	1	67.5 180	Rectangular	8.2 22.8	15.1	4.3 5.9	1-1.3	5.5 1.5	19 3.85	3.5 2.5	5.5 4.5		0.3-0.4	0.18-0.25 0.22-0.32	Distribution of velocity components		19,35
Konovalov, Makkaveev, V.M., and Romanenko	Sinusoidal		Trapezoidal		15	2-3.9	0.65-0.82			3.8-8.3	5.8-9.6	0.0005-0.0015	0.2-0.3	0.07-0.14	Direction of bottom and surface velocities		19
Makkaveev, N.I., and Romanenko	Sinusoidal		Rectangular	min. 19.7	9.8	1.2-4.7	0.65-2.4	min. 2	min. 4.17	2-10	4.1-10.4		< 1	0.04-0.4	Direction of bottom and surface velocities		19,35
Fidman	3	117.5	Rectangular	88.5	39.4	4.5-6.3	0.29-1.2	2.25	14-19.5	6.25-8.33	8.2-11.8		0.07-0.3	0.09-0.38	Water surface		19,35
Ananyan	2	180	Rectangular	98.5	19.7	5.9-7.1	0.92-1.1	5.0	14-17	2.8-3.3	4.8-5.3		0.21-0.28	0.24-0.31	Distribution of velocity components		19,35
Rozovskii	1	29	Rectangular Triangular Polygonal	23-39	14.2-31.5	0.8-5.9 Triang. up to 24	0.49-0.85	1-2.5	2.7-4.3								35
	1	90	Movable bed														
	1	180	Rectangular Triangular	23-39	14.2-31.5	0.8-5.9	0.49-0.95	1-2.5	5.3-45	4.3-27	6.4-29		0.2-0.5	0.0028-0.27	Distribution of velocity components and water surface		

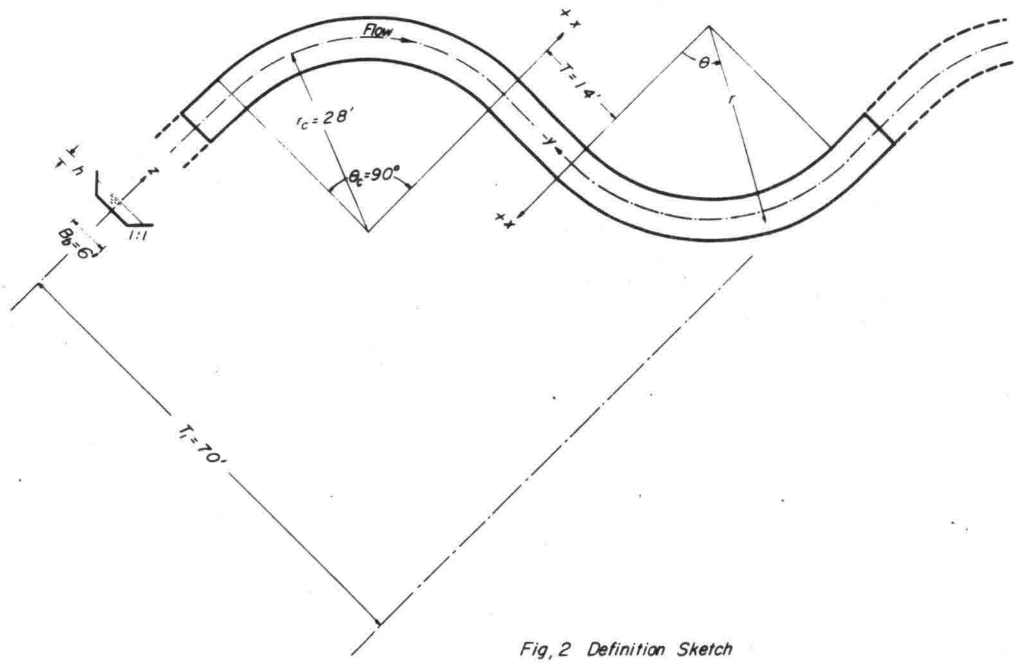

Fig, 2 Definition Sketch

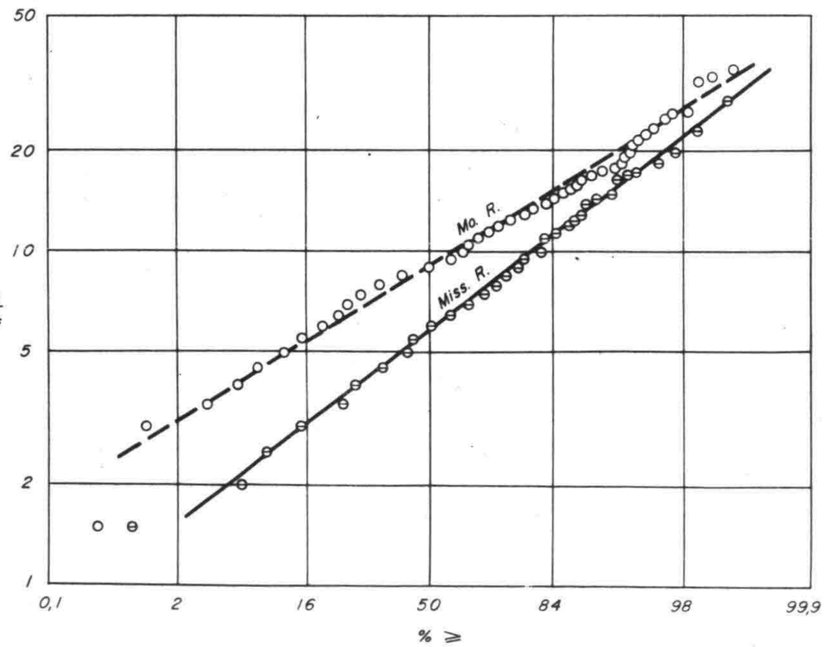

Fig, 3 Cumulative Frequency Curves of r_c/B_s

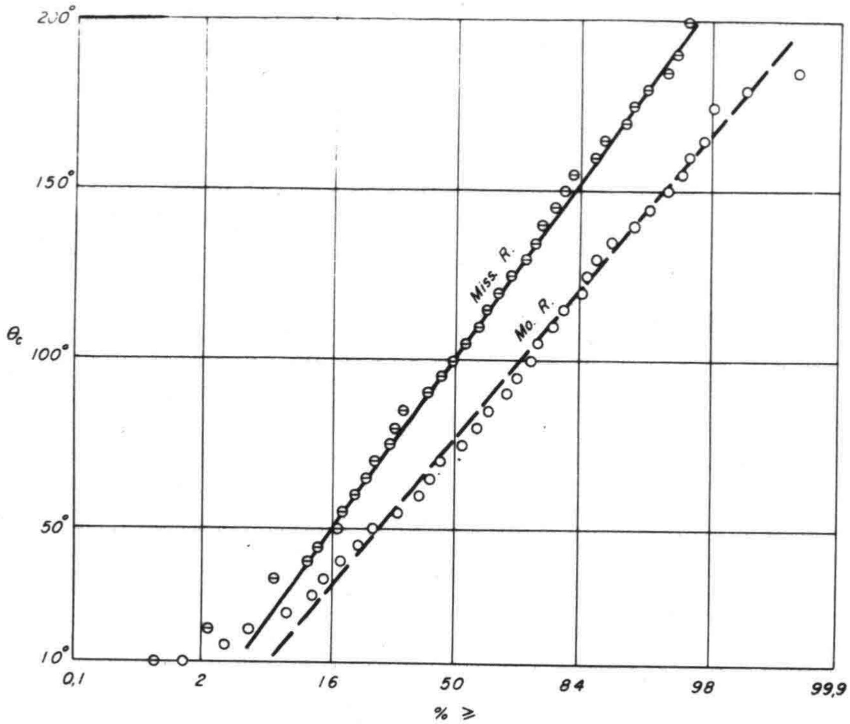

Fig, 4 Cumulative Frequency Curves of θ_c

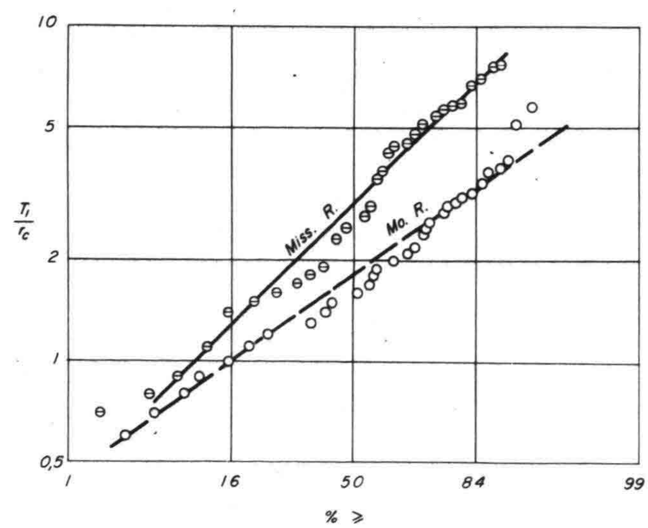

Fig, 5 Cumulative Frequency Curves of T_1 / r_c

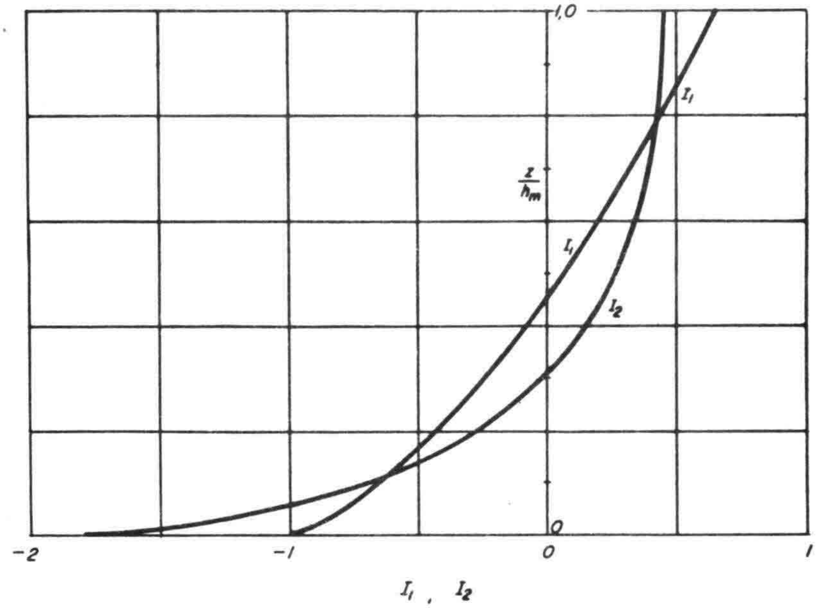

Fig, 6 Values of I_1 and I_2

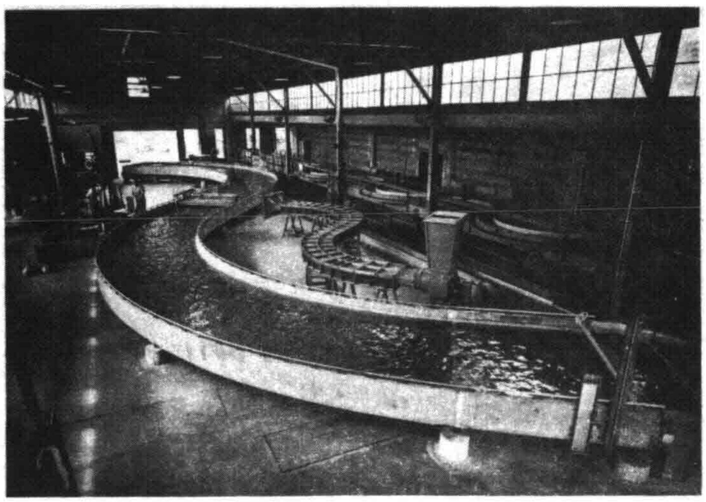

Fig, 7 Photograph of Meander Models

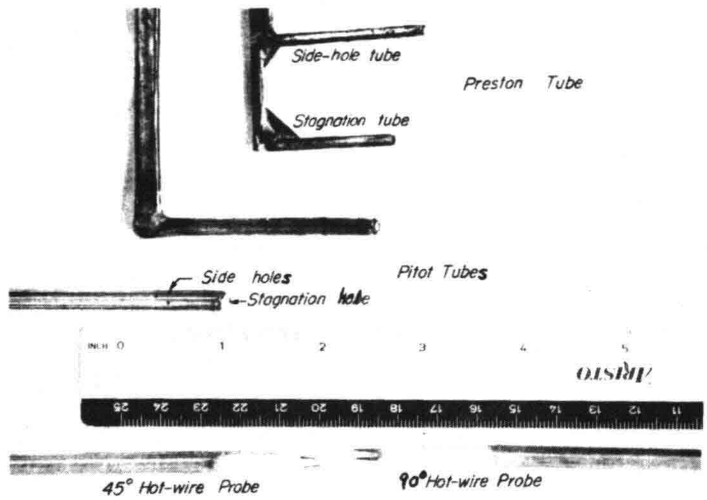

Fig, 8 Photograph of Sensing Probes

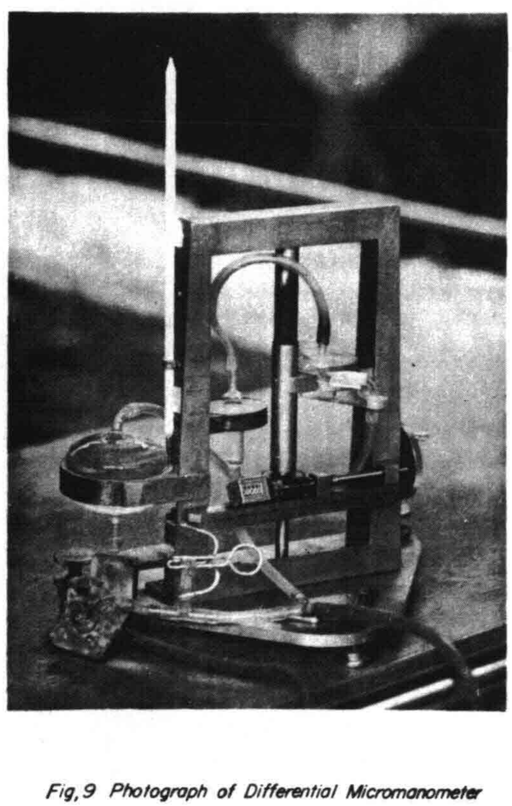

Fig, 9 Photograph of Differential Micromanometer

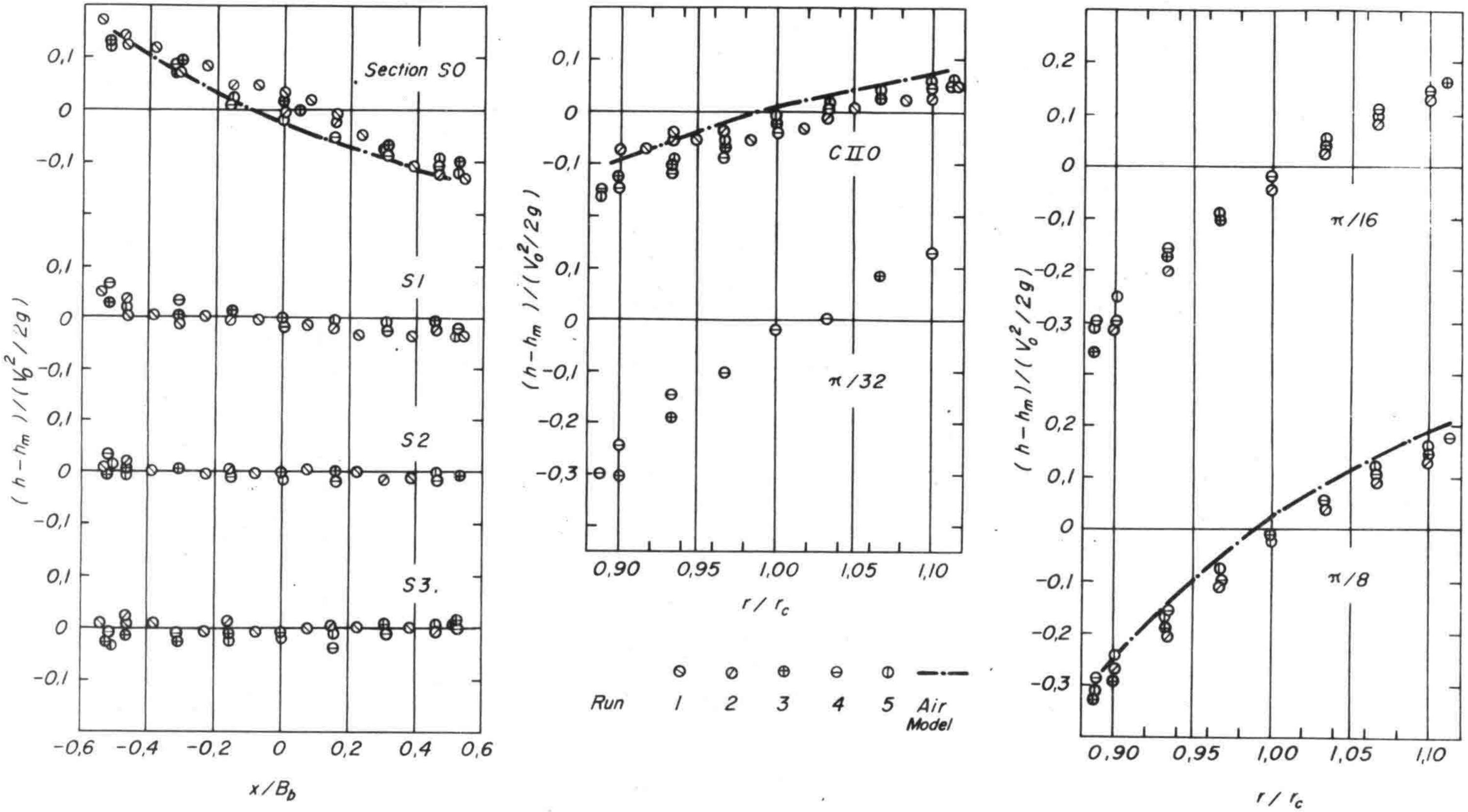

Fig. 10 Transverse Water-surface Profiles

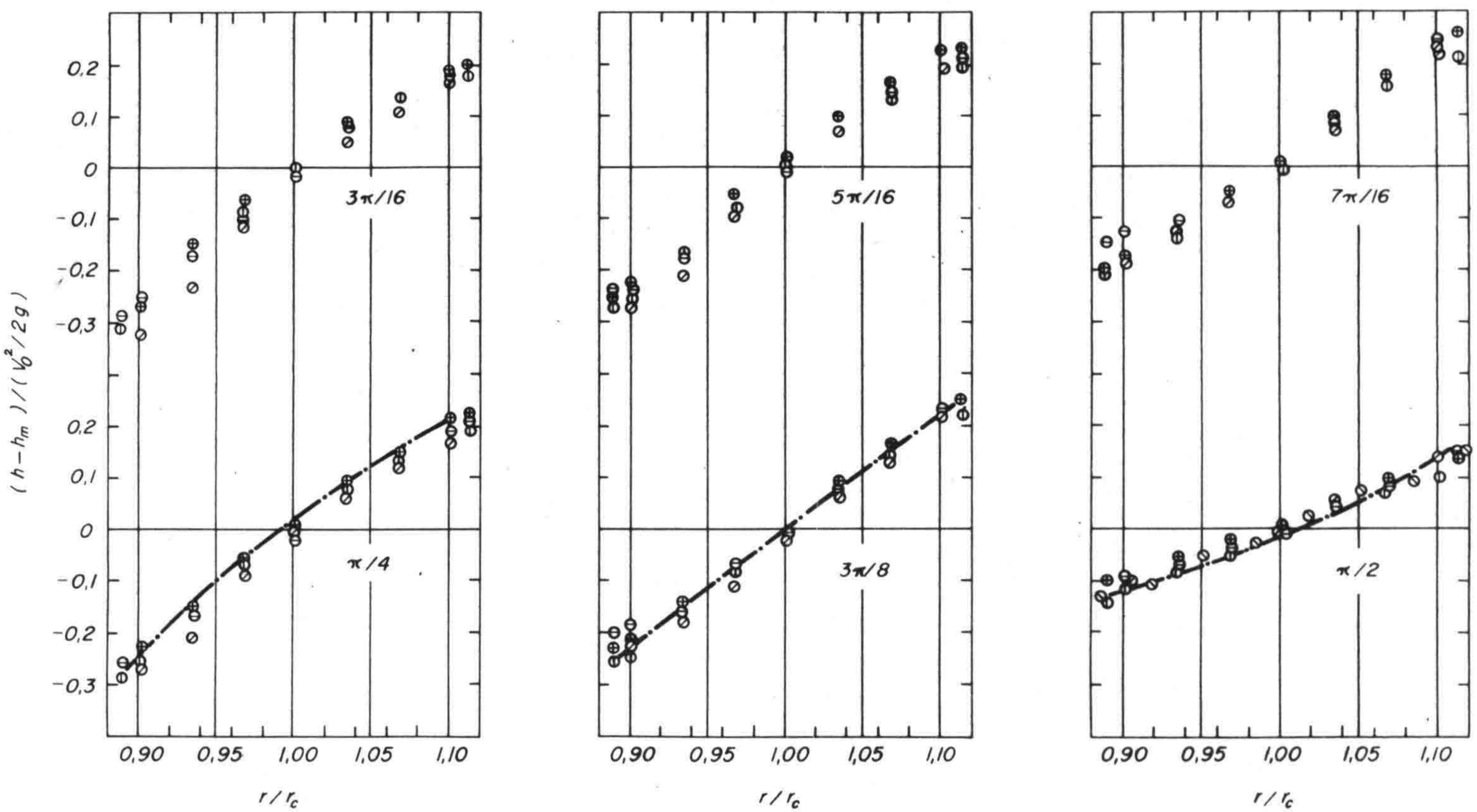

Fig, 10 (continued)

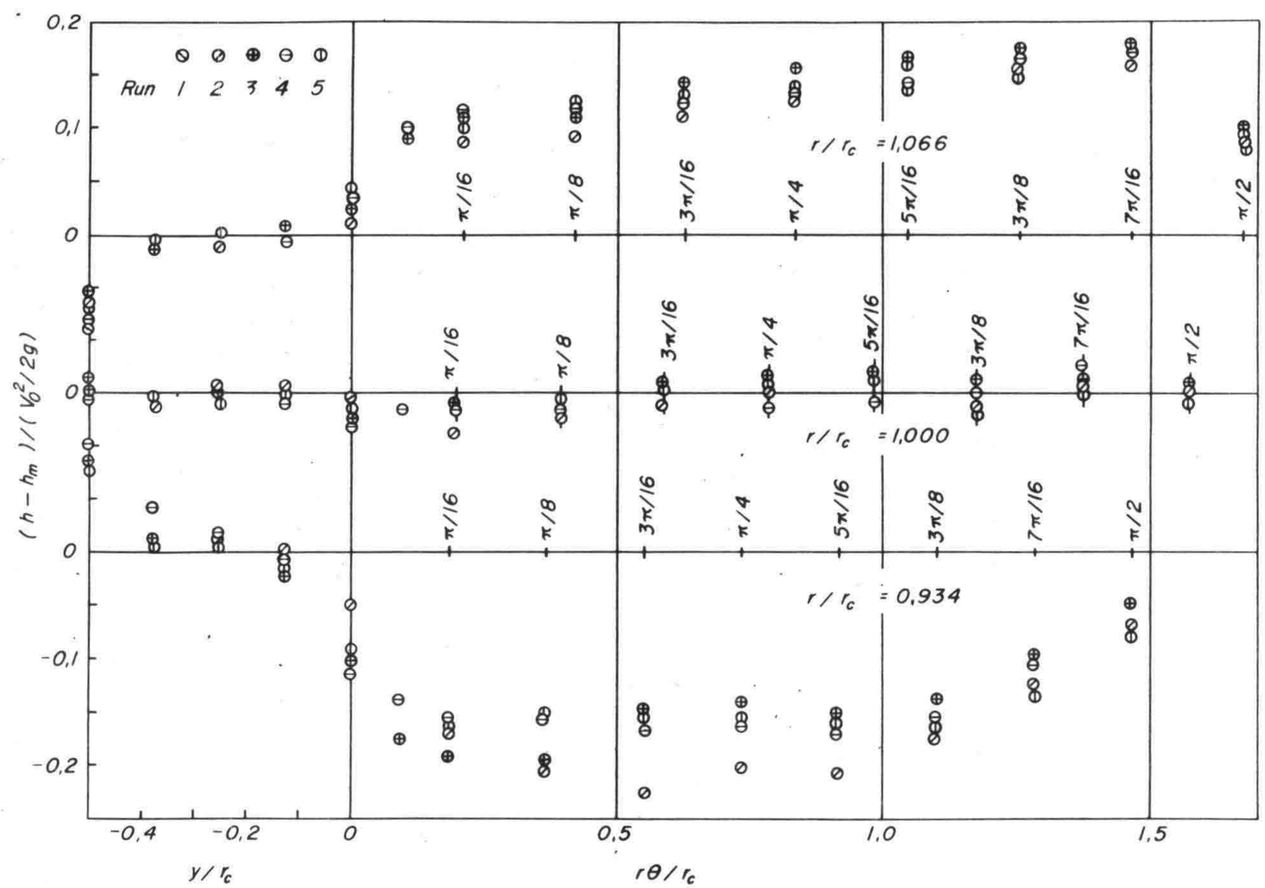

Fig, 11 Longitudinal Water-surface Profiles

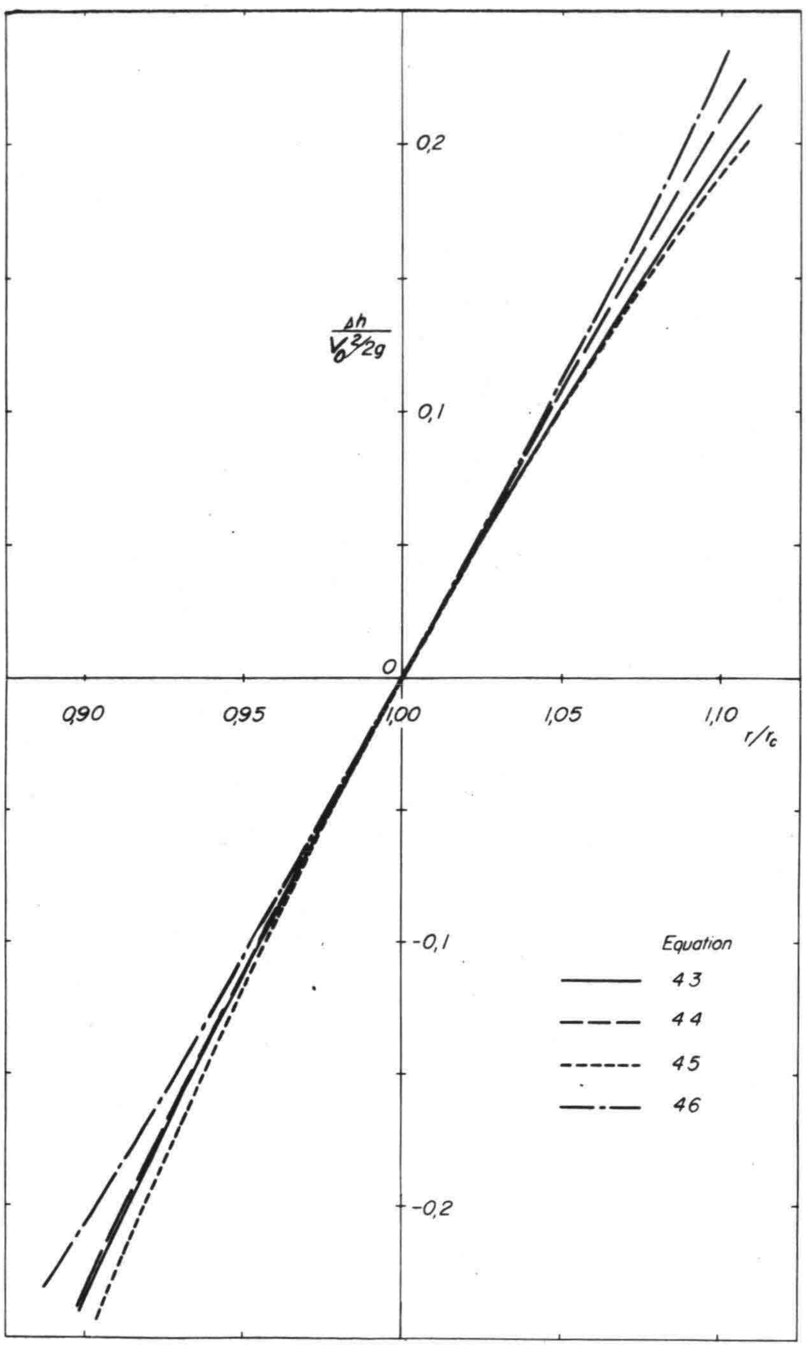

Fig. 12 Theoretical Transverse Water-surface Profiles for $(v_{av})_c/V_0 = 1.05$

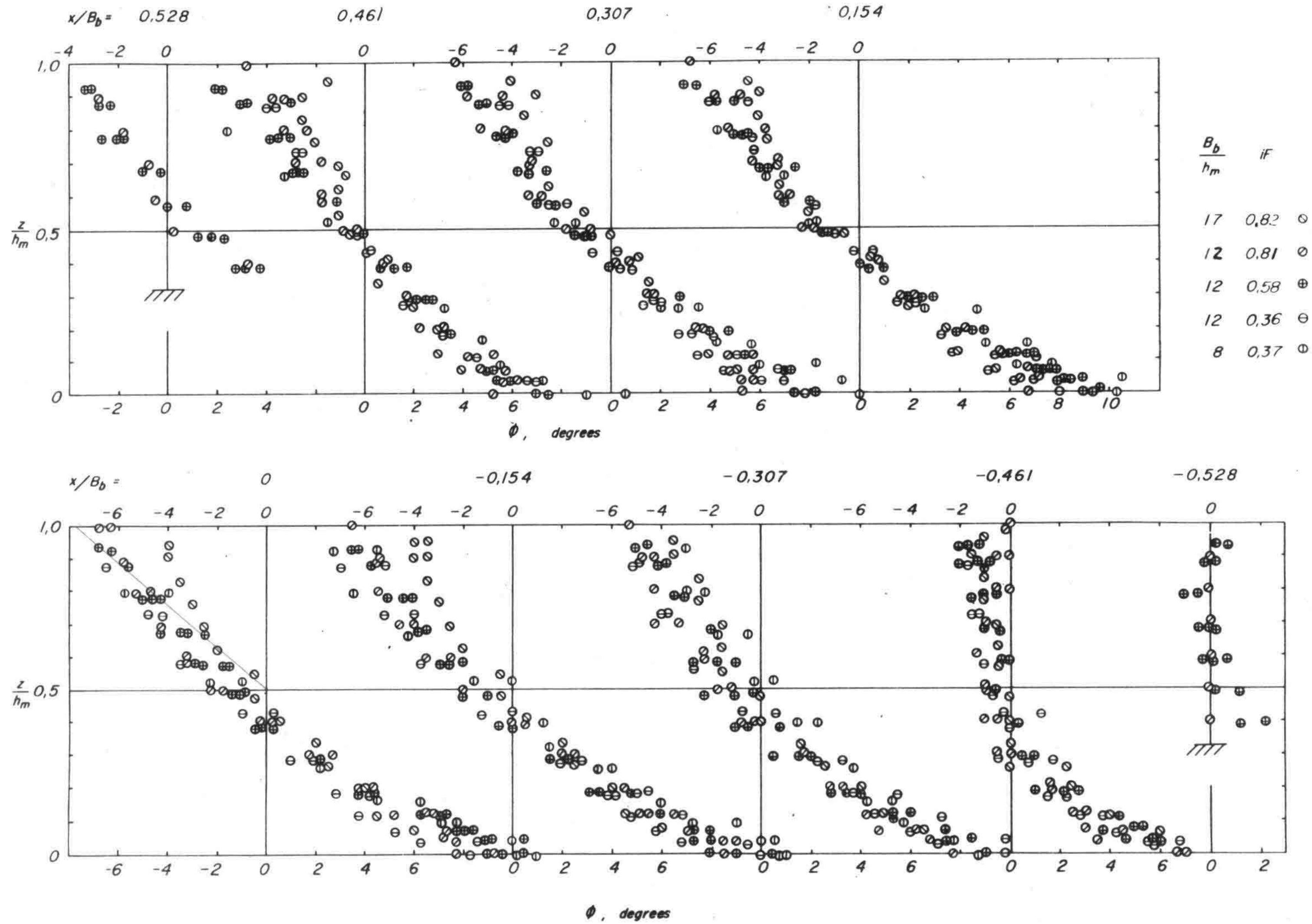

Fig. 13 Angles of Flow Direction in Horizontal Planes, (a) Section SO

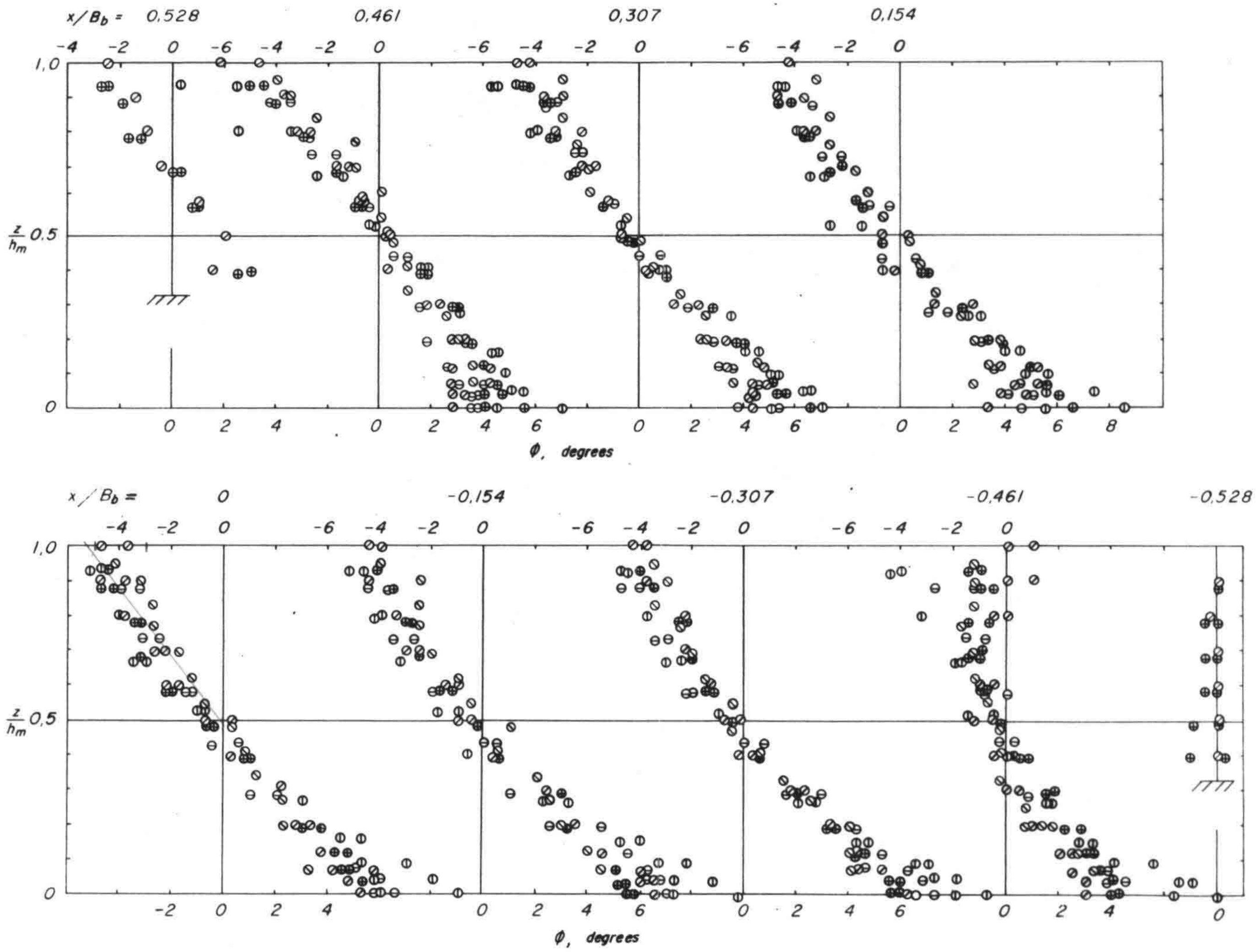

Fig. 13 (b) Section SI

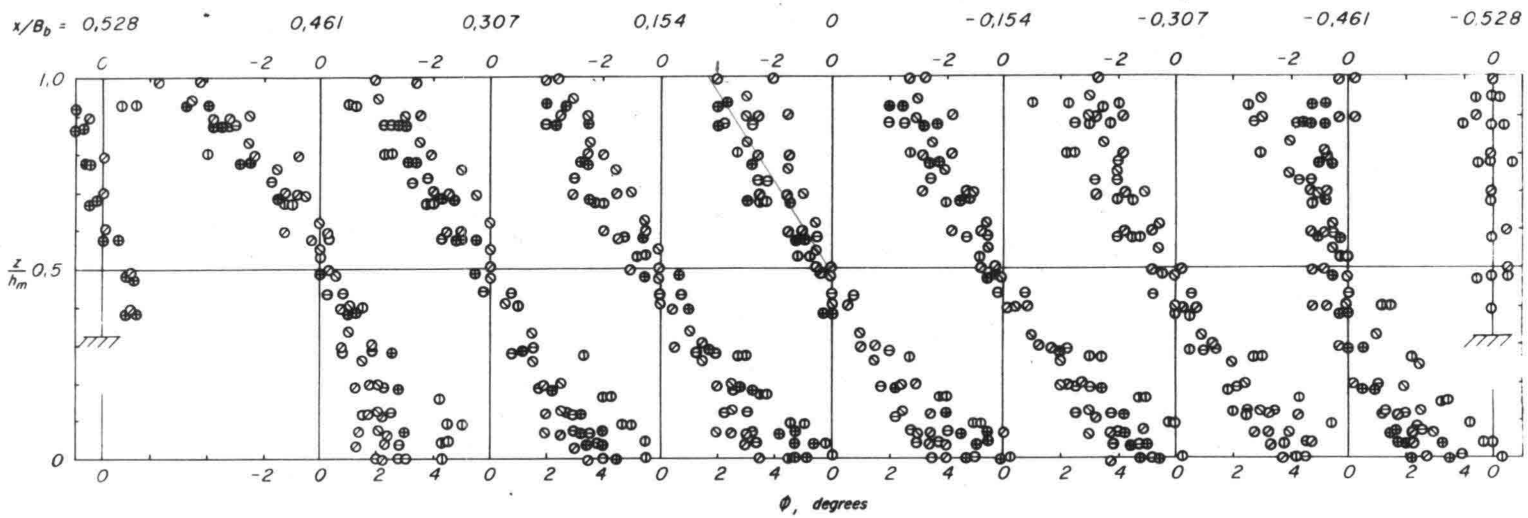

Fig, 13 (c) Section S2

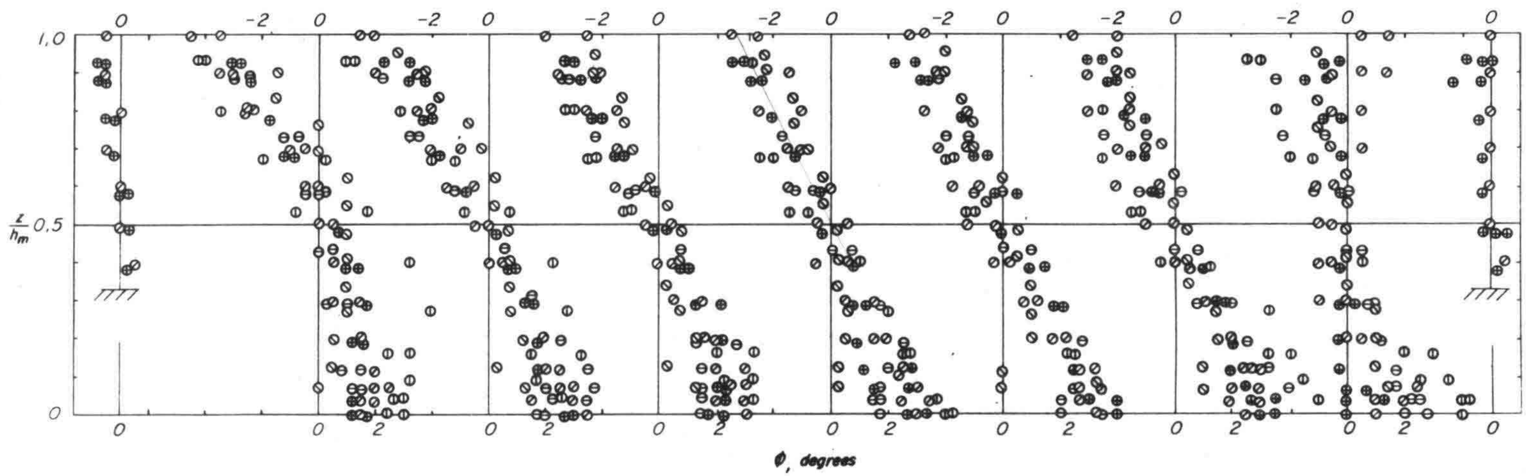

Fig, 13 (d) Section S3

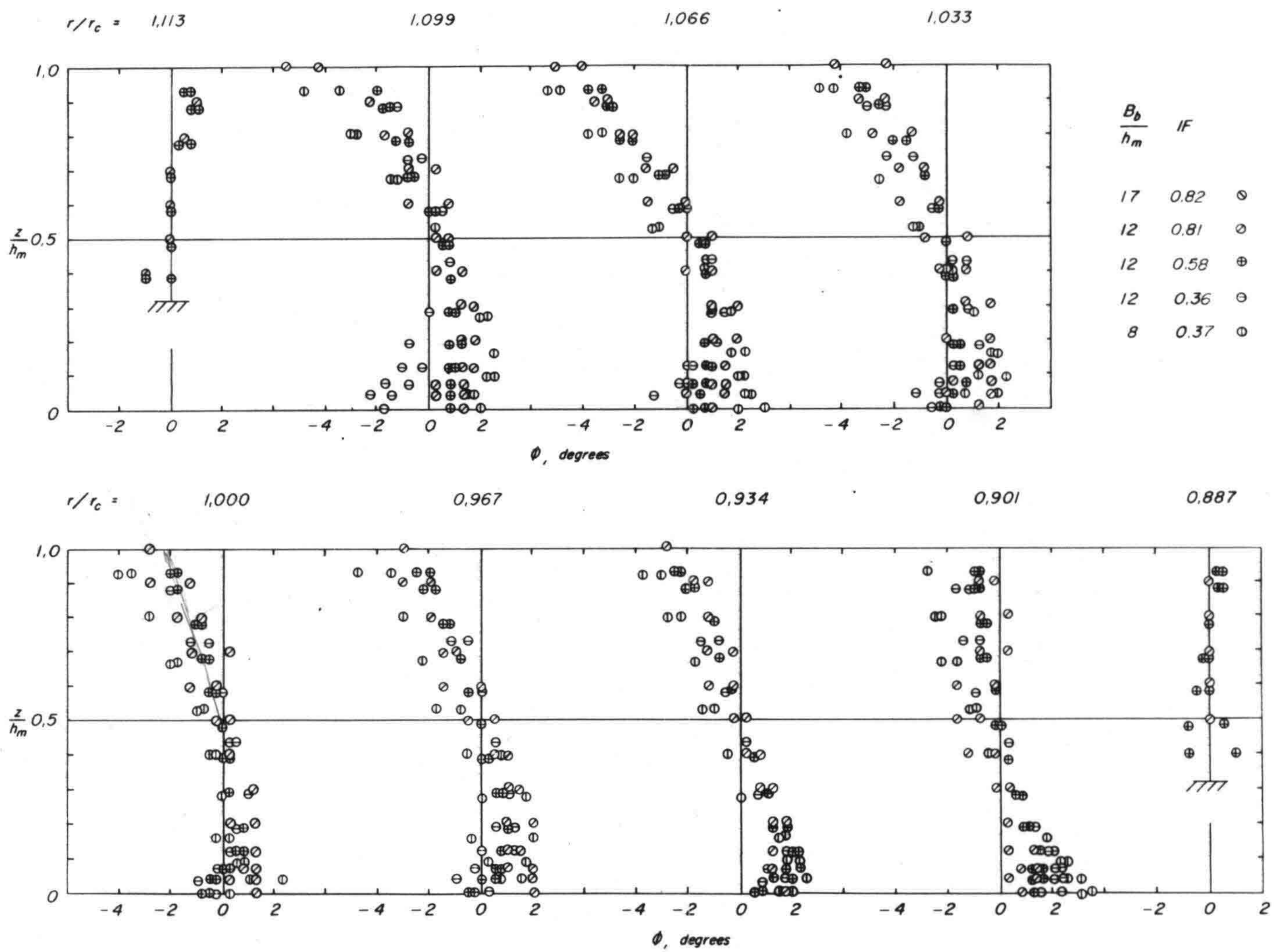

Fig. 13 (e) Section CIIO

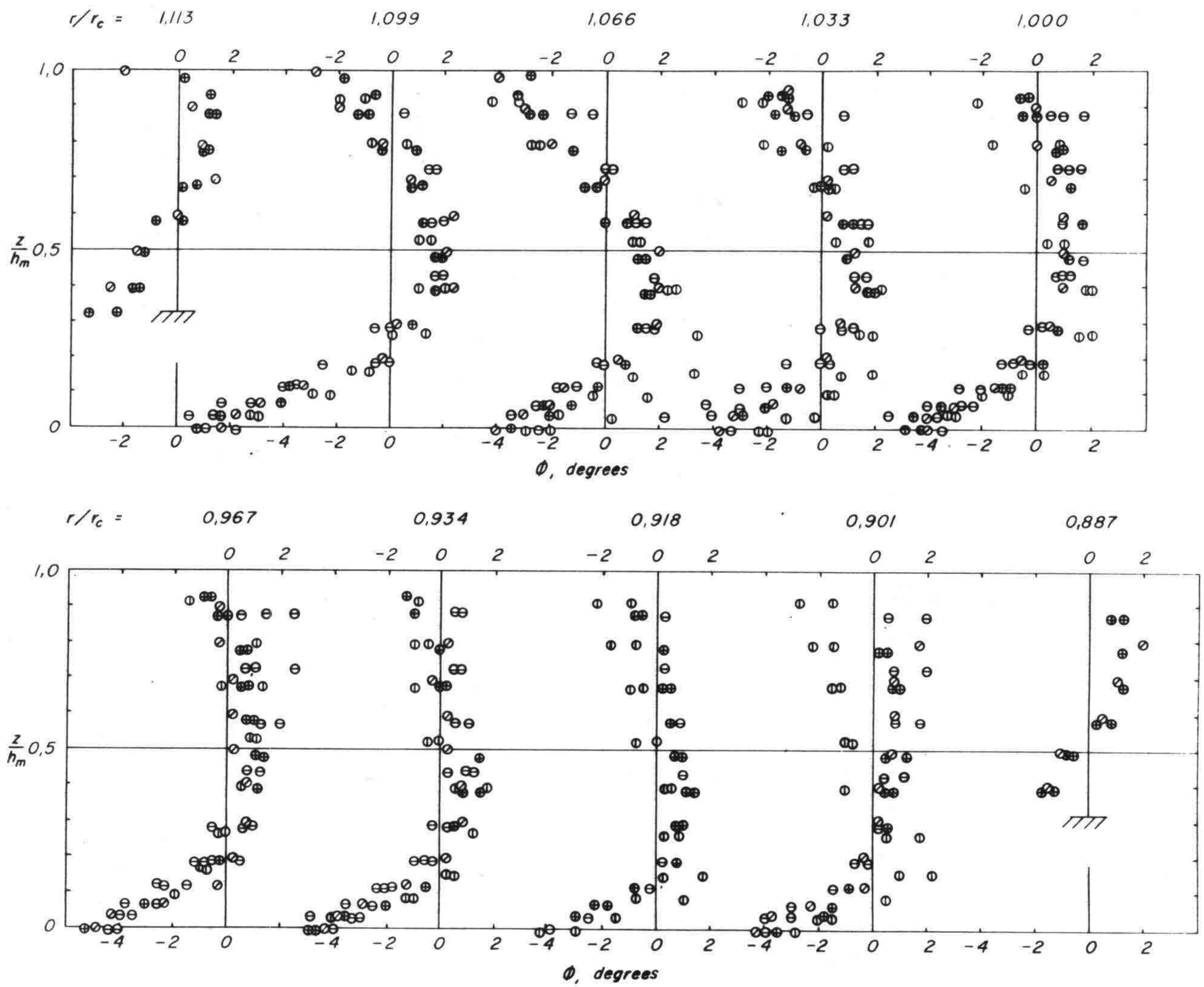

Fig. 13 (f) Section $\pi/16$

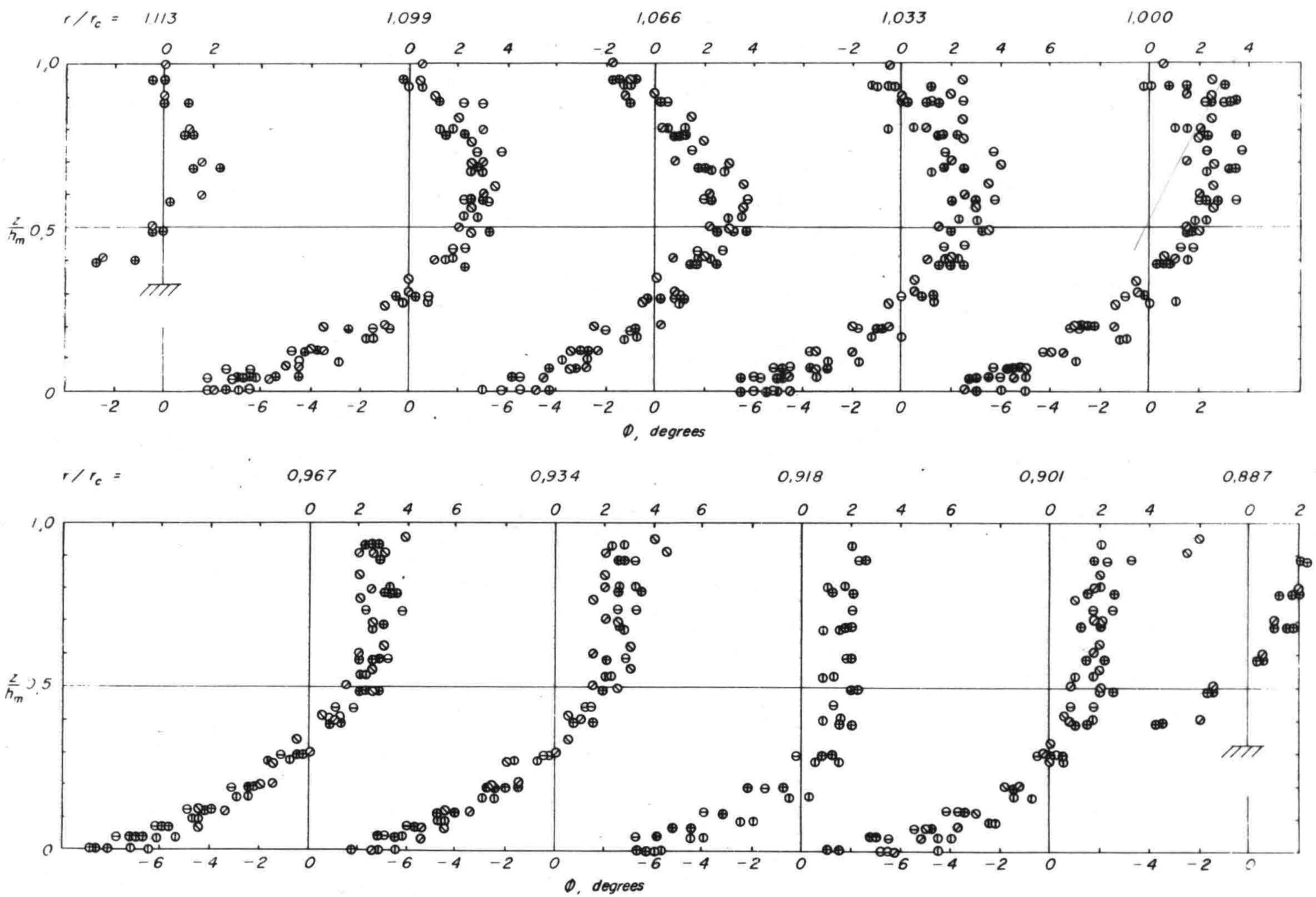

Fig. 13 (g) Section $\pi/8$

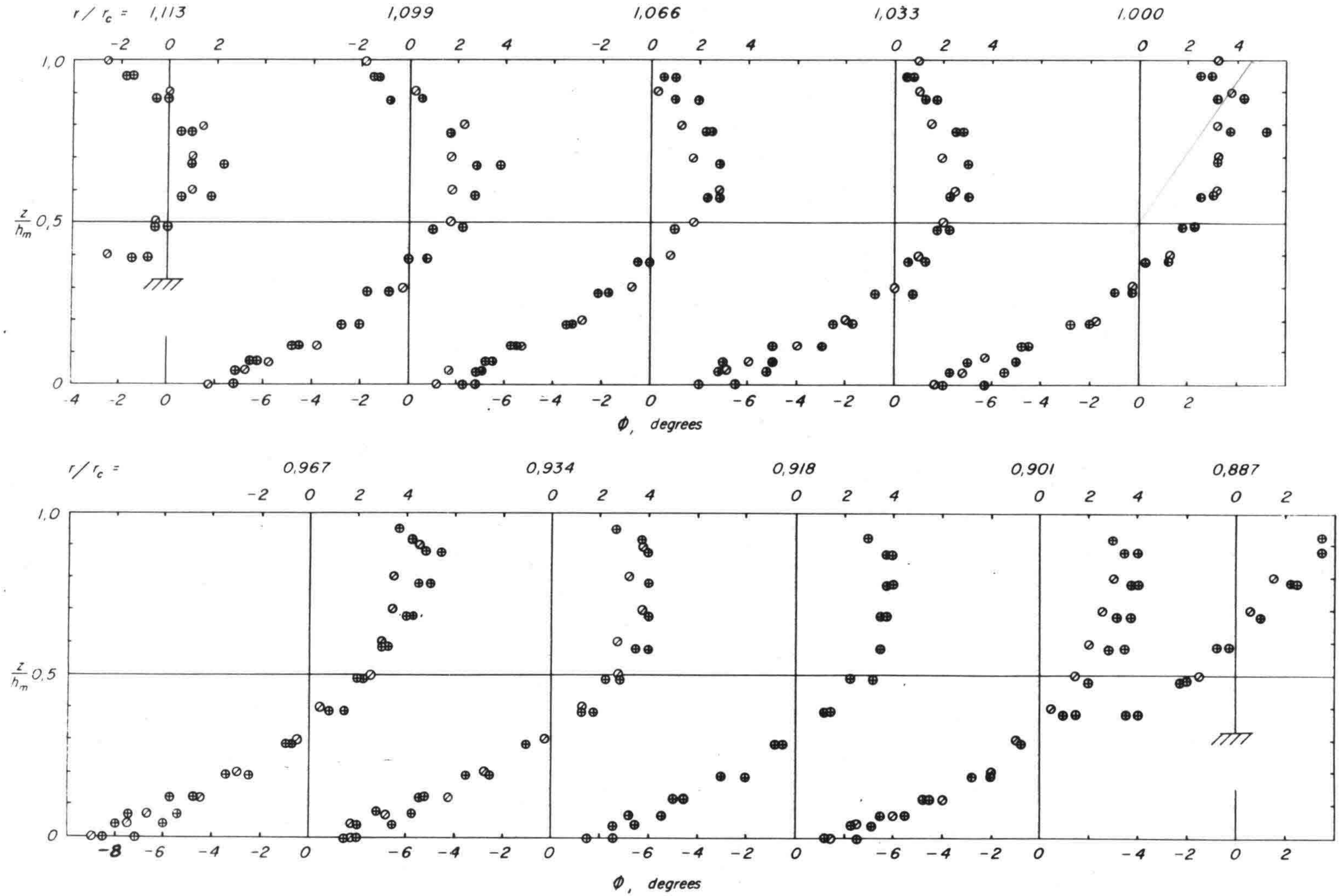

Fig, 13 (h) Section 3π/16

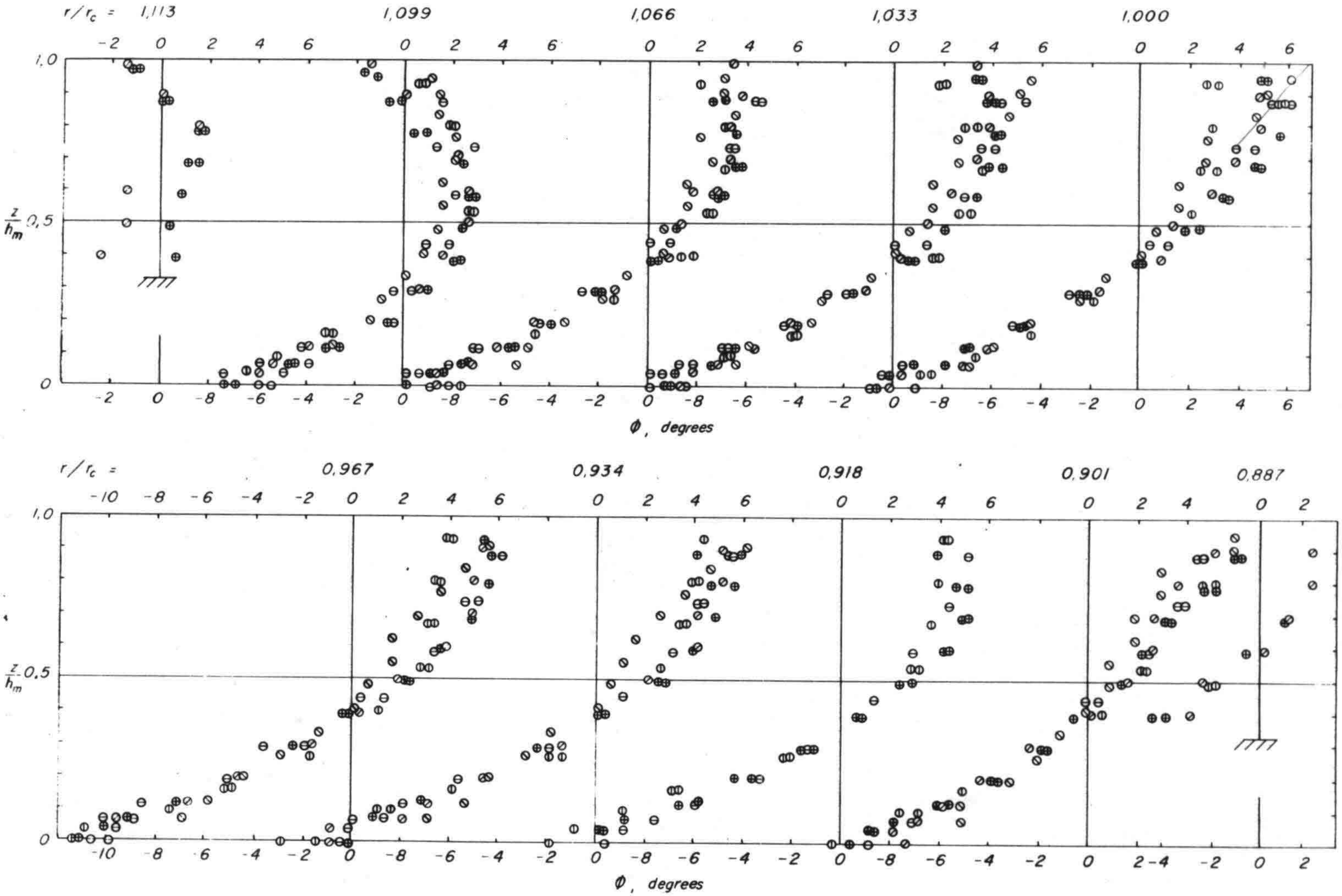

Fig, 13 (i) Section π/4

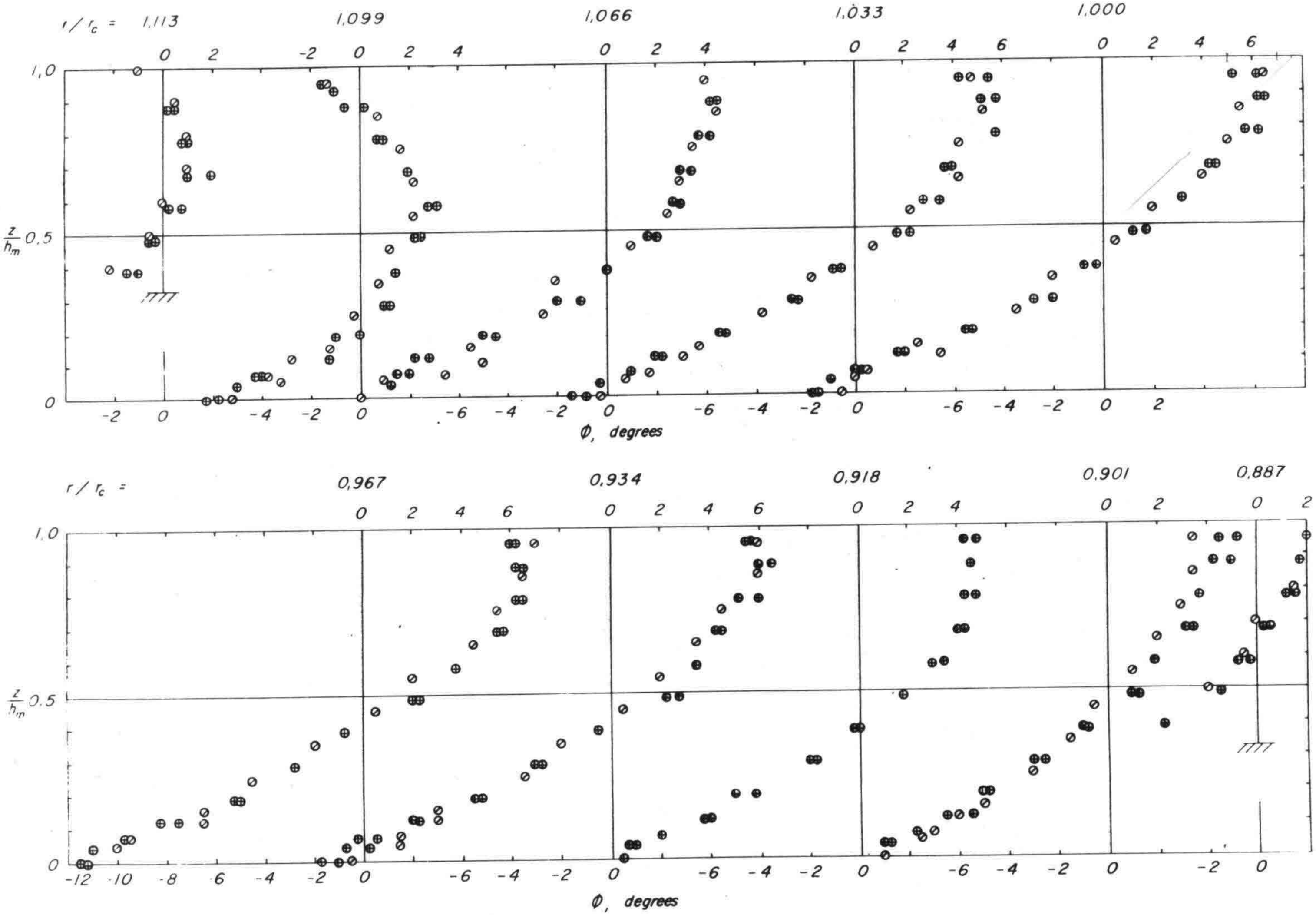

Fig. 13 (j) Section 5π/16

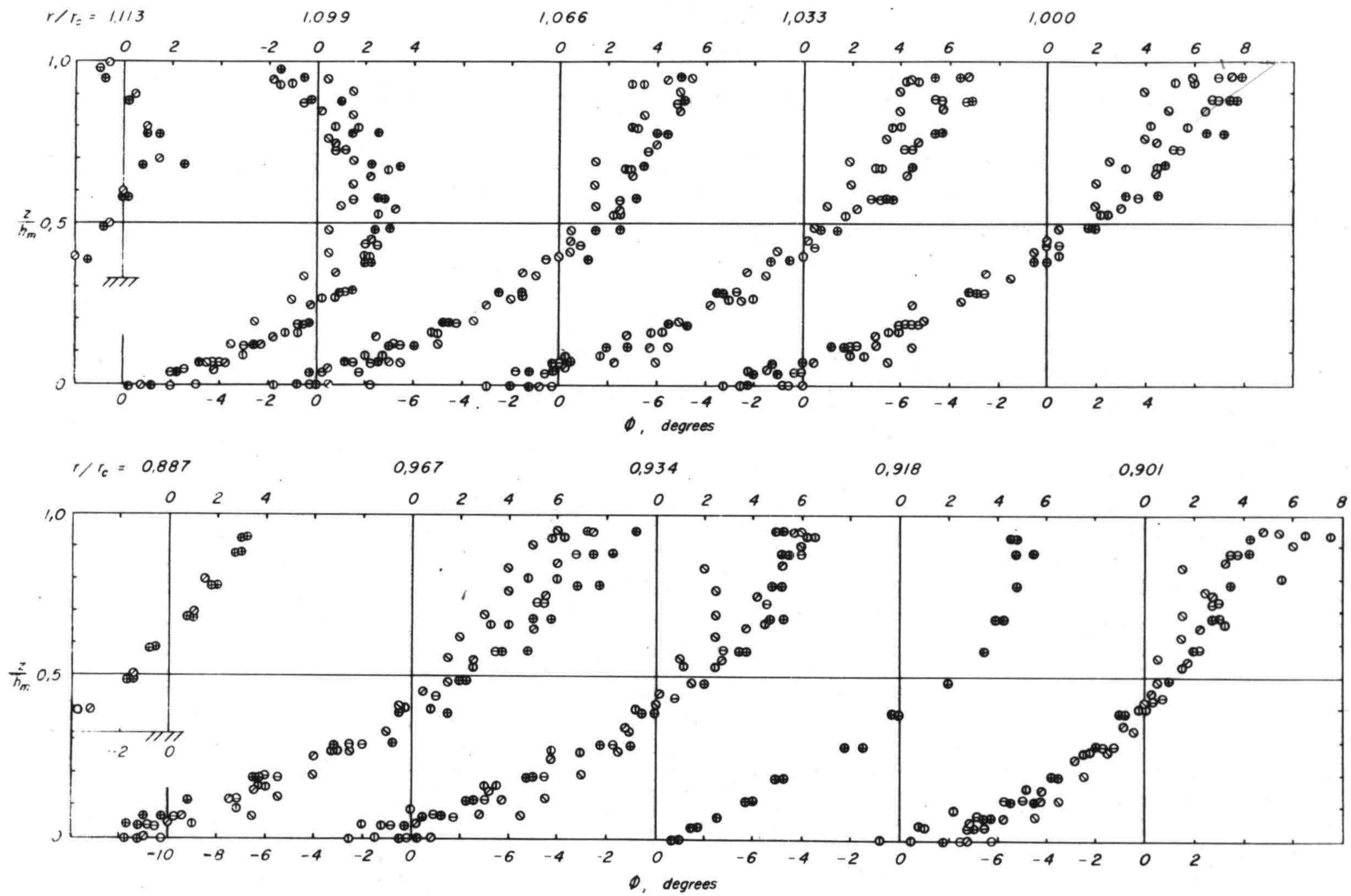

Fig. 13 (k) Section 3π/8

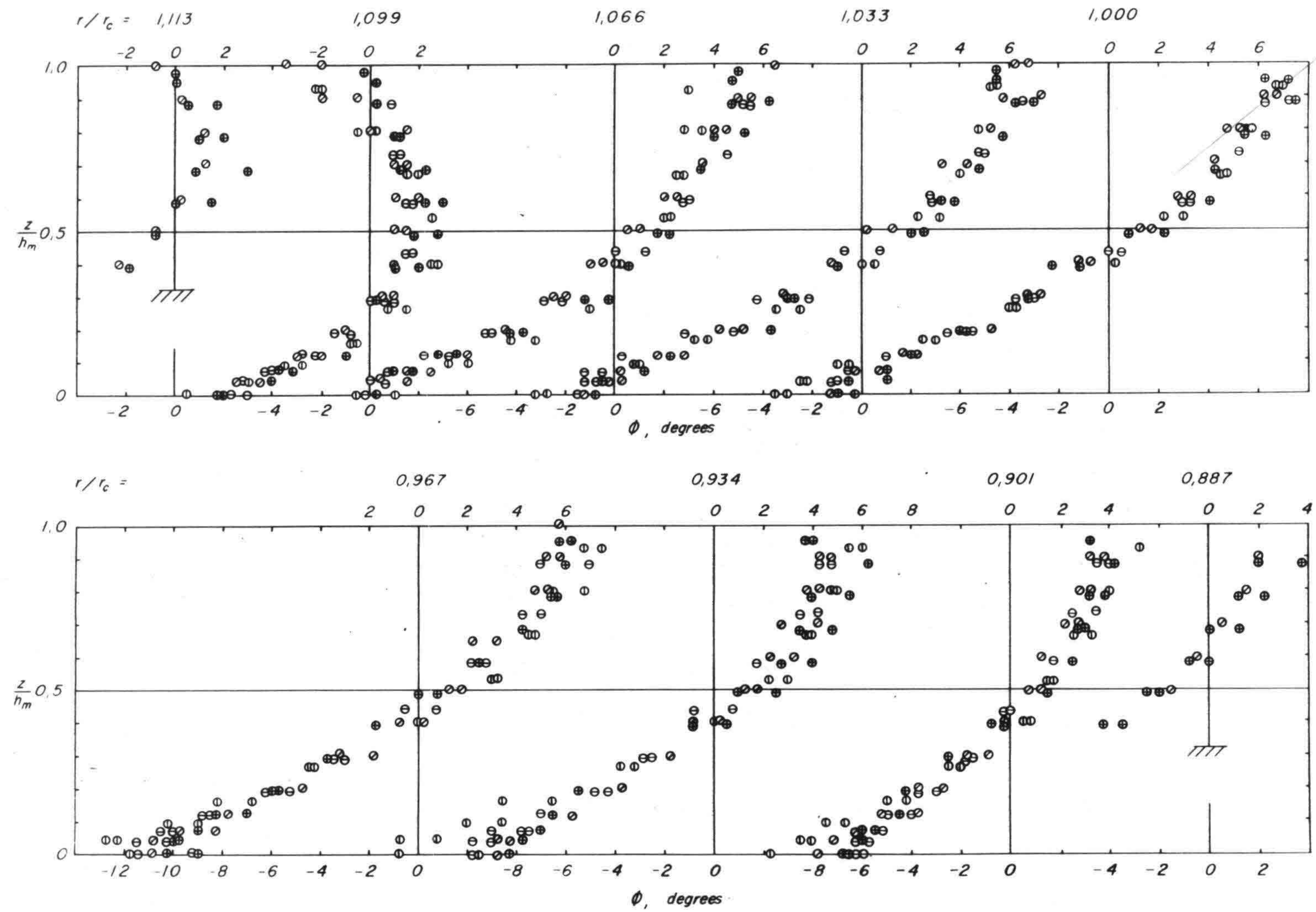

Fig. 13 (l) Section $7\pi/16$

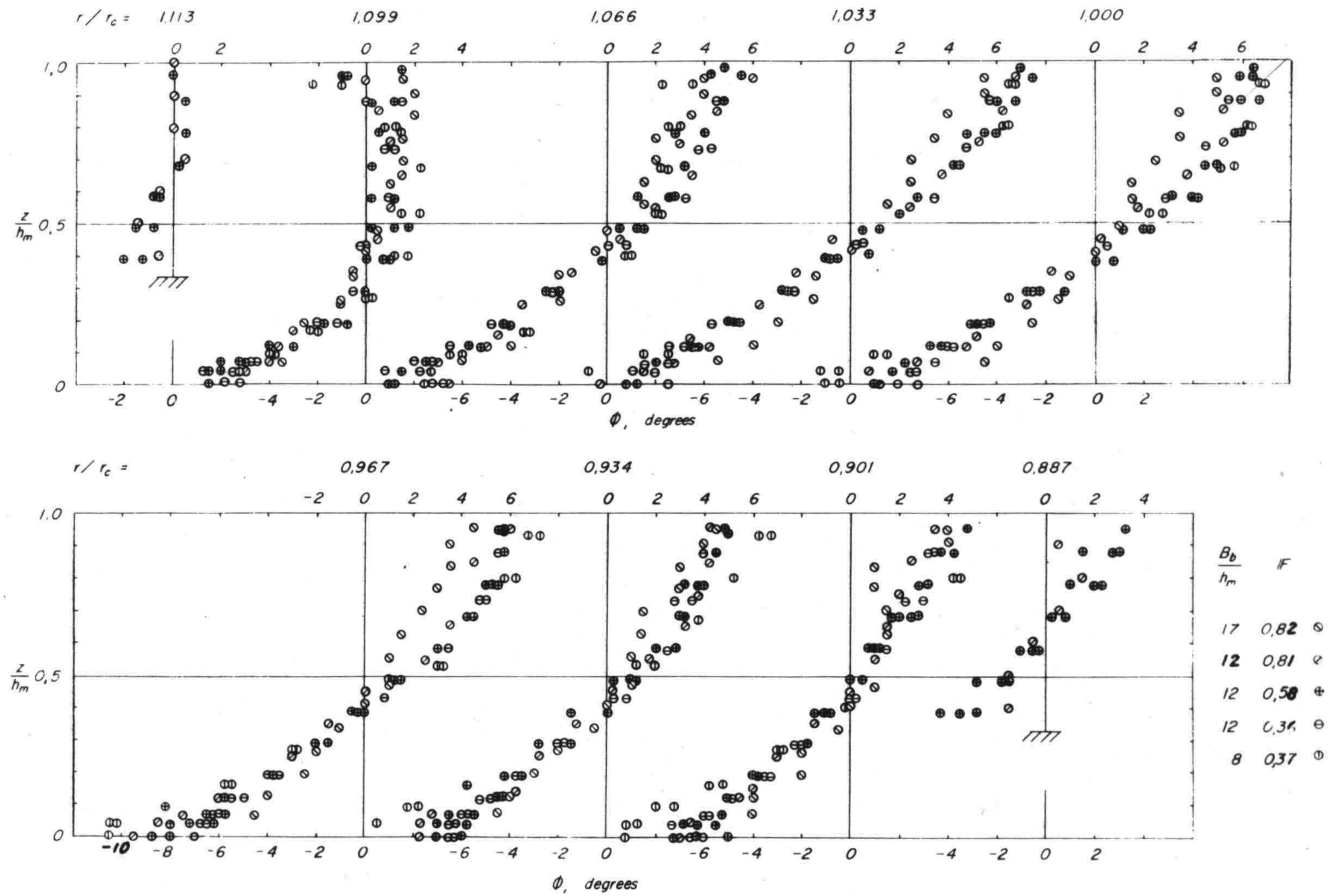

Fig. 13 (m) Section π/2

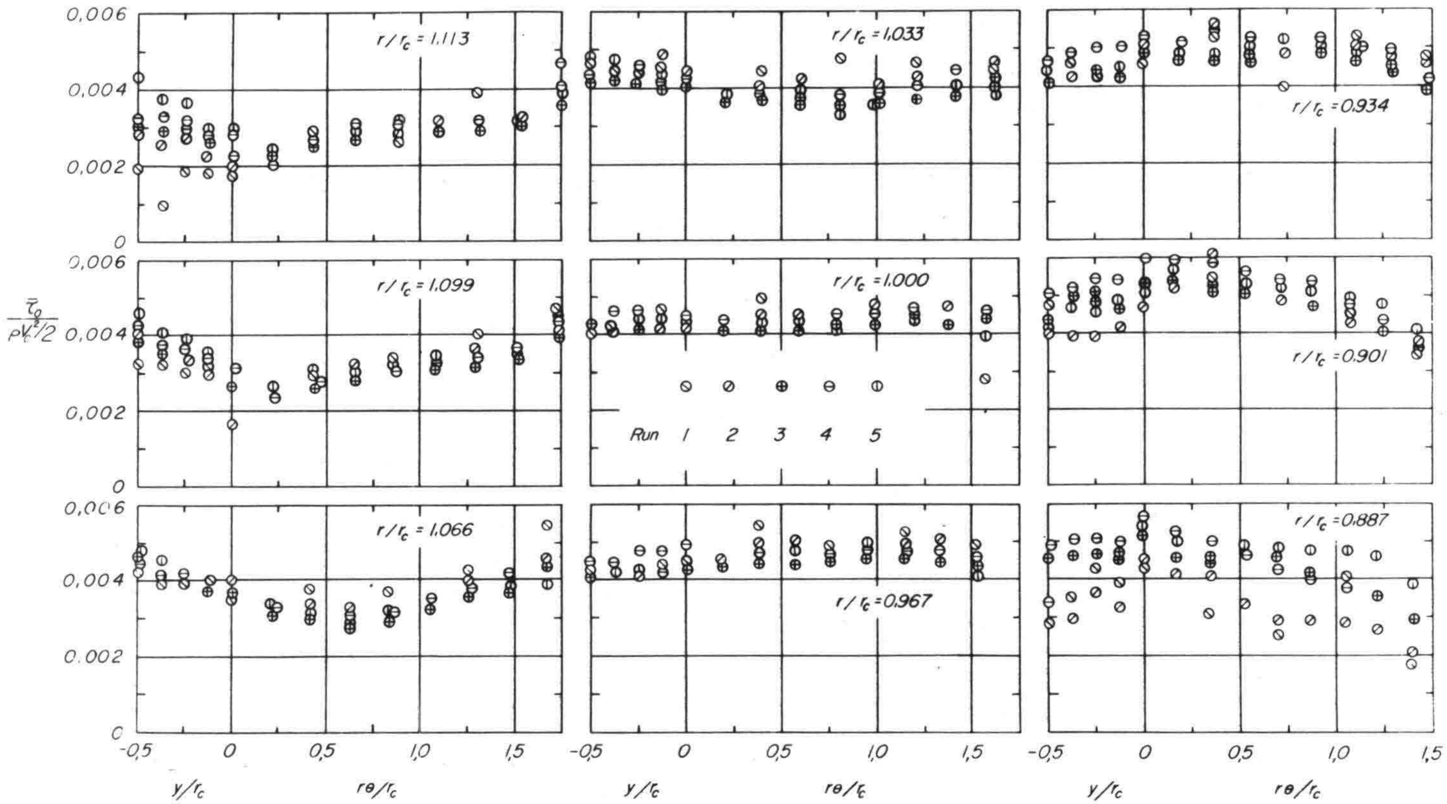

Fig. 14 Longitudinal Variation of $\bar{\tau}_o / \frac{1}{2} \rho V_o^2$

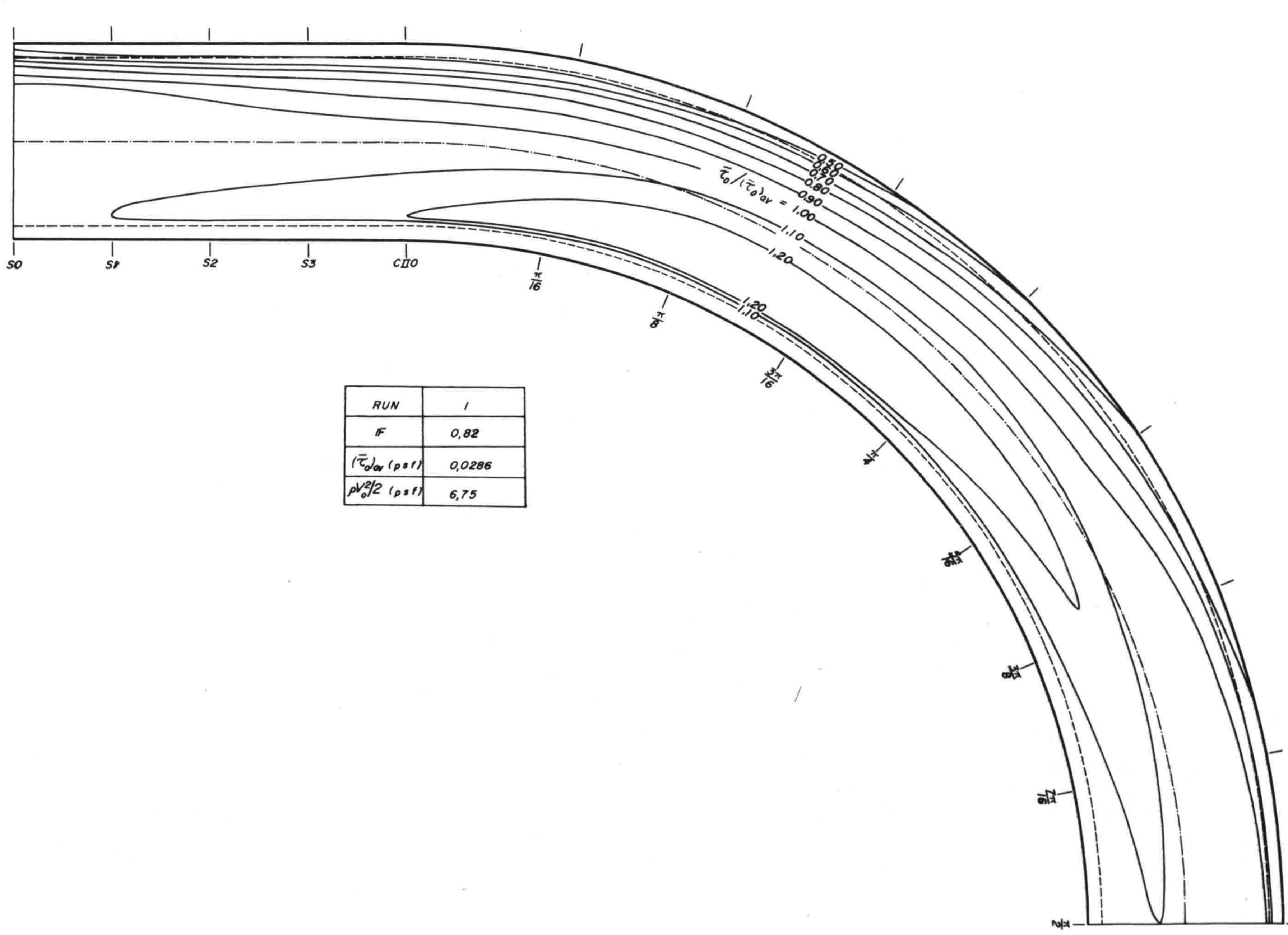

RUN	1
IF	0,82
$(\bar{\tau}_0)_{av}$ (psf)	0,0286
$\rho V_0^2/2$ (psf)	6,75

Fig, 15 Boundary Shear Contours, (a)

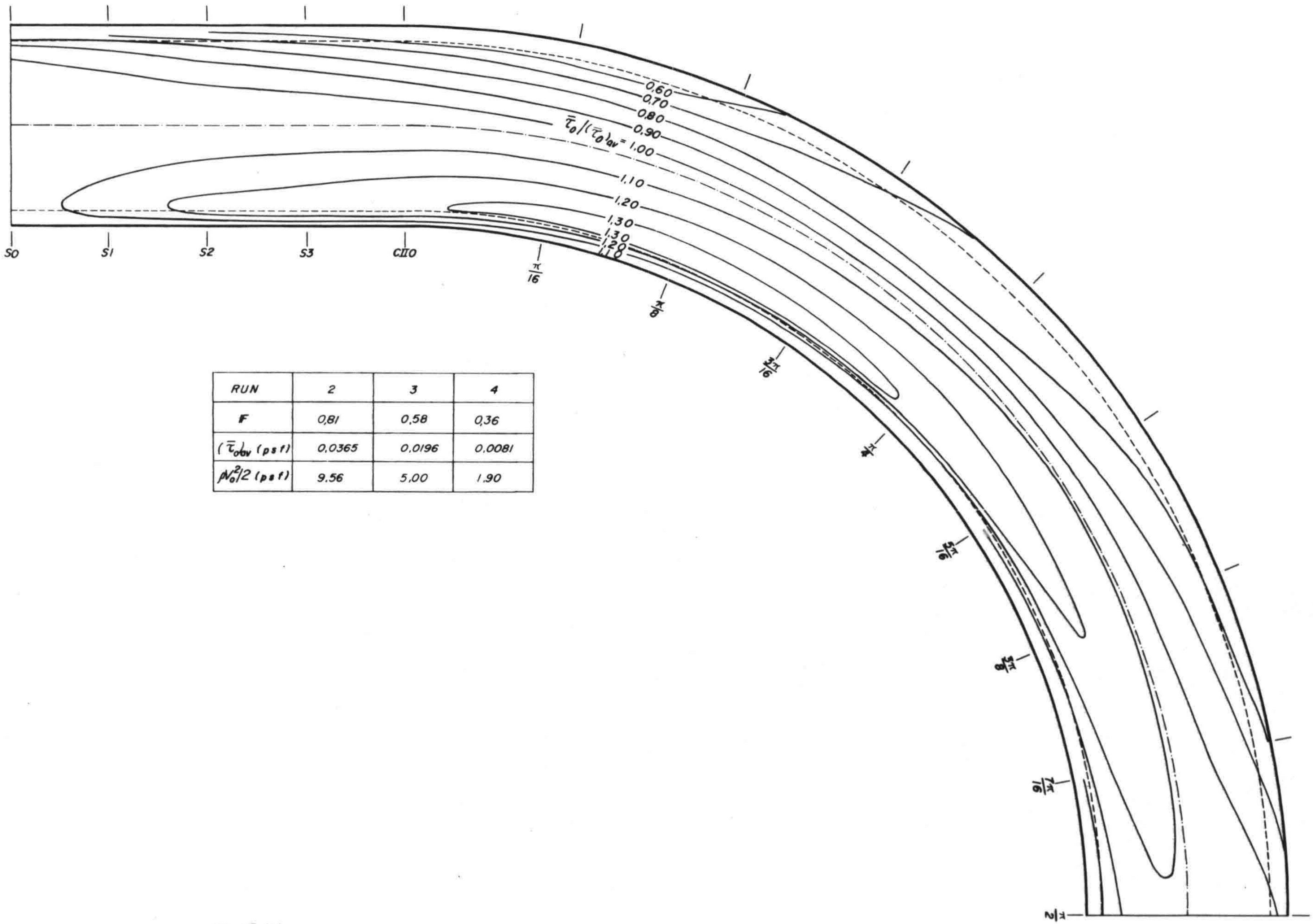

RUN	2	3	4
F	0,81	0,58	0,36
$(\bar{\tau}_0)_{av}$ (psf)	0,0365	0,0196	0,0081
$\rho V_0^2/2$ (psf)	9.56	5,00	1.90

Fig, 15 (b)

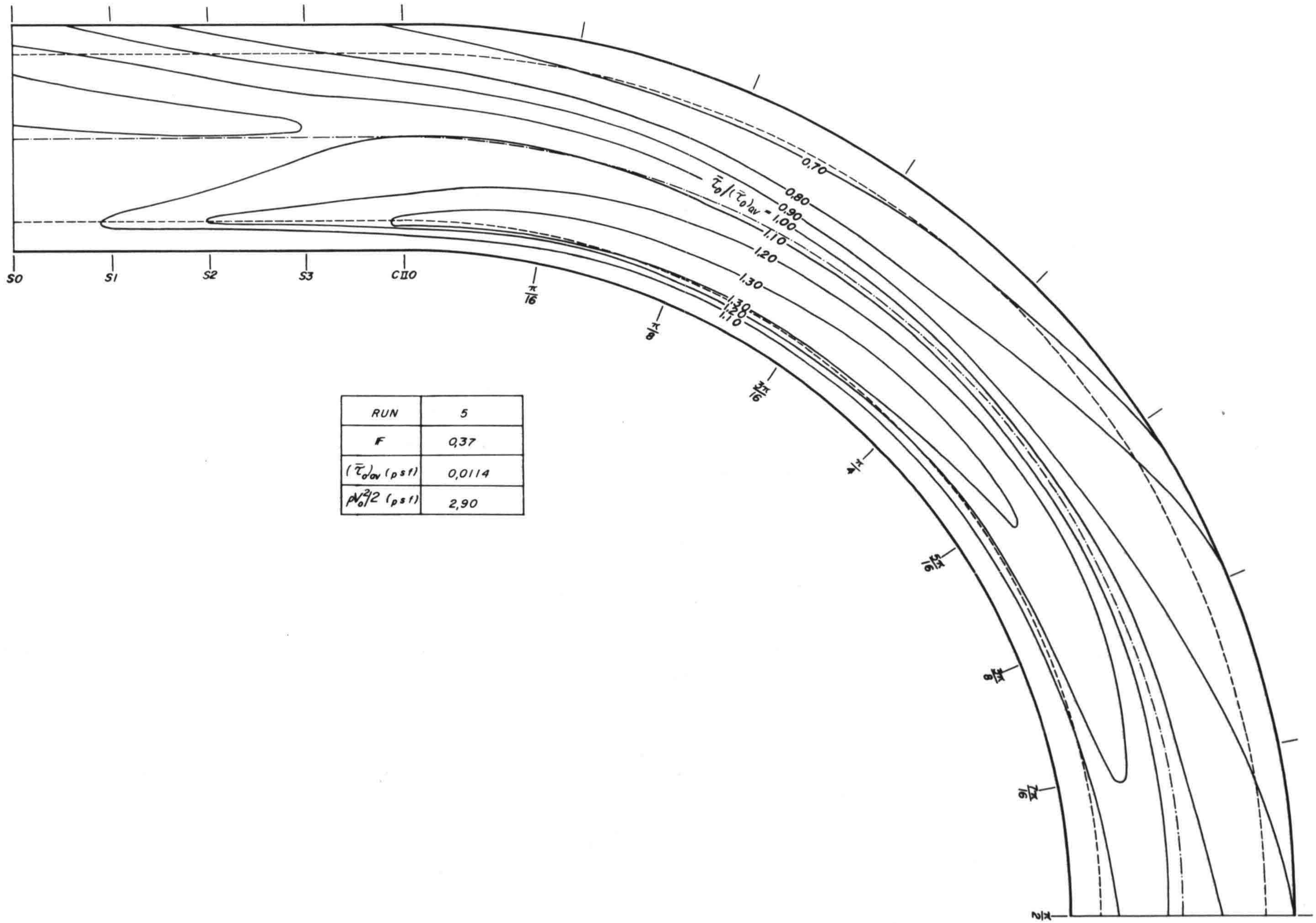

RUN	5
F	0,37
$(\bar{\tau}_0)_{av}$ (psf)	0,0114
$\rho V_0^2/2$ (psf)	2,90

Fig, 15 (c)

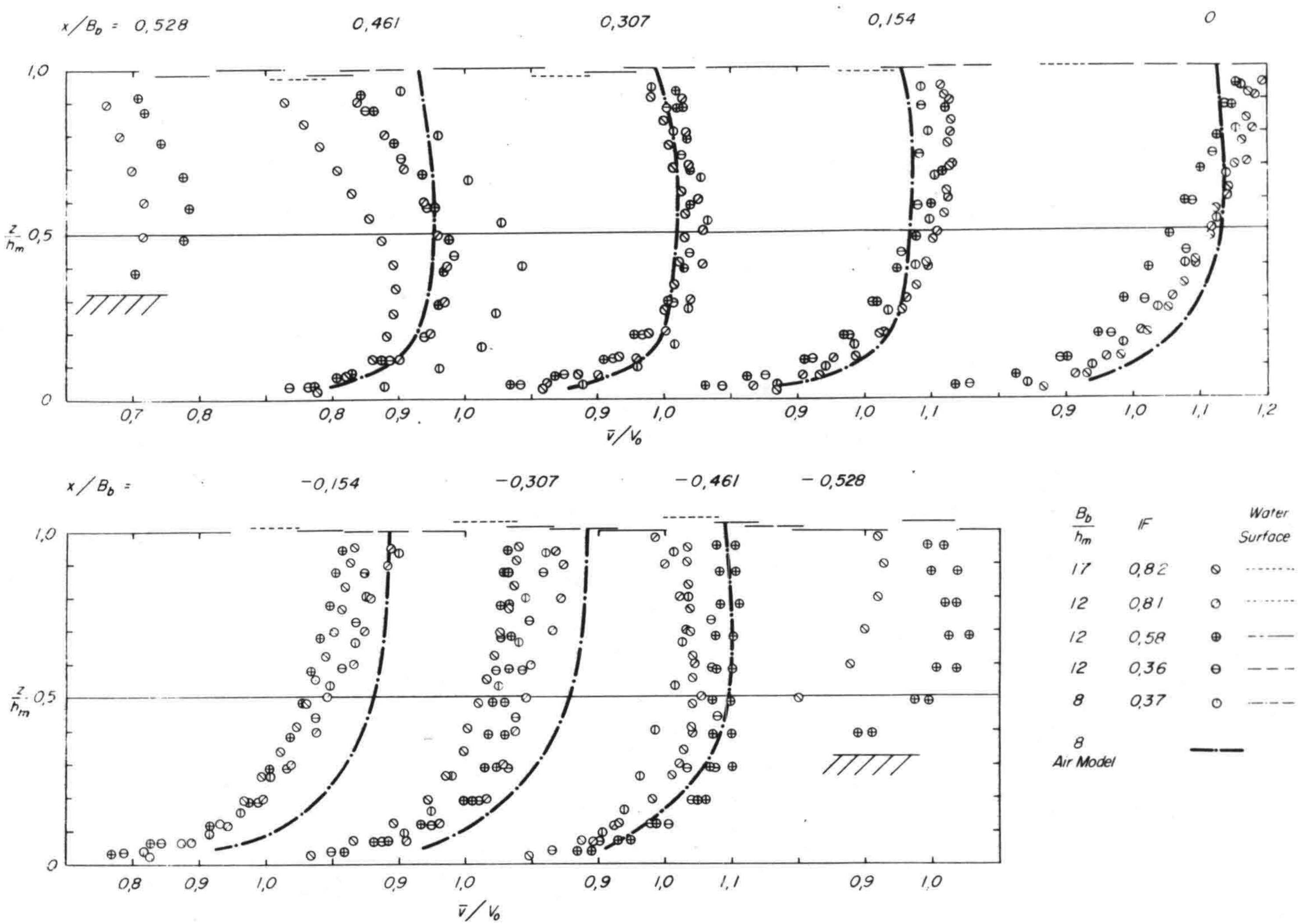

Fig. 16 Mean-velocity Distribution Along Verticals, (a) Section SO

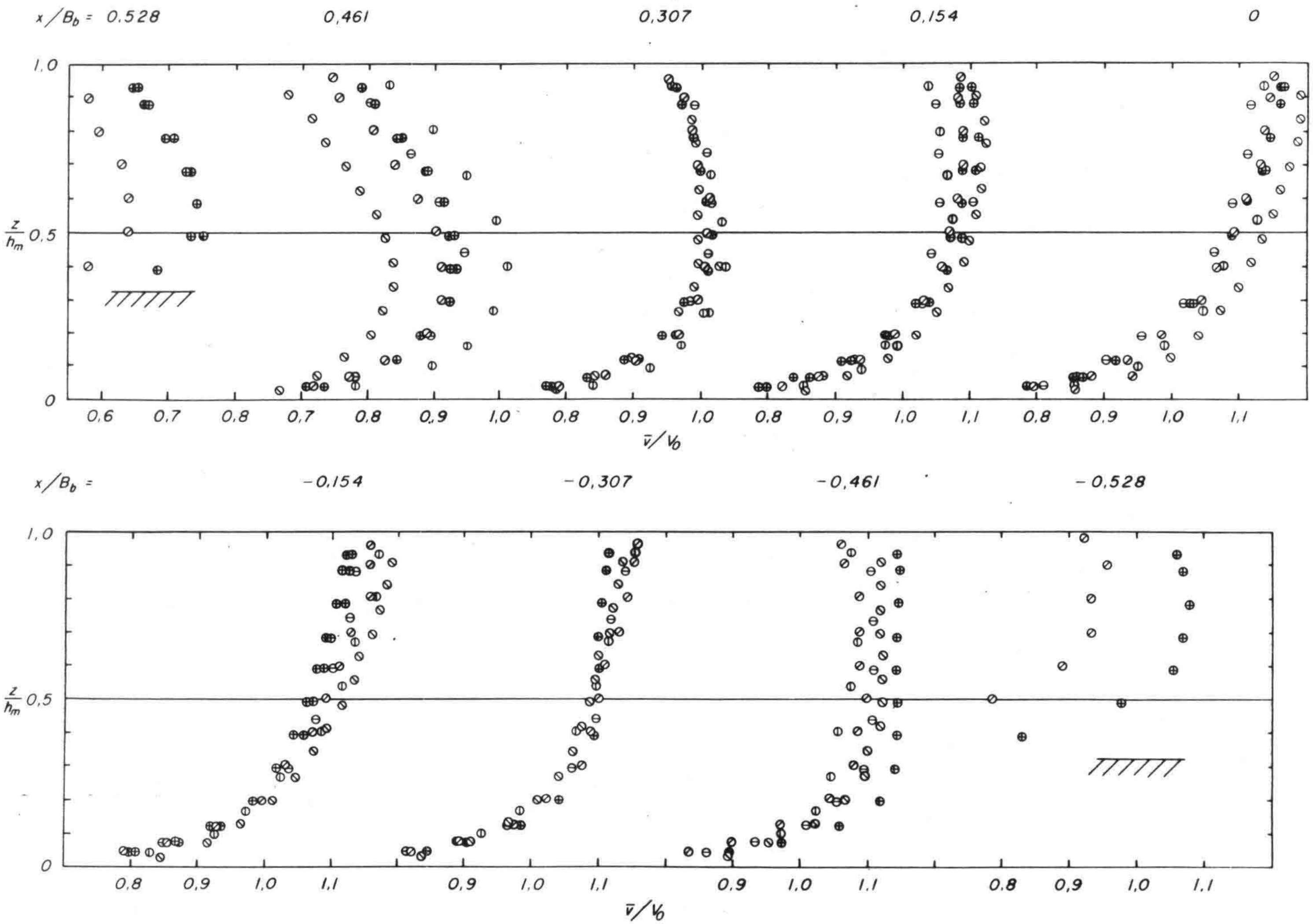

Fig. 16 (b) Section S1

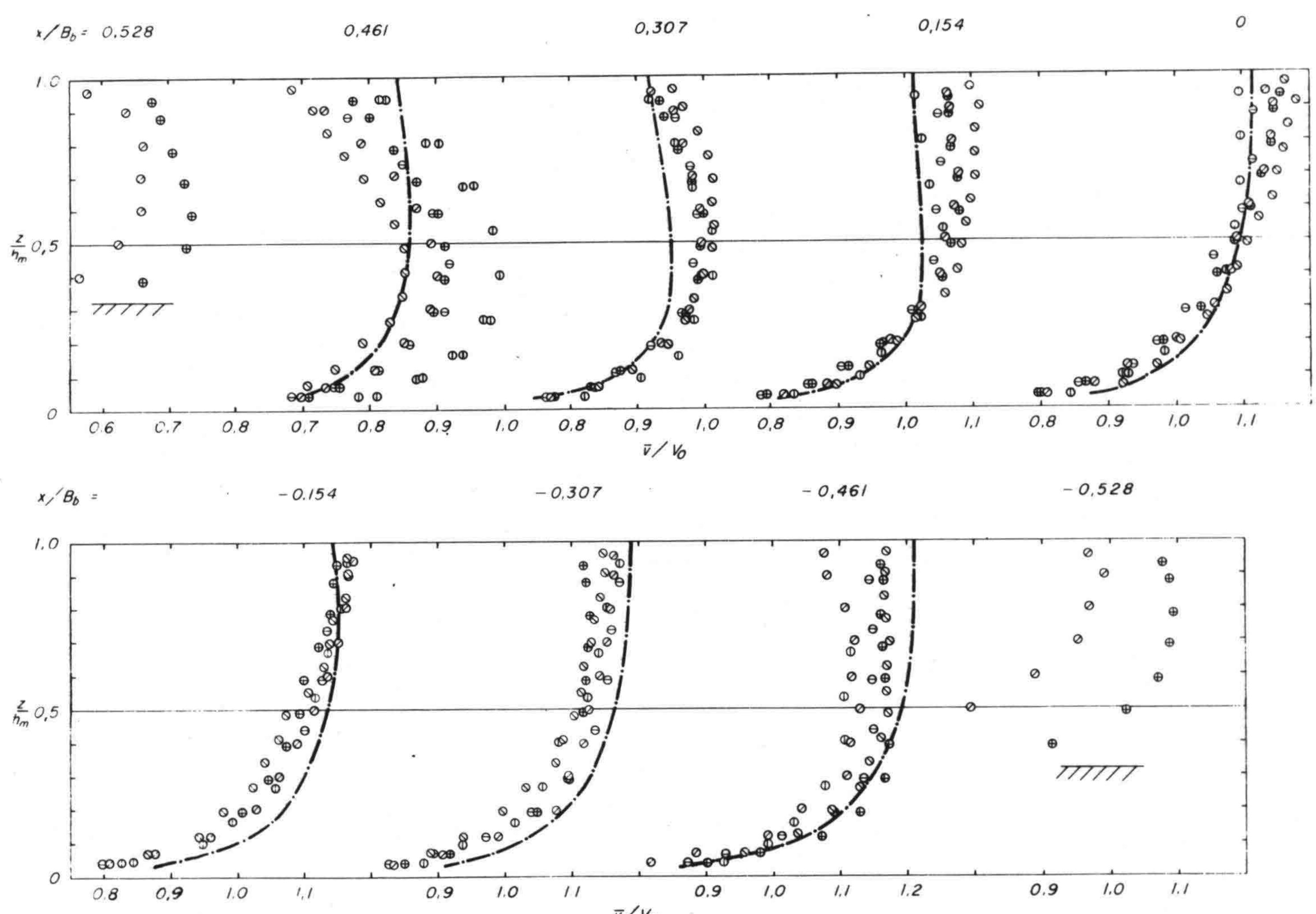

Fig. 16 (c) Section S2

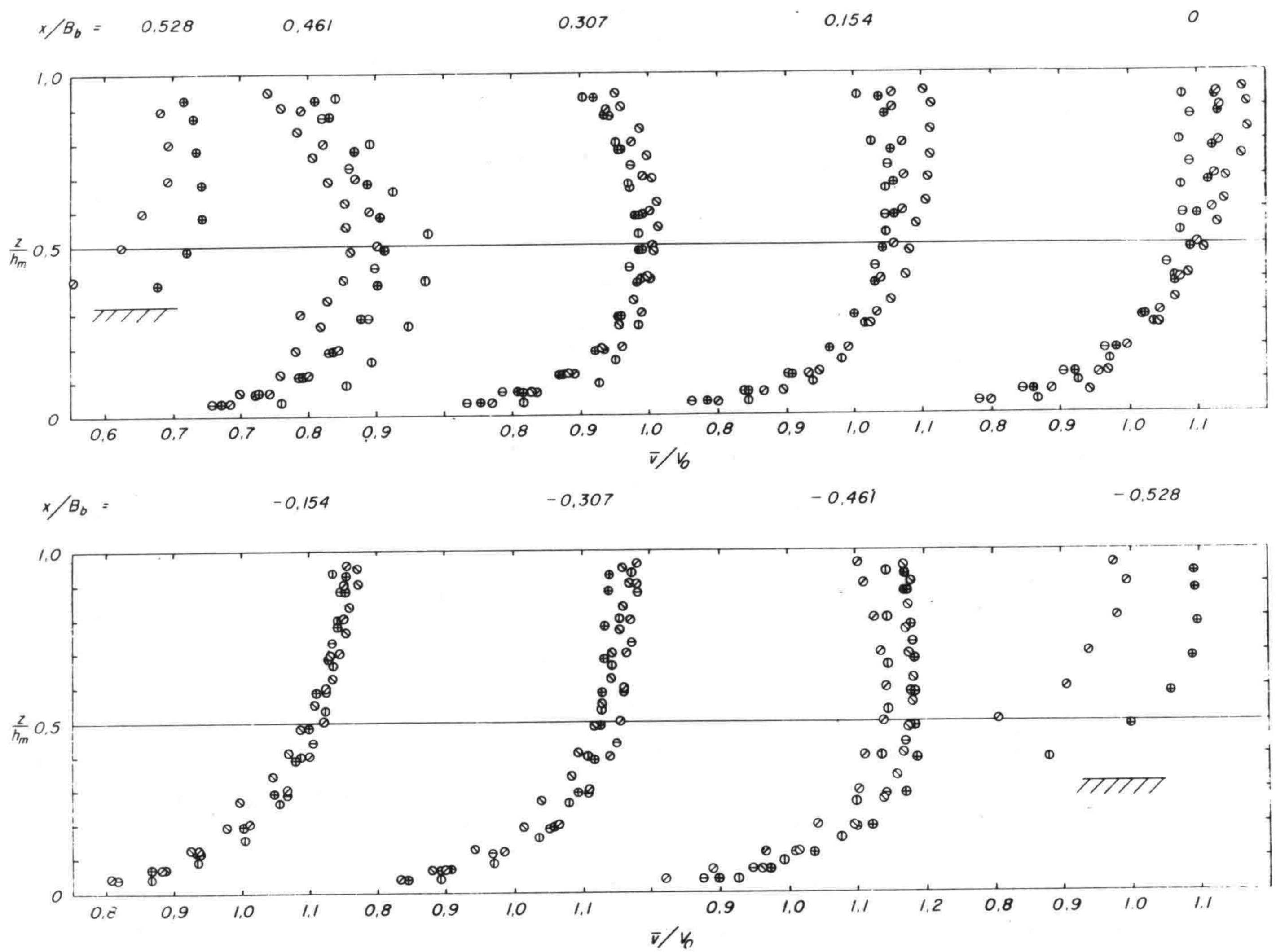

Fig. 16(d) Section S3

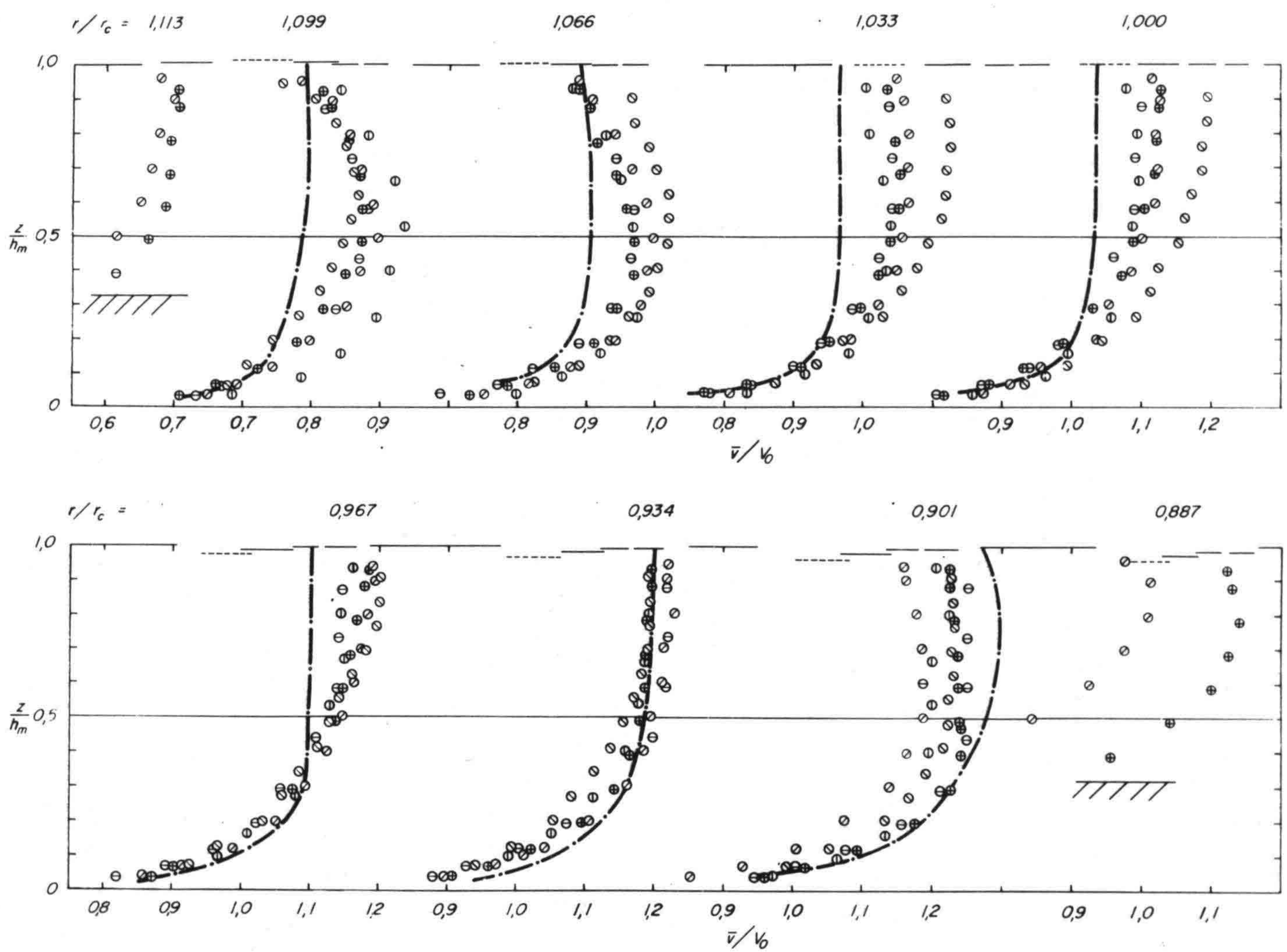

Fig, 16 (e) Section CIIO

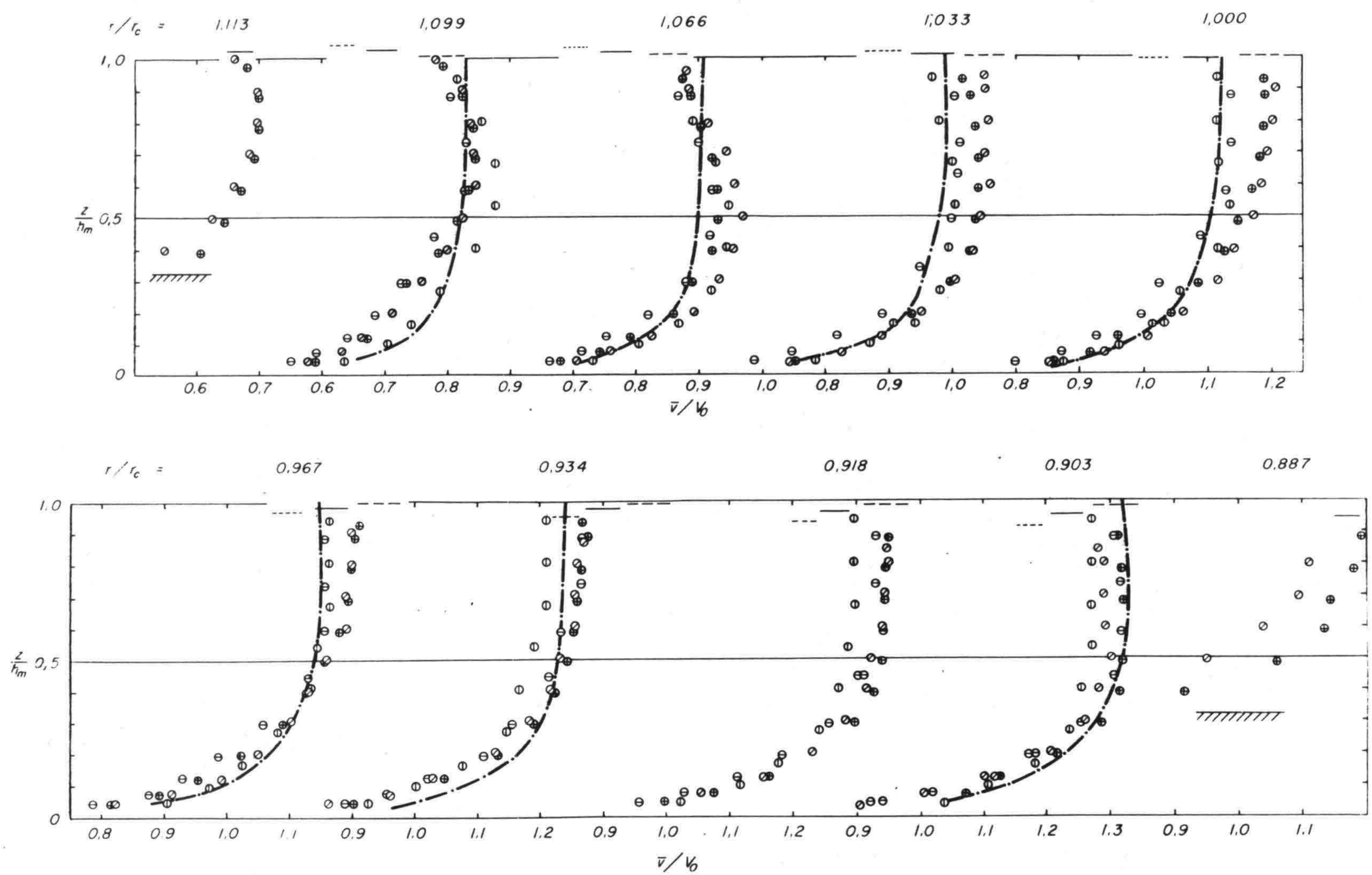

Fig. 16 (f) Section π/16

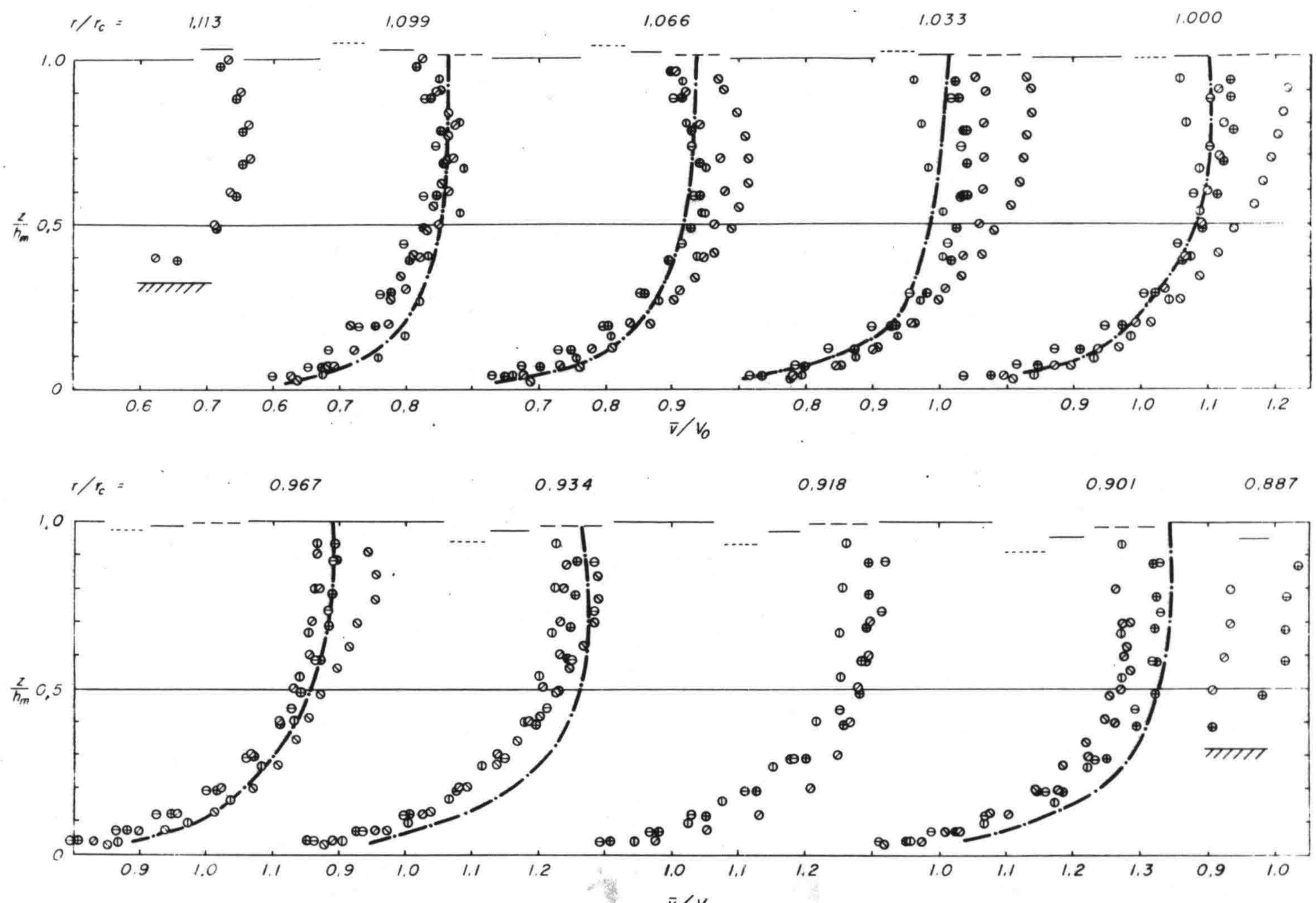

Fig. 16 (g) Section $\pi/8$

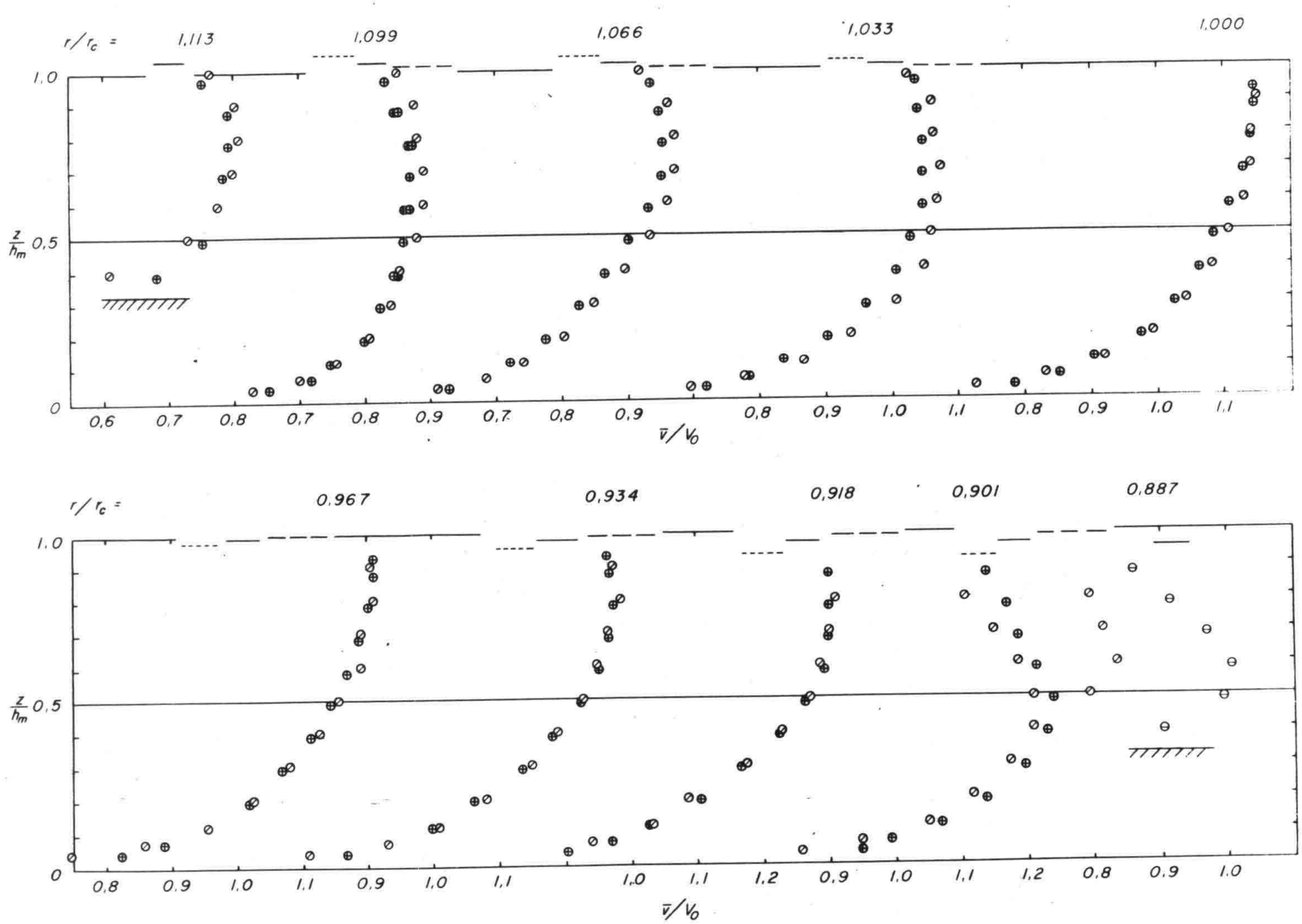

Fig. 16 (h) Section $3\pi/16$

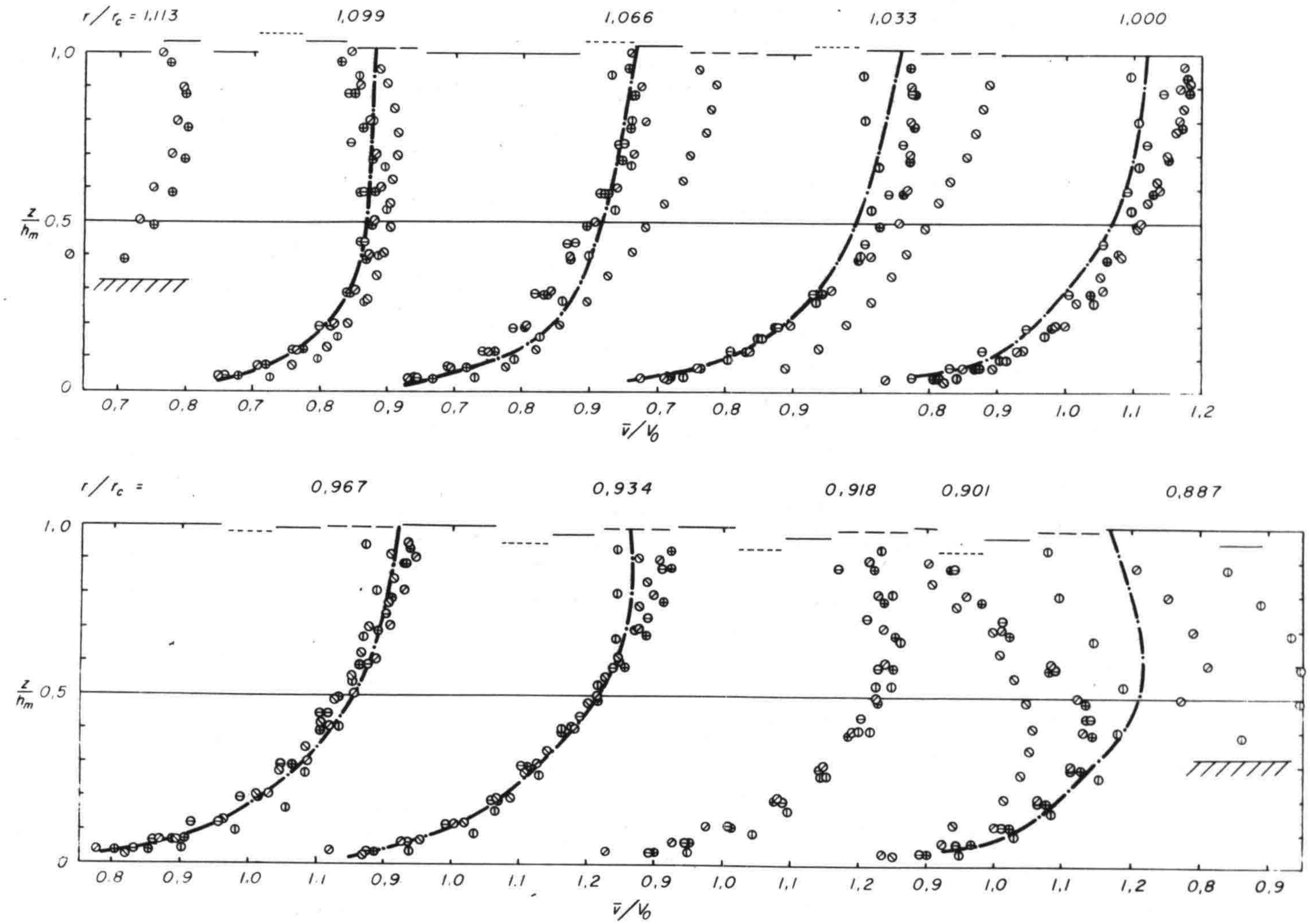

Fig, 16 (i) Section $\pi/4$

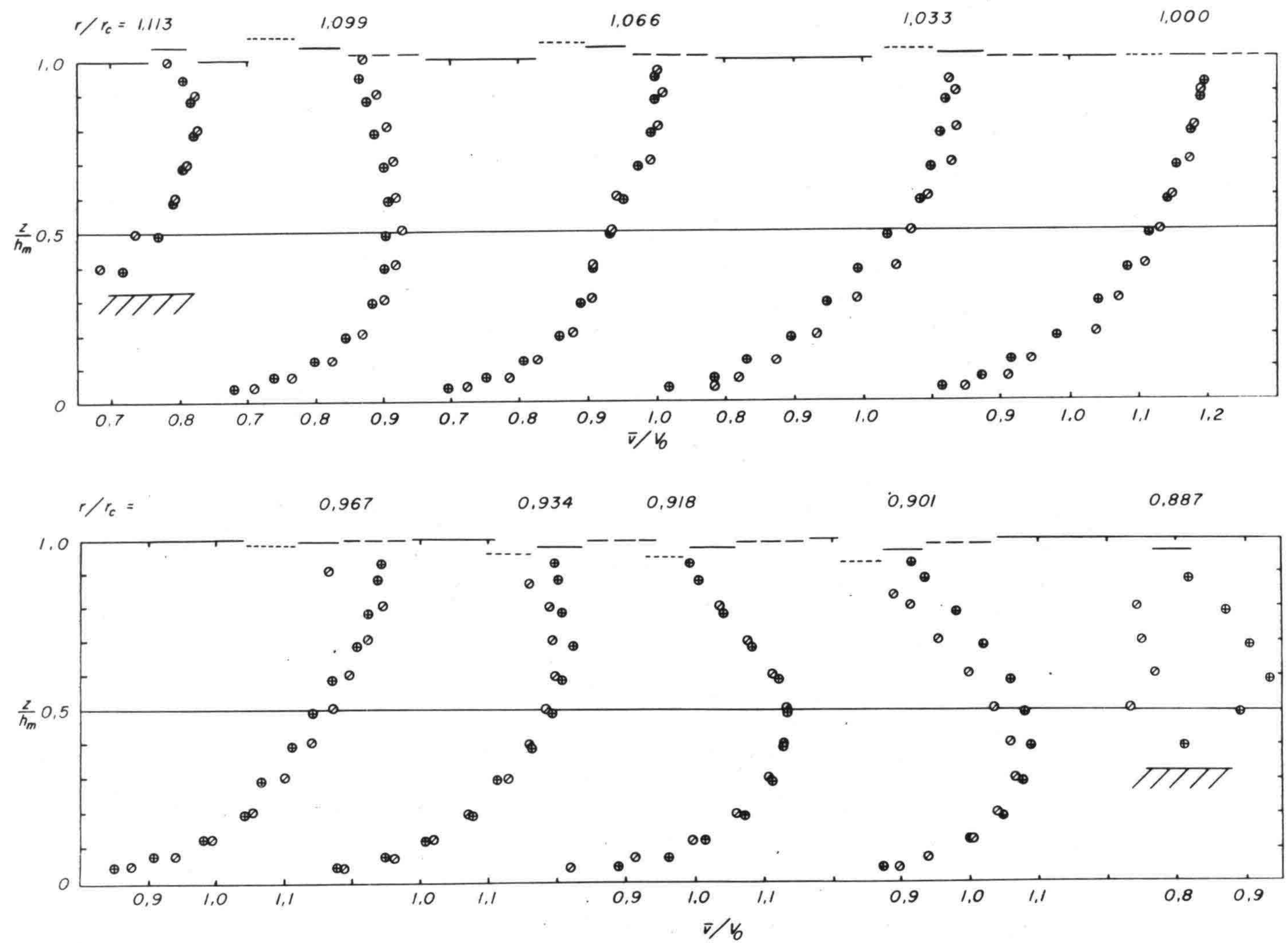

Fig, 16 (j) Section $5\pi/16$

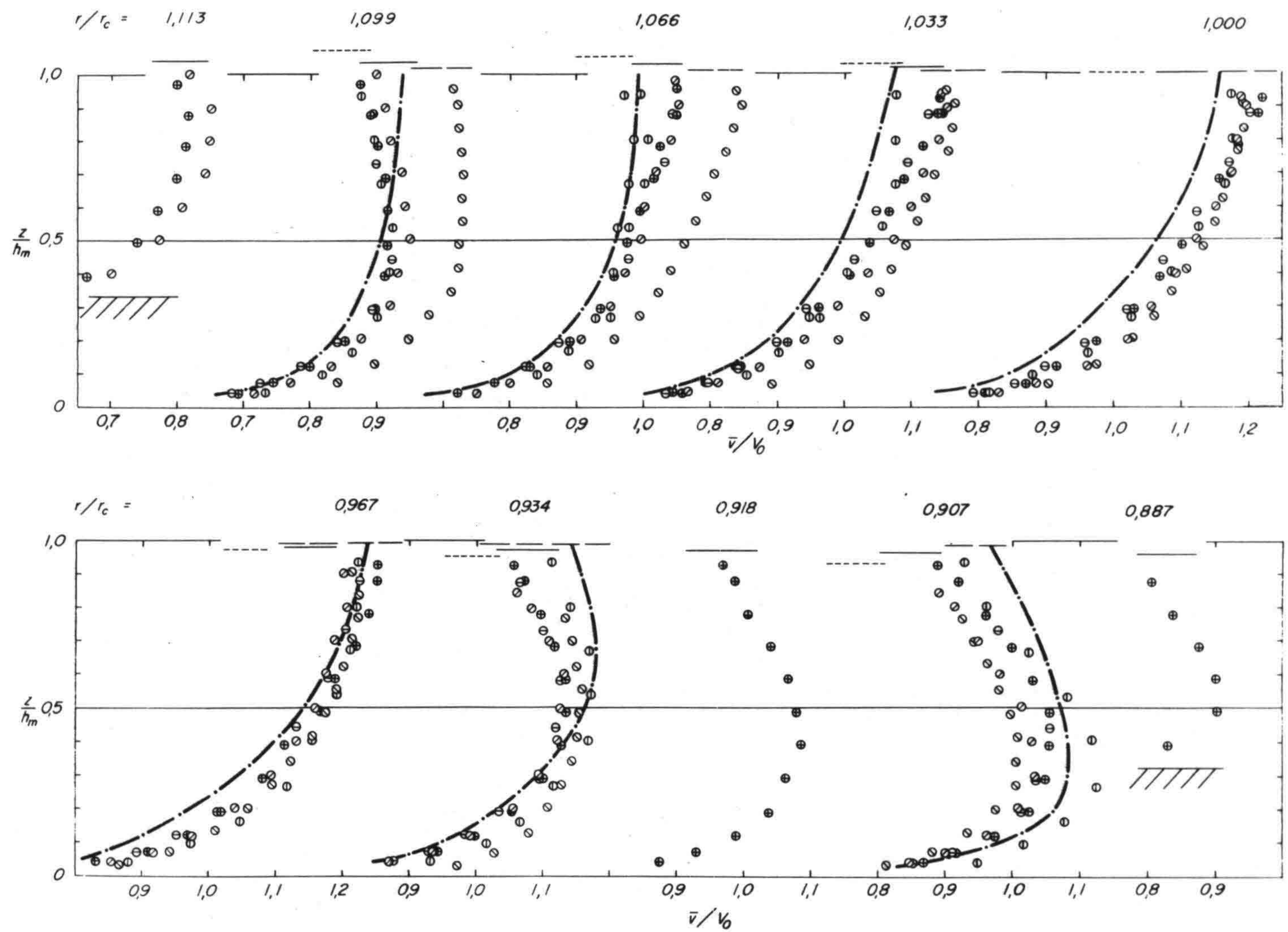

Fig, 16 (k) Section $3\pi/8$

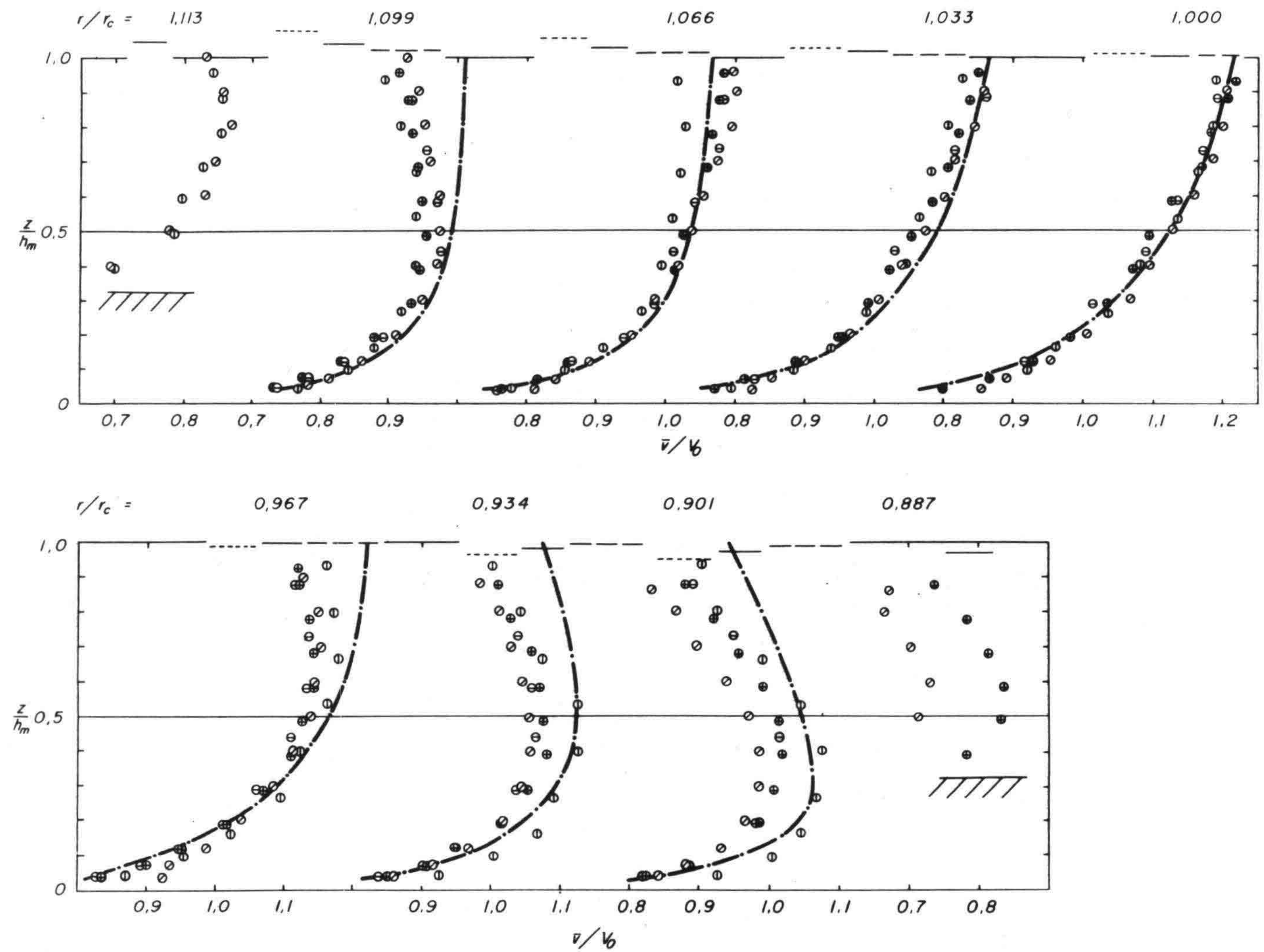

Fig. 16 (1) Section $7\pi/16$

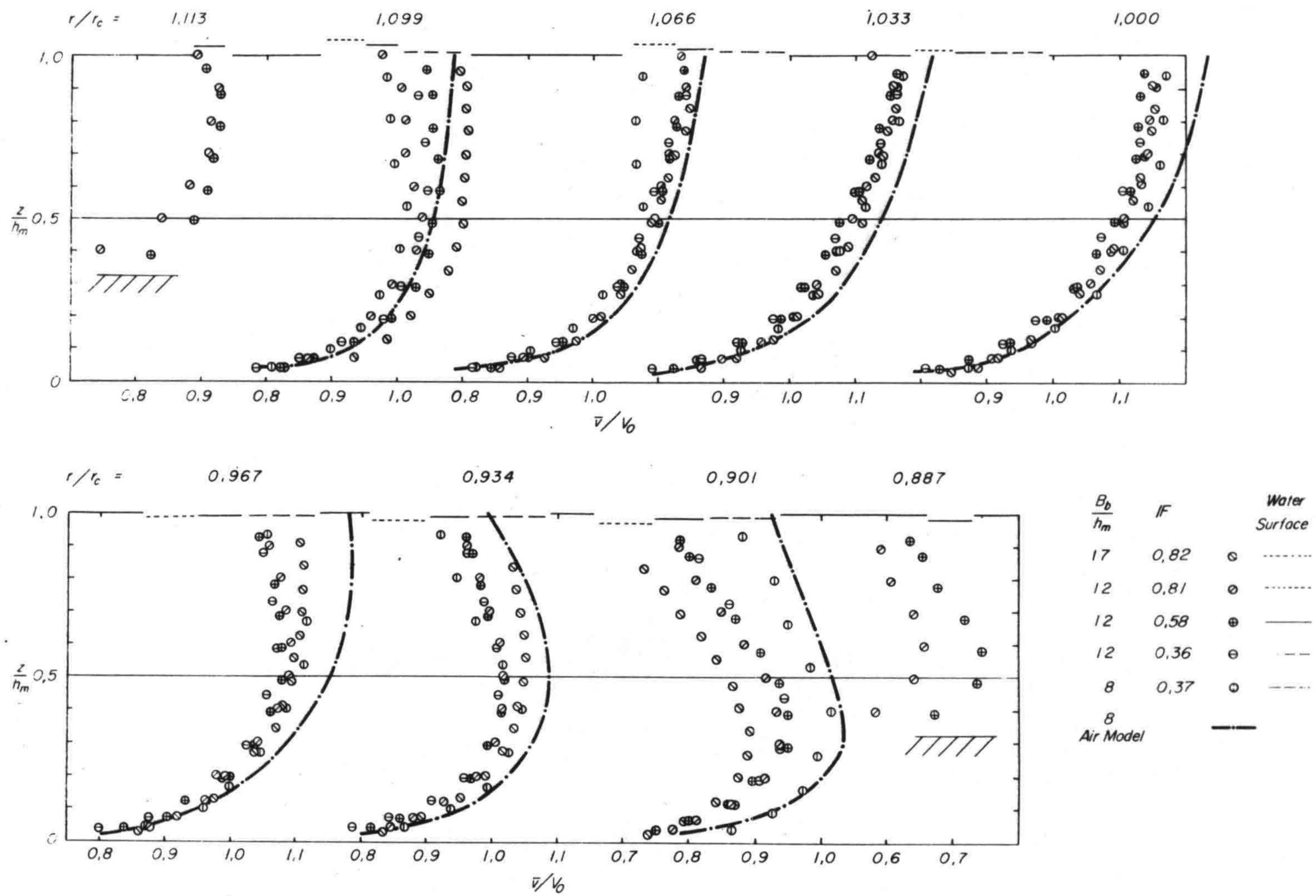

Fig, 16 (m) Section $\pi/2$

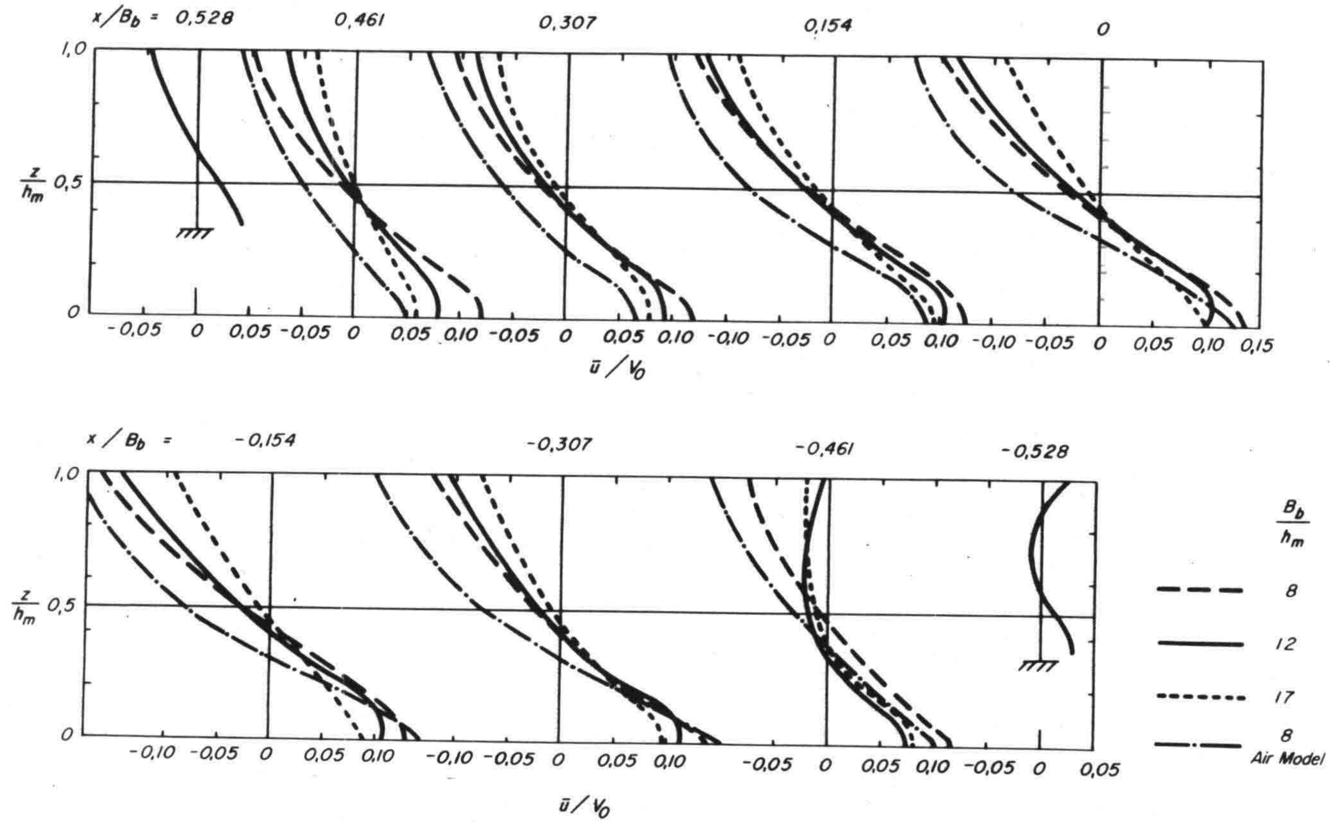

Fig. 17 Distribution of Radial Mean-velocity Component, (a) Section SO

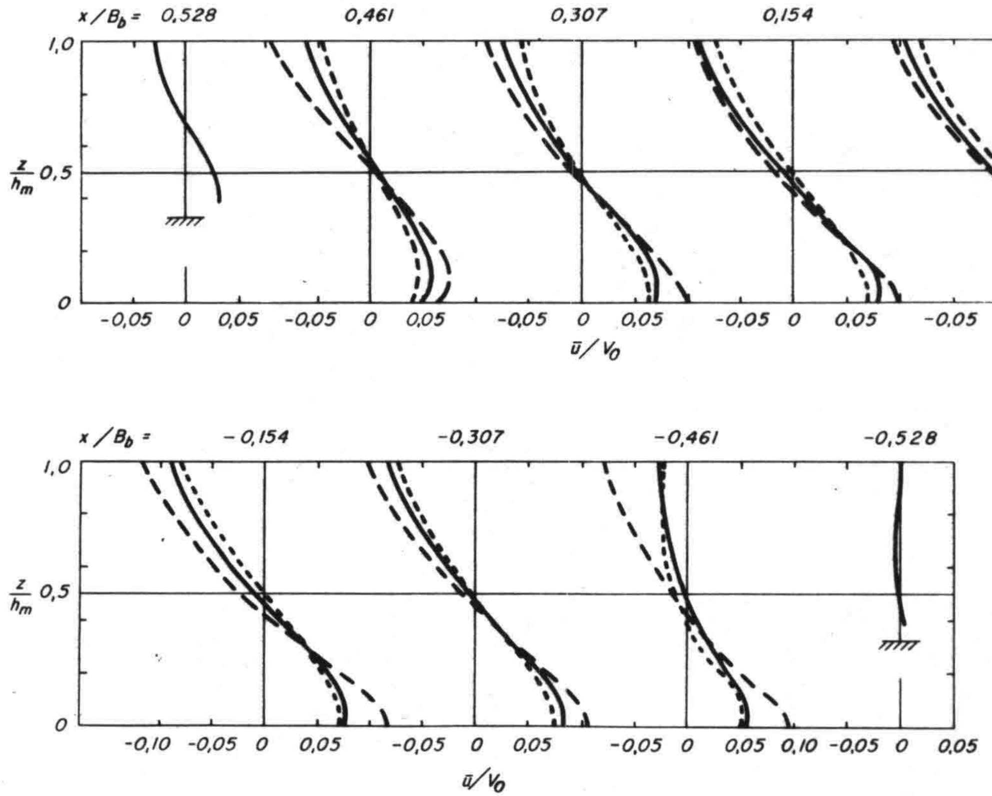

Fig. 17.(b) Section S1

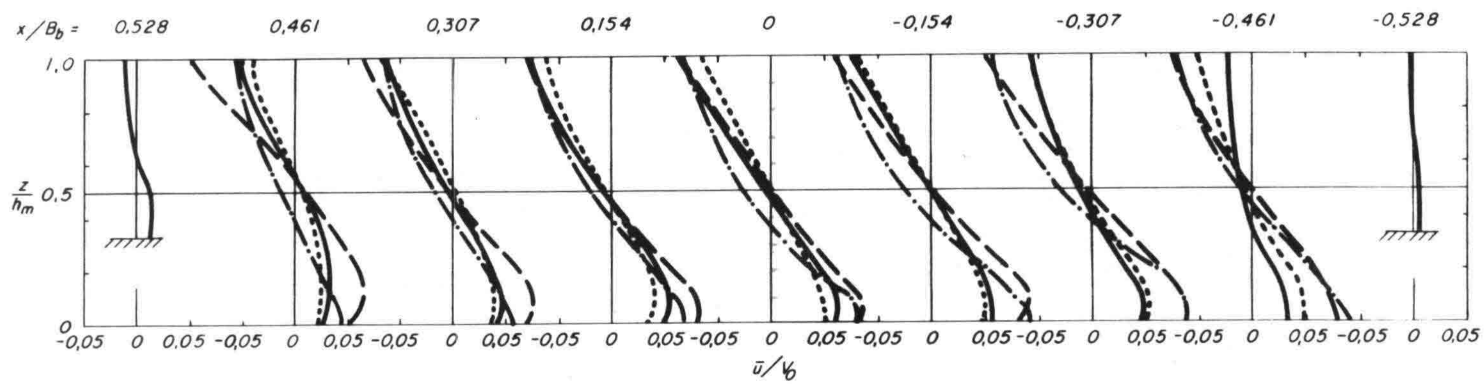

Fig, 17 (c) Section S2

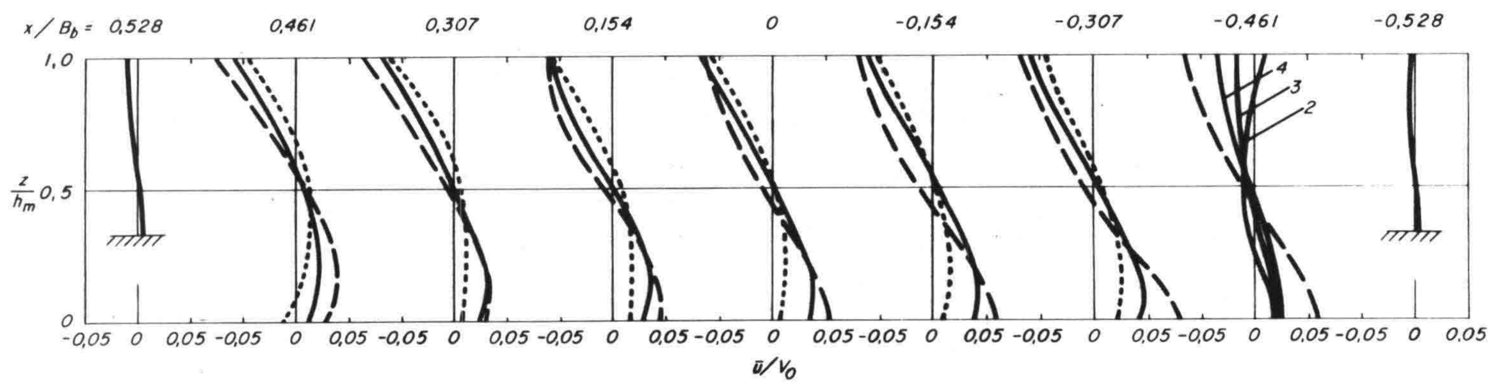

Fig, 17 (d) Section S3

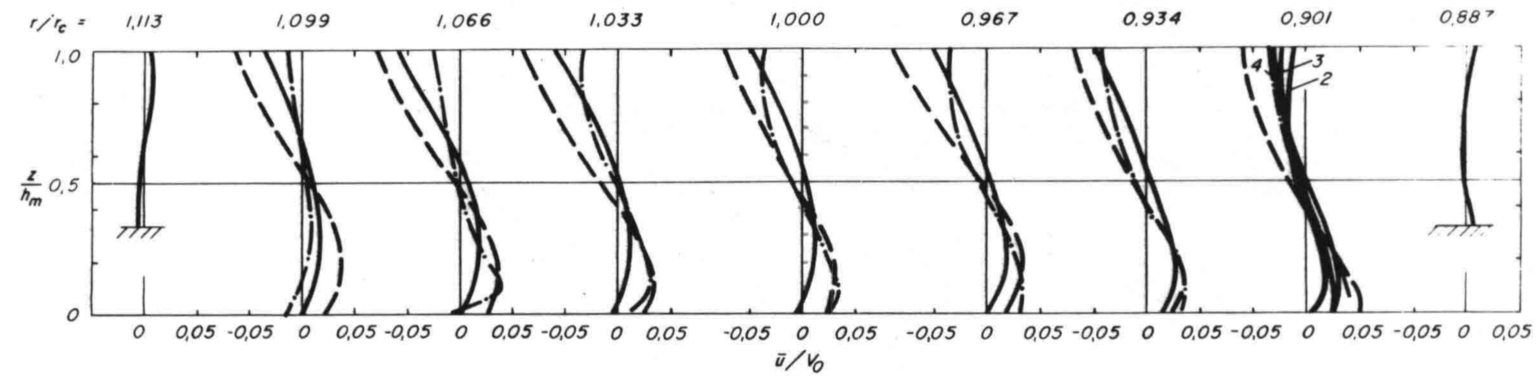

Fig, 17 (e) Section CIIO

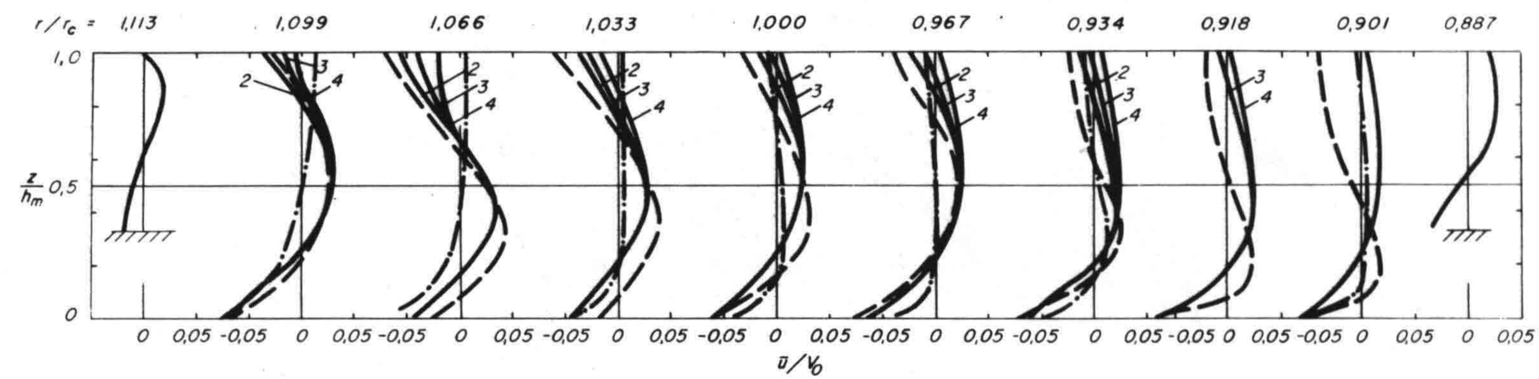

Fig, 17 (f) Section π/16

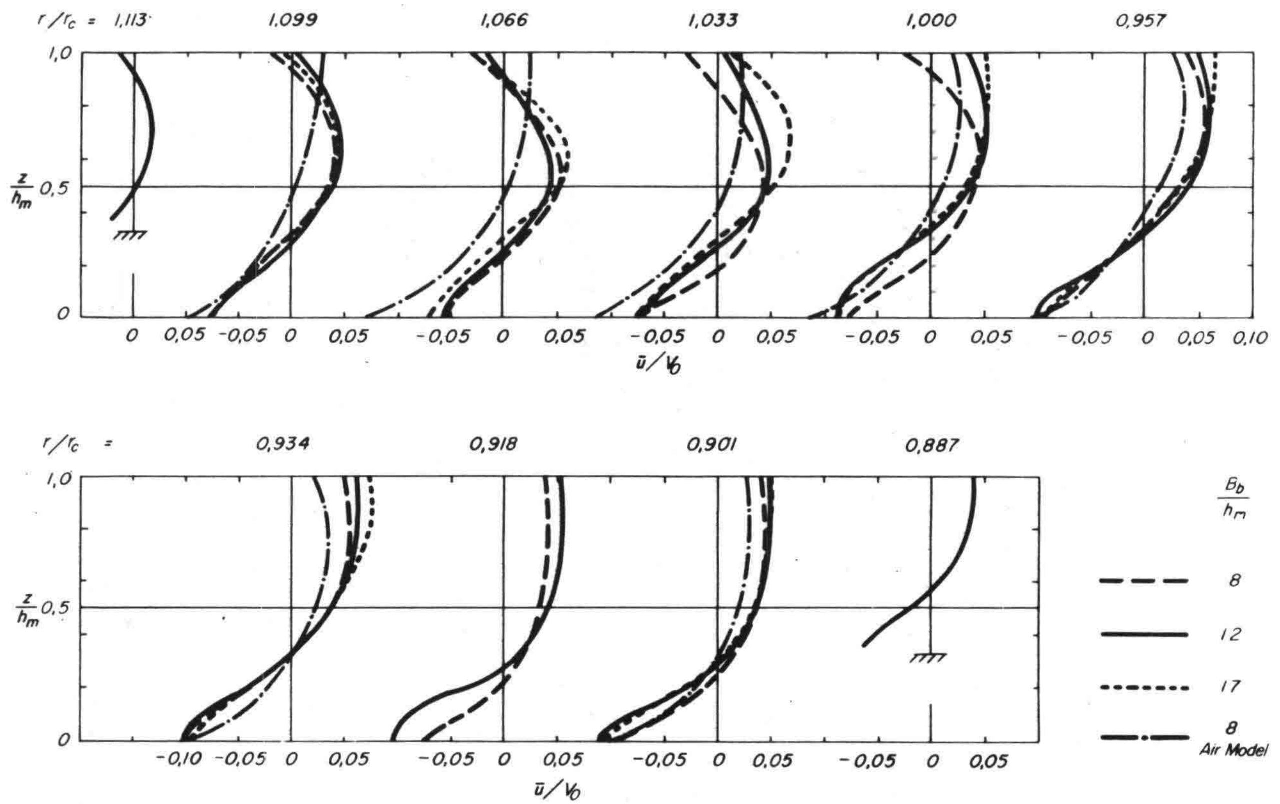

Fig. 17 (g) Section $\pi/8$

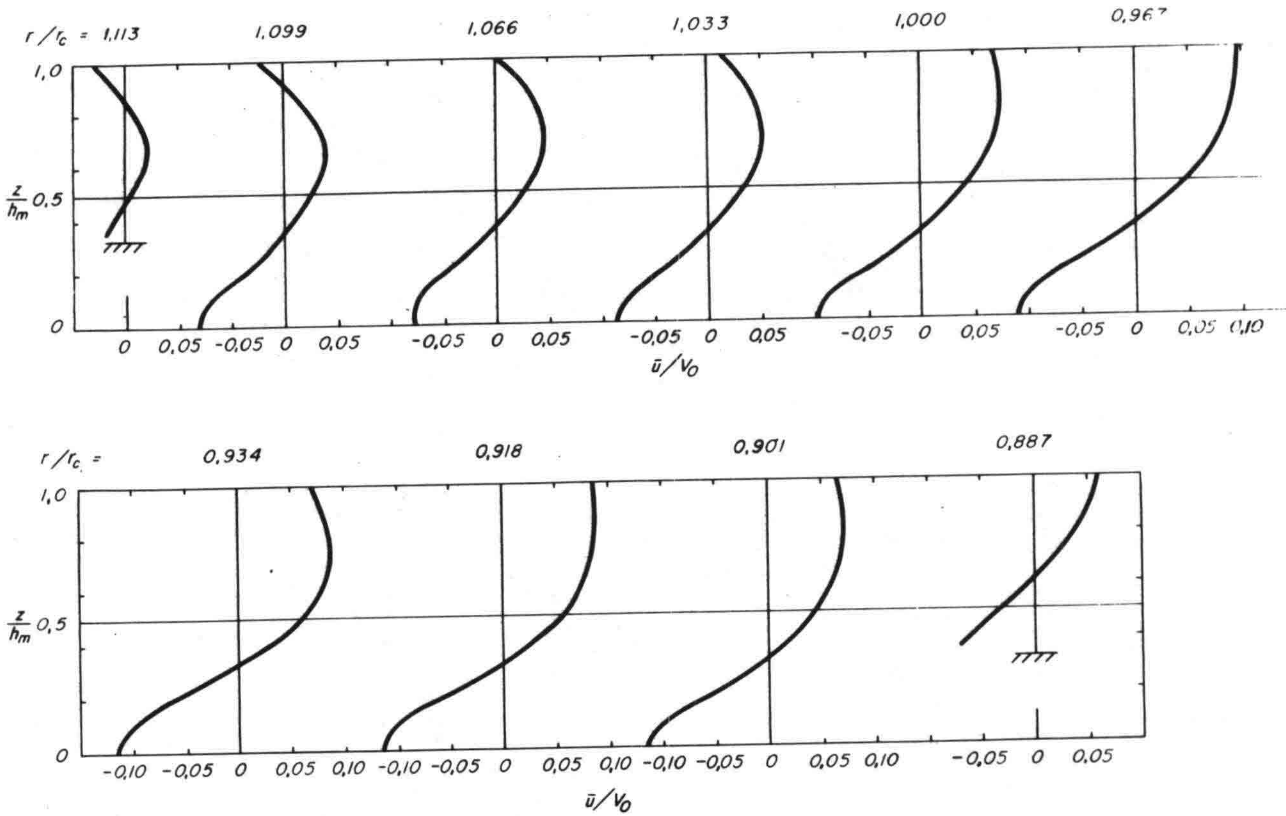

Fig. 17 (h) · Section $3\pi/16$

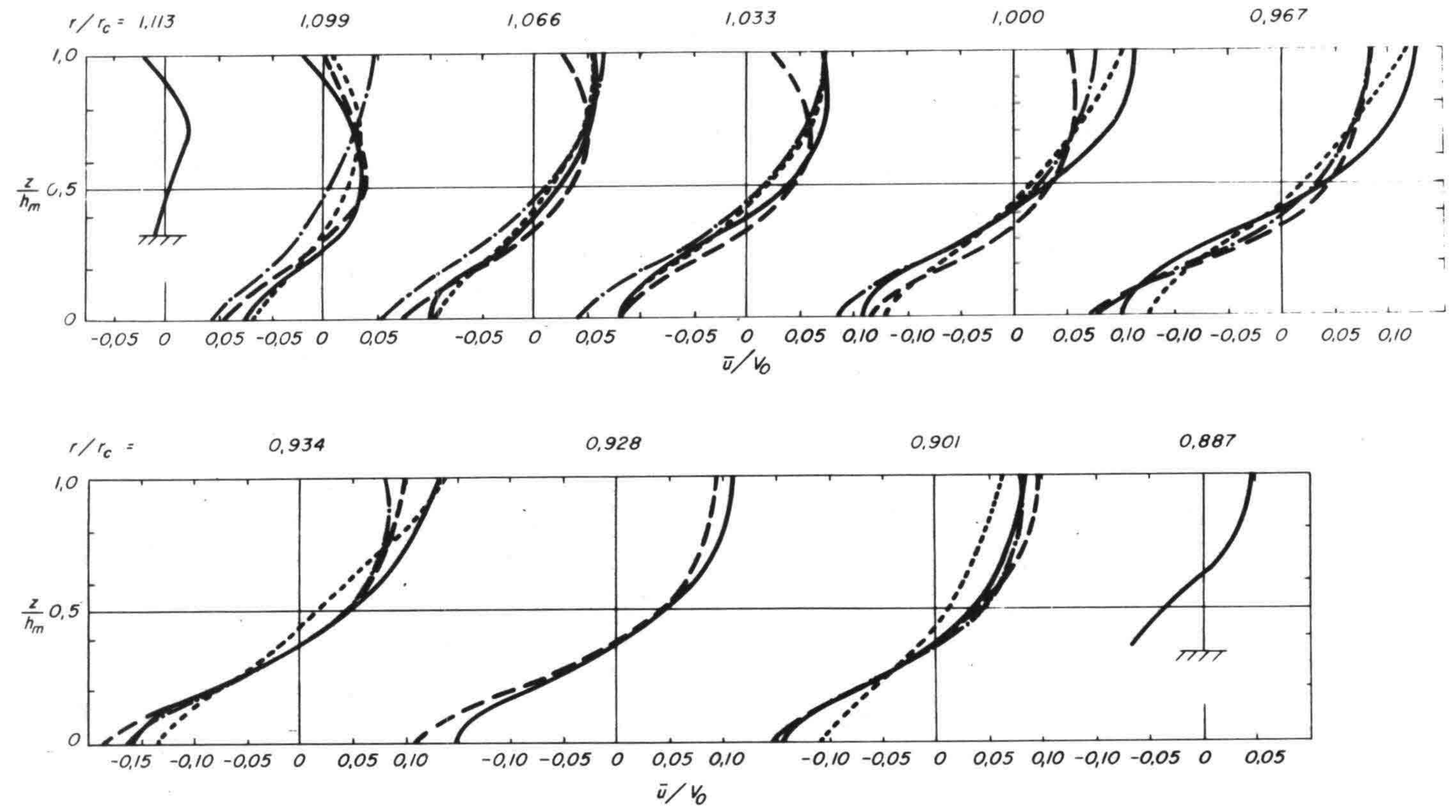

Fig. 17 (i) Section π/4

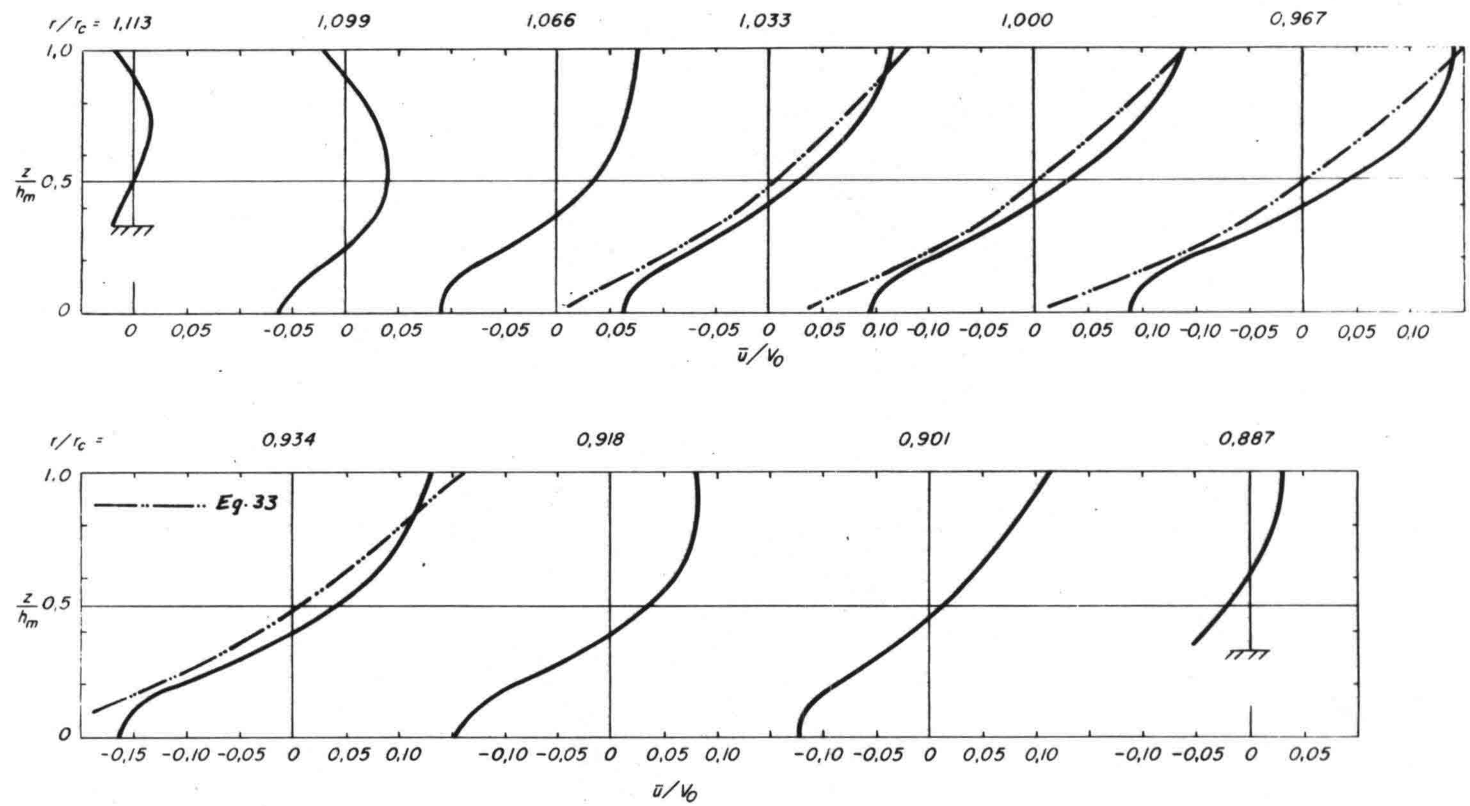

Fig. 17(j) Section $5\pi/16$

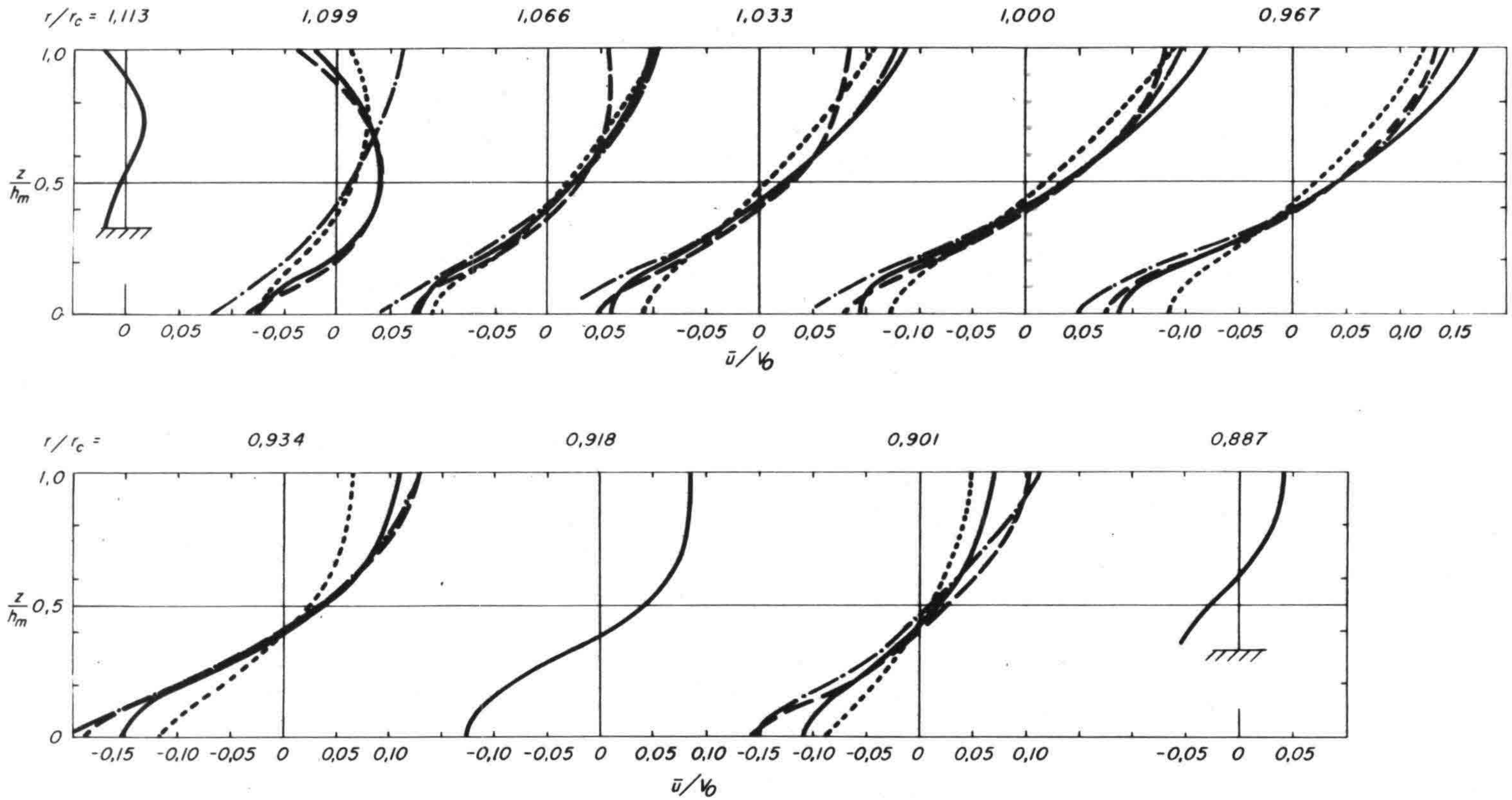

Fig. 17 (k) Section $3\pi/8$

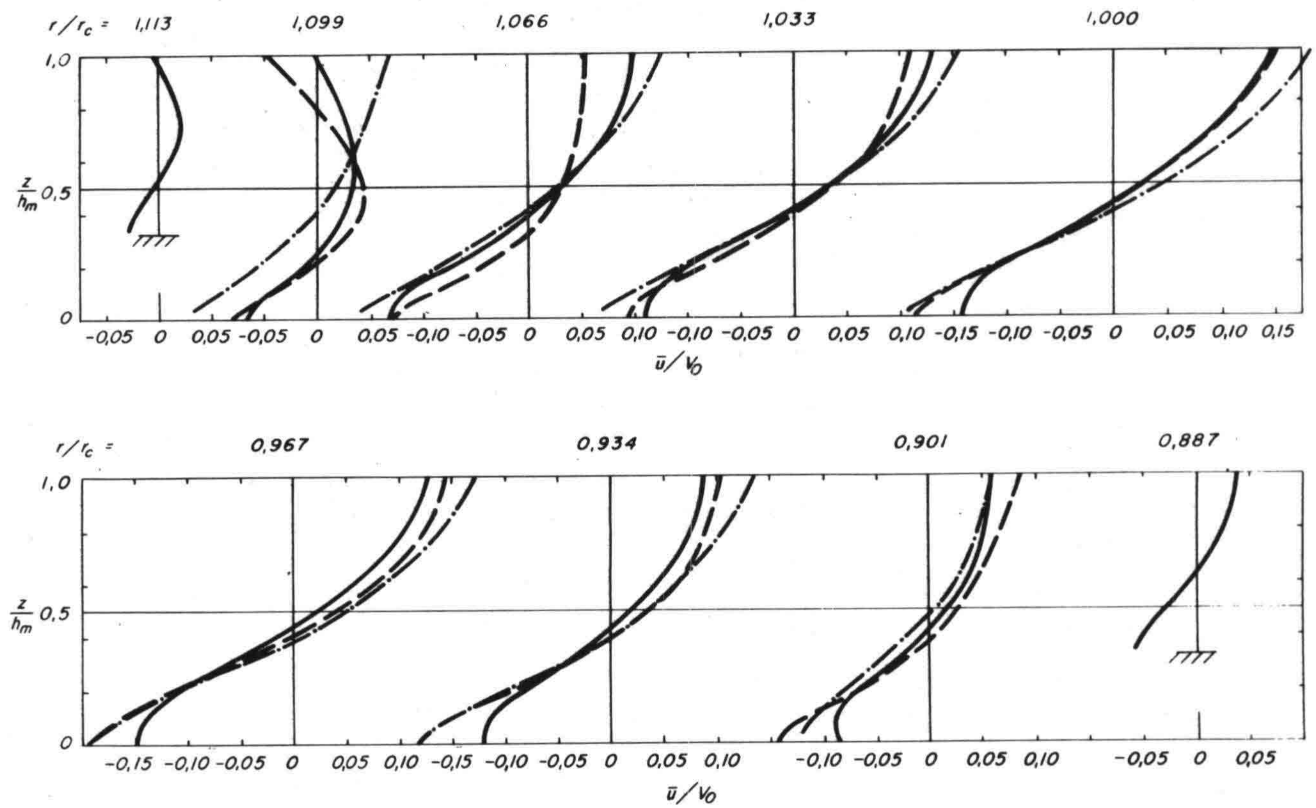

Fig. 17 (l) Section $7\pi/16$

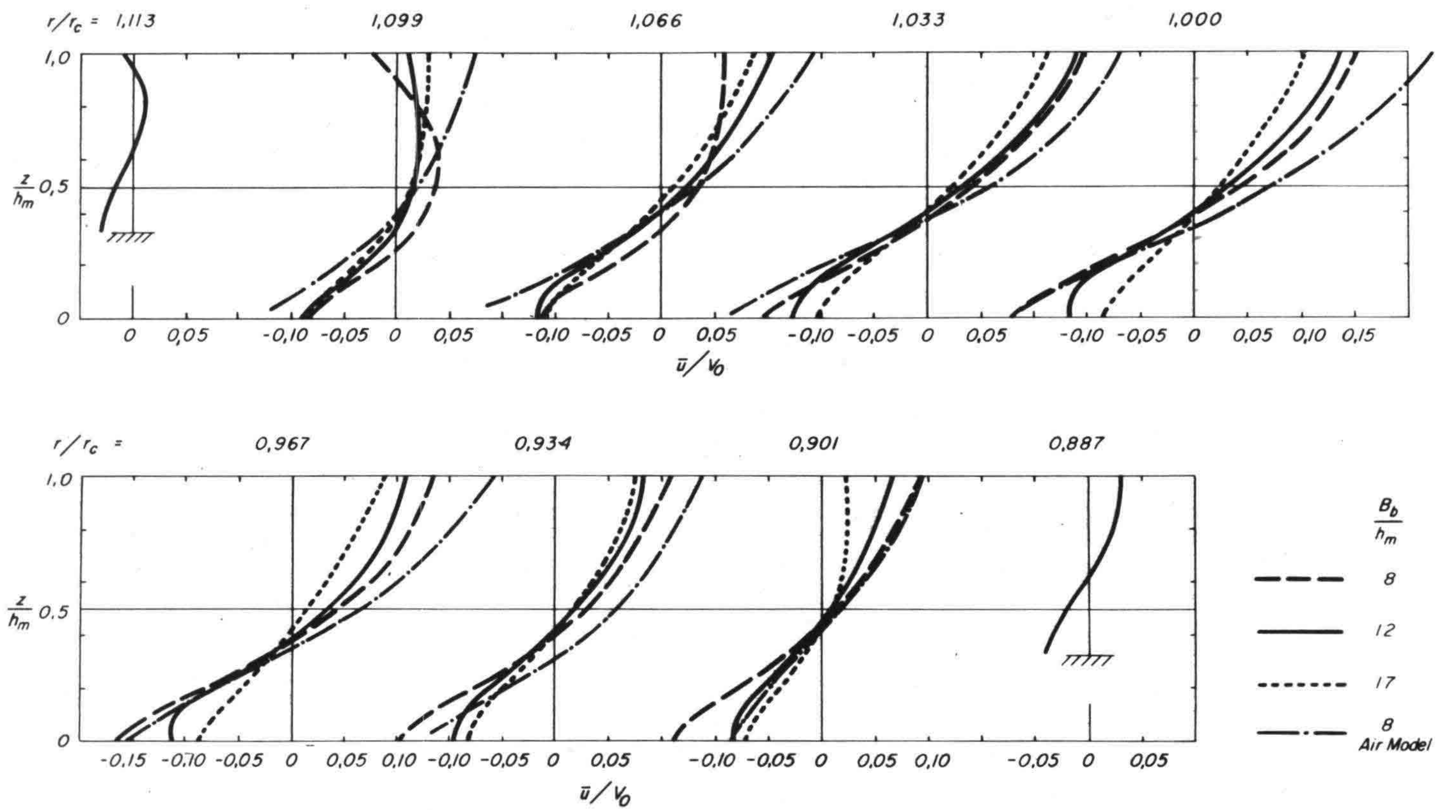

Fig. 17 (m) Section $\pi/2$

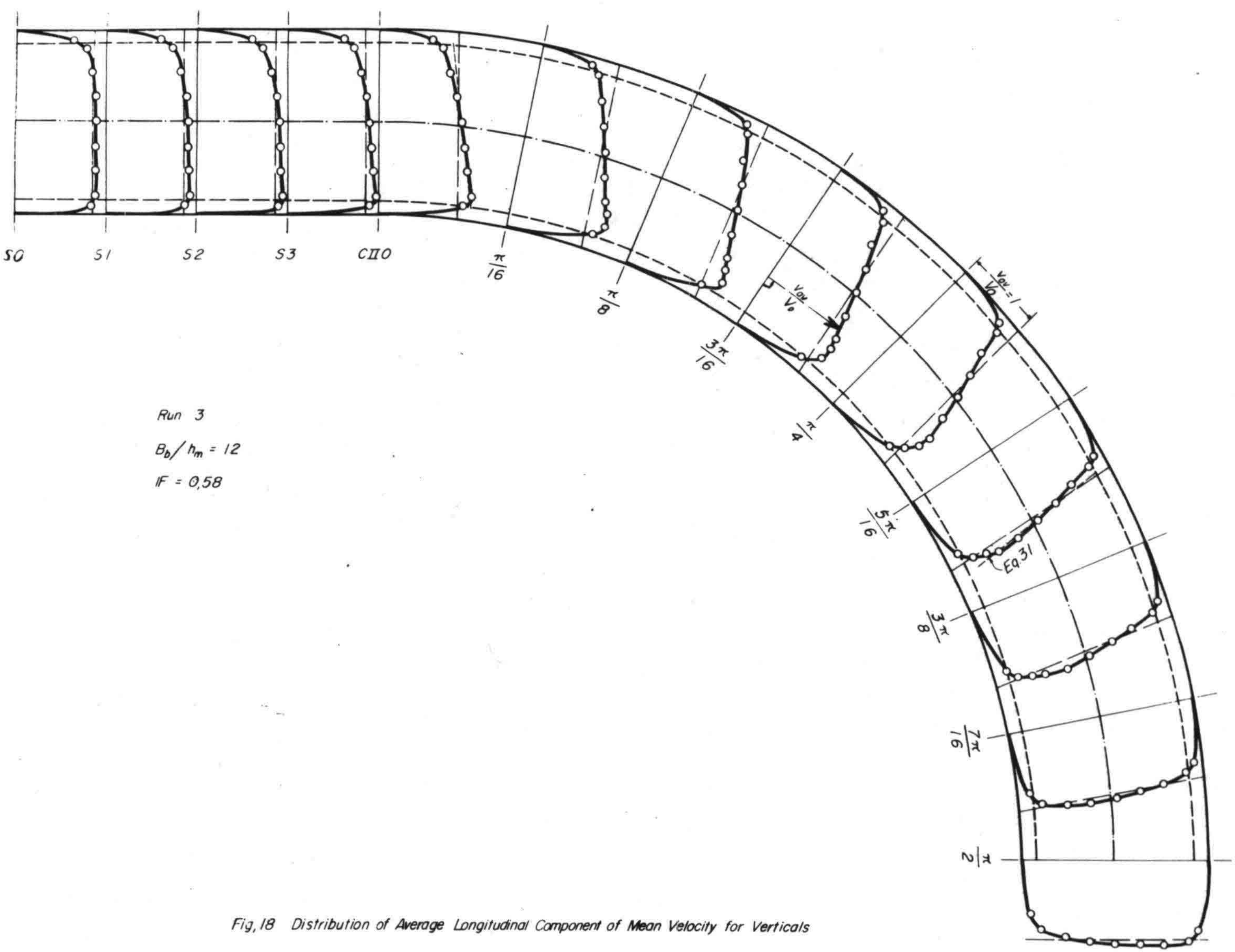

Fig, 18 Distribution of Average Longitudinal Component of Mean Velocity for Verticals

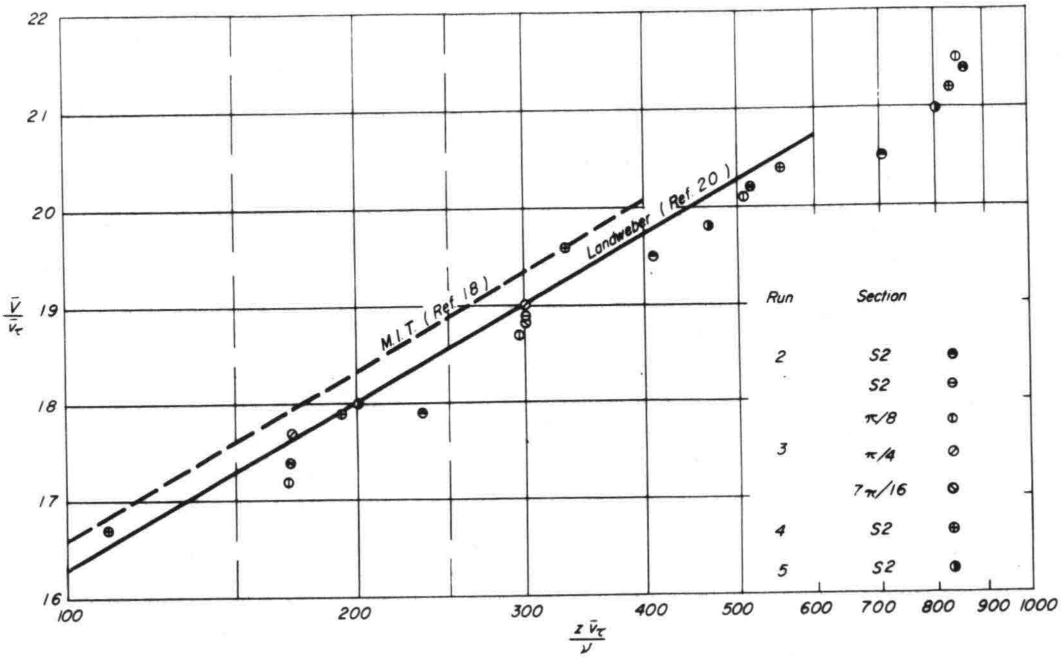

Fig. 19 Velocity Distribution near Channel Bed

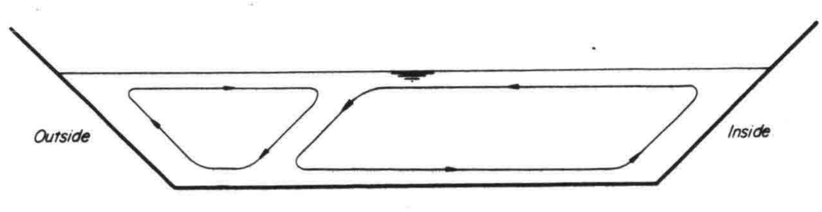

Fig. 20 Sketch of Spiral Motion in Upstream Part of Bend

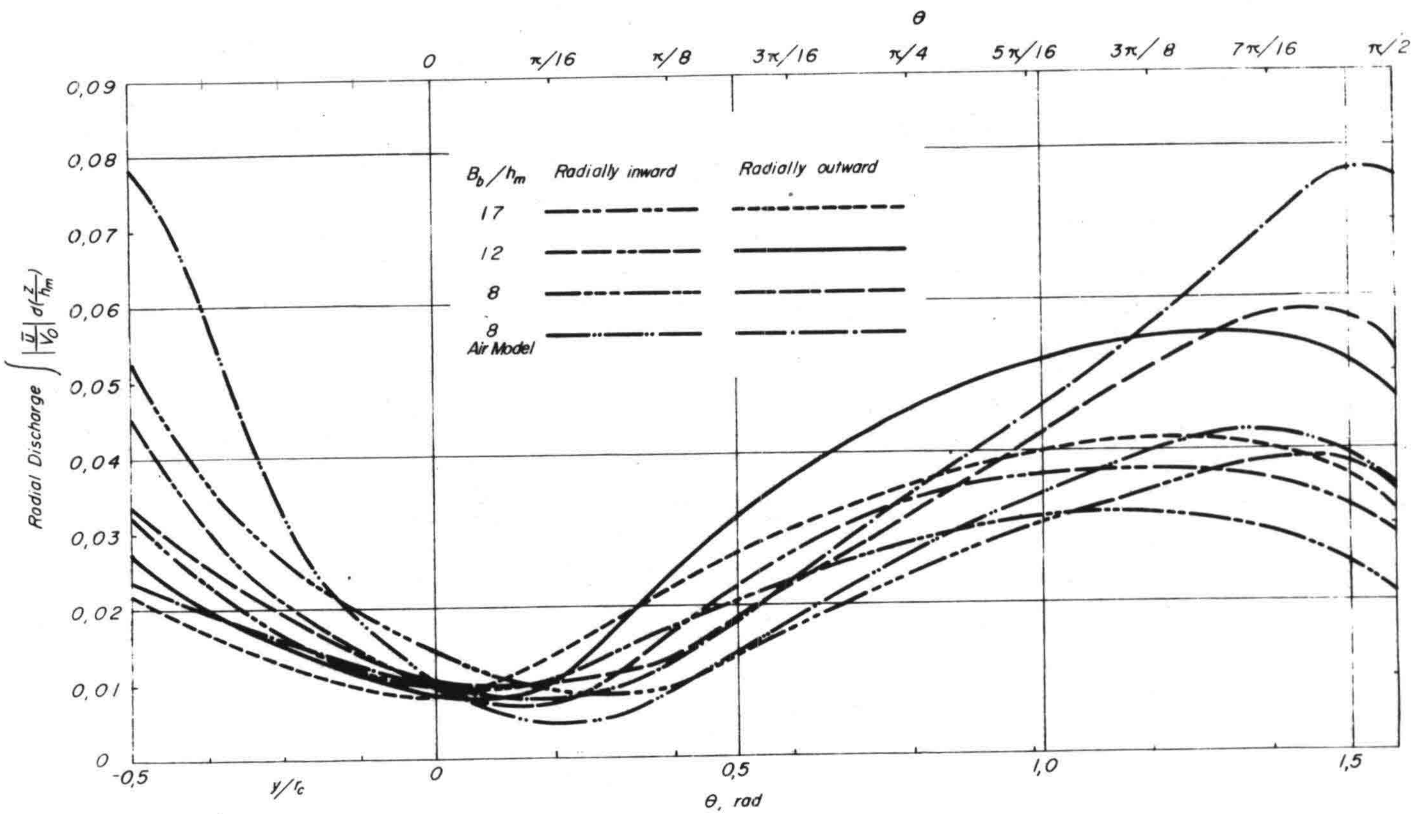

Fig. 21 Radially Inward and Outward Discharge per Unit Length through Axial Section of Channel

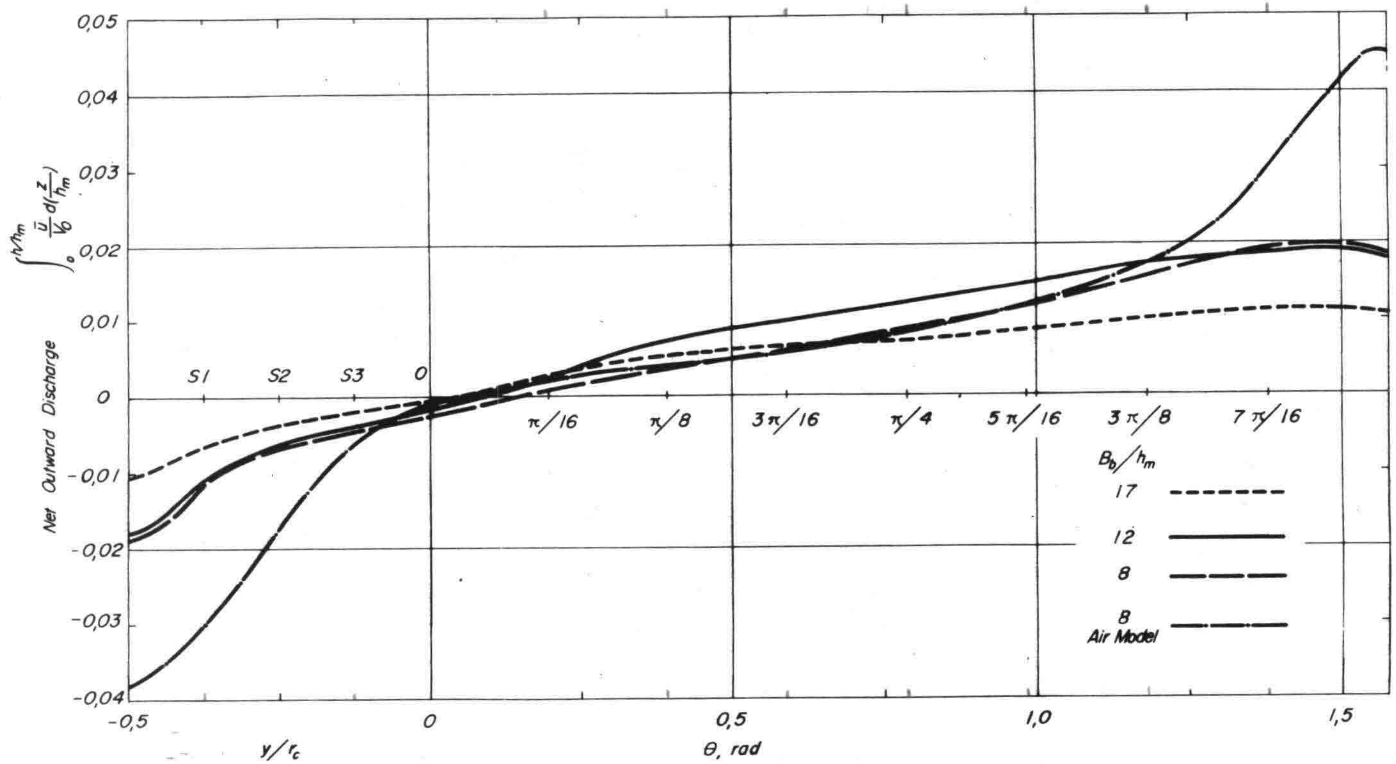

Fig. 22 Net Radial Discharge per Unit Length through Axial Section of Channel

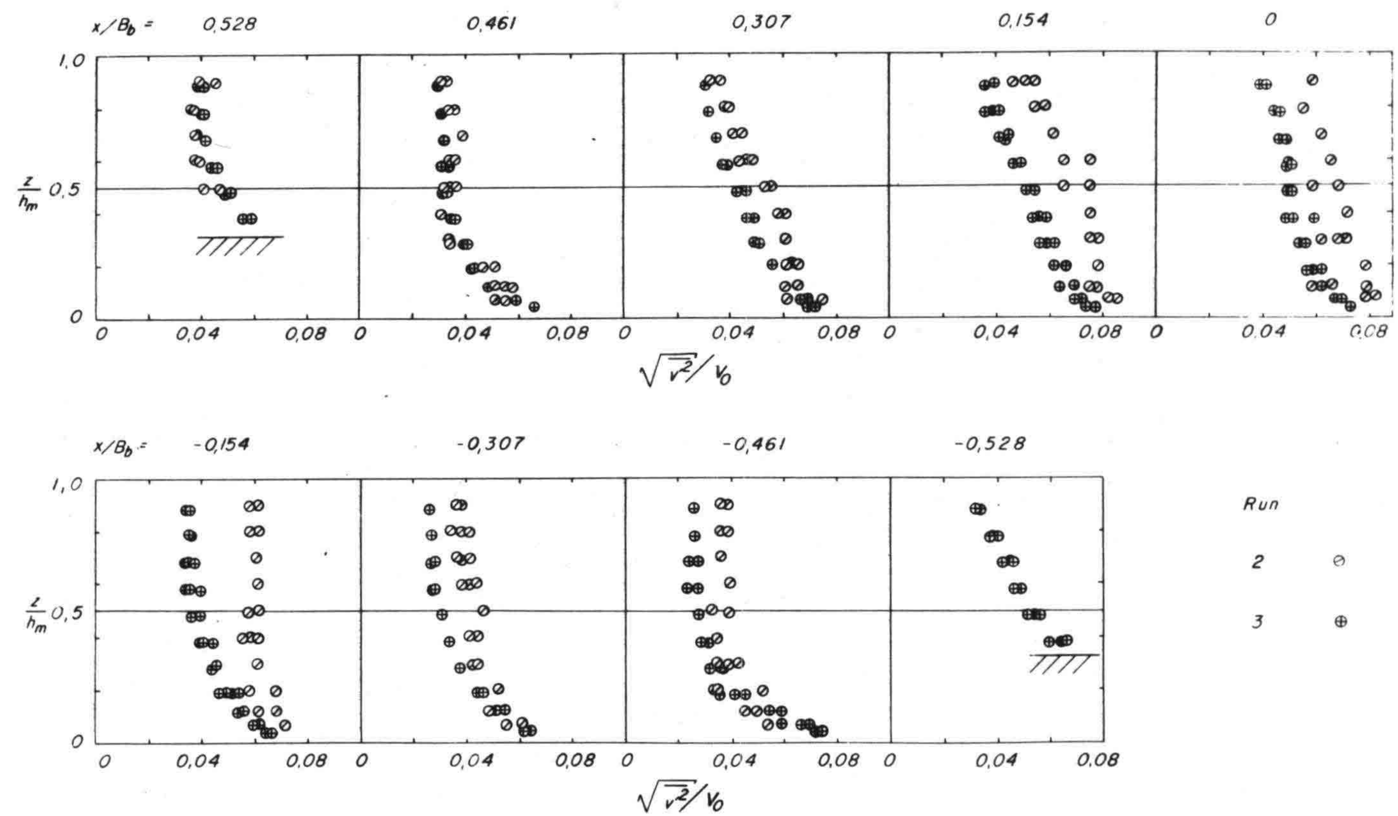

Fig, 23 Distribution of Longitudinal Component of Turbulence Intensity, (a) Section SO

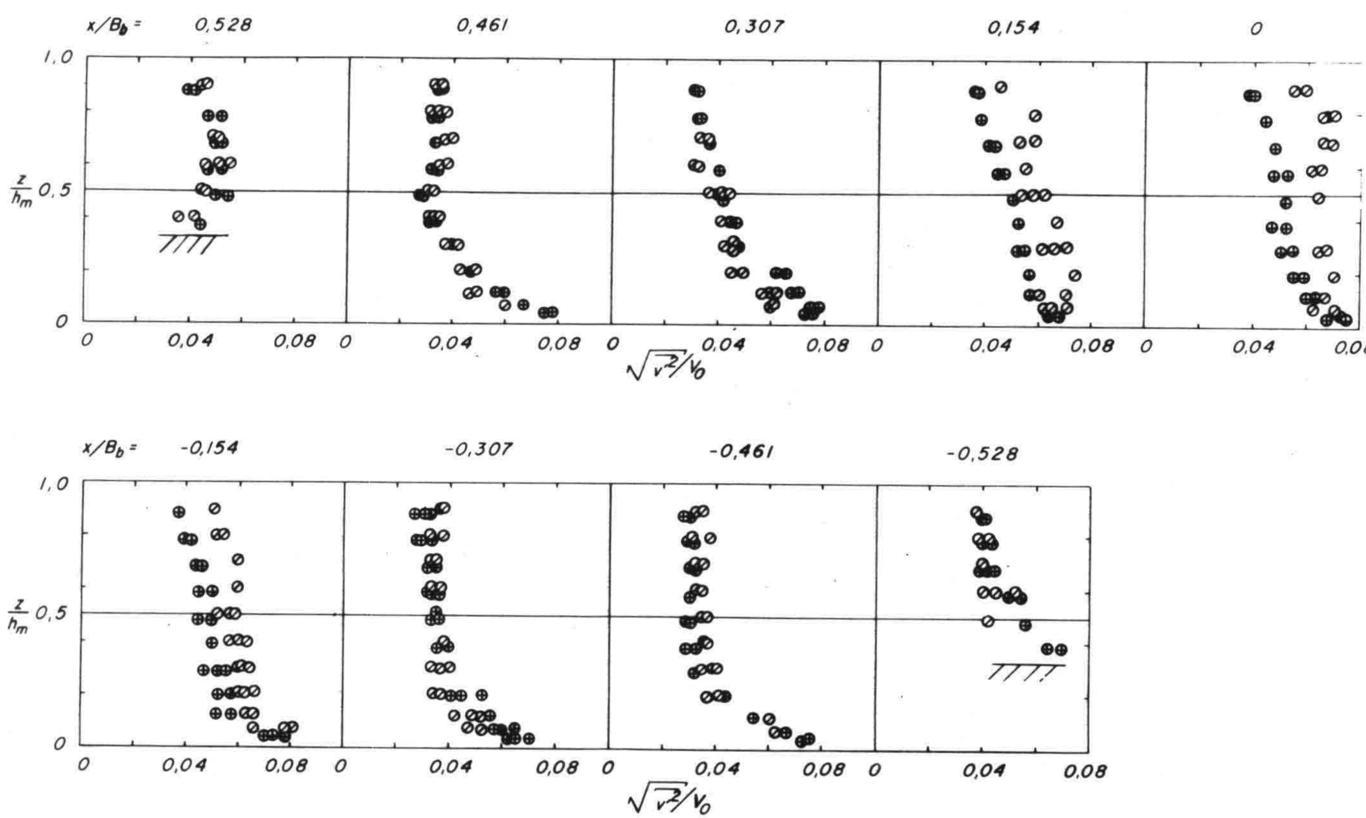

Fig, 23 (b) Section SI

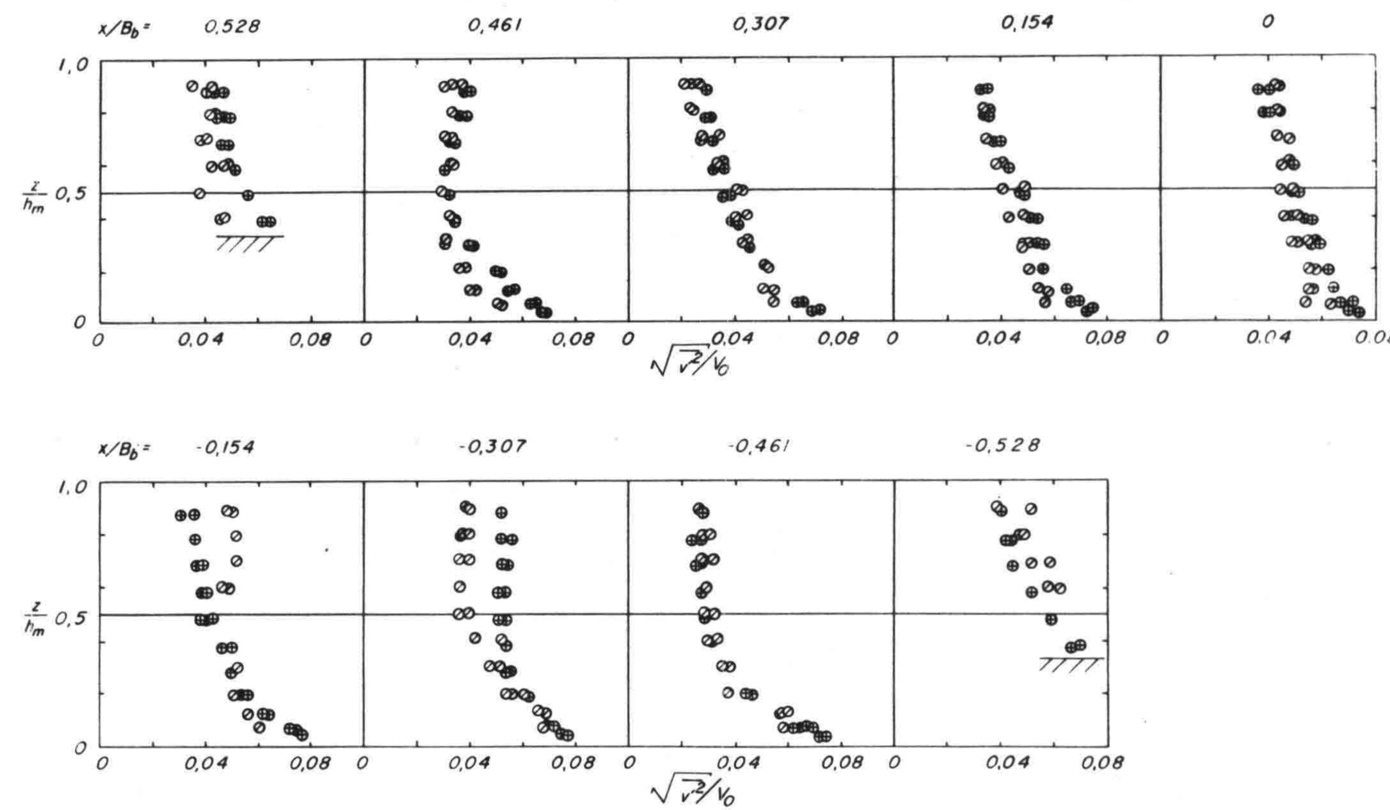

Fig, 23 (c) Section S2

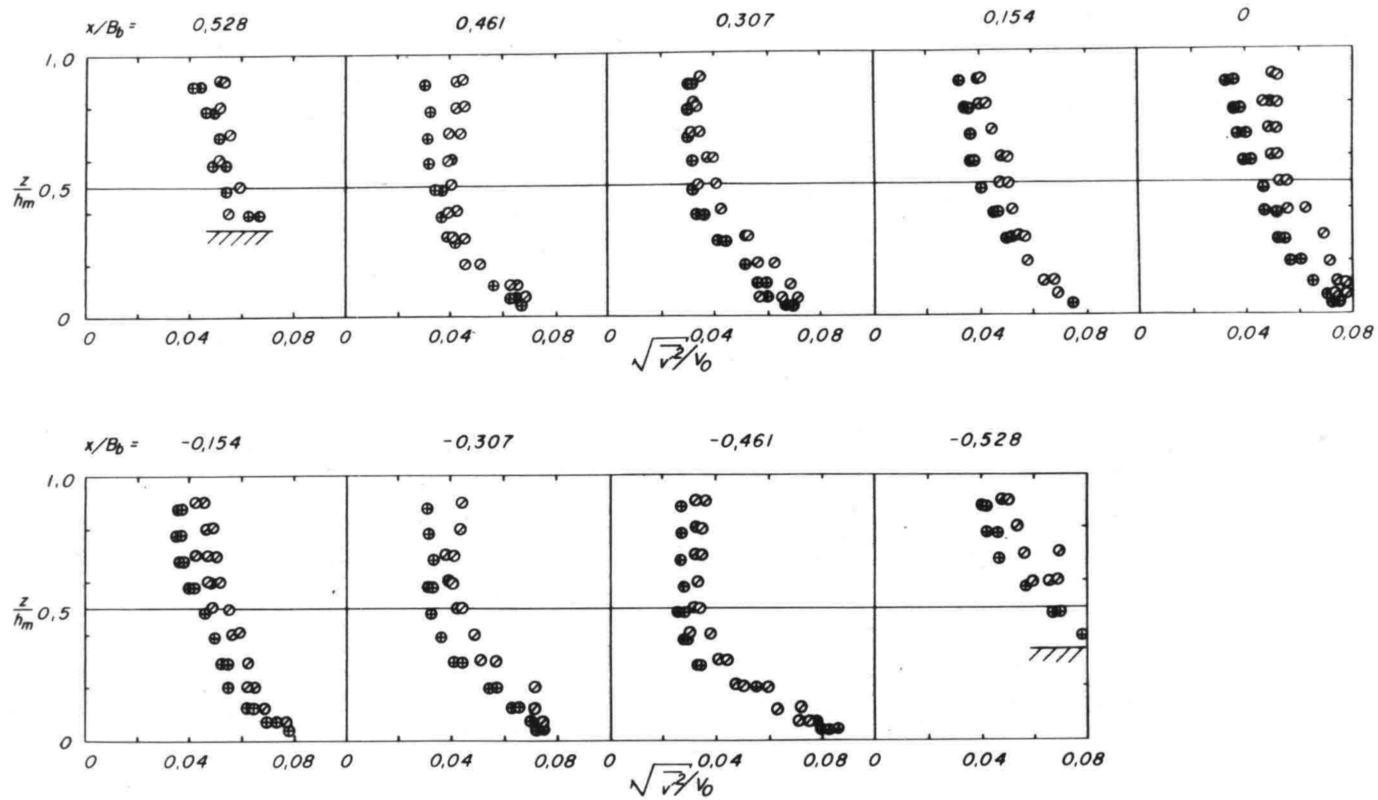

Fig. 23(d) Section S3

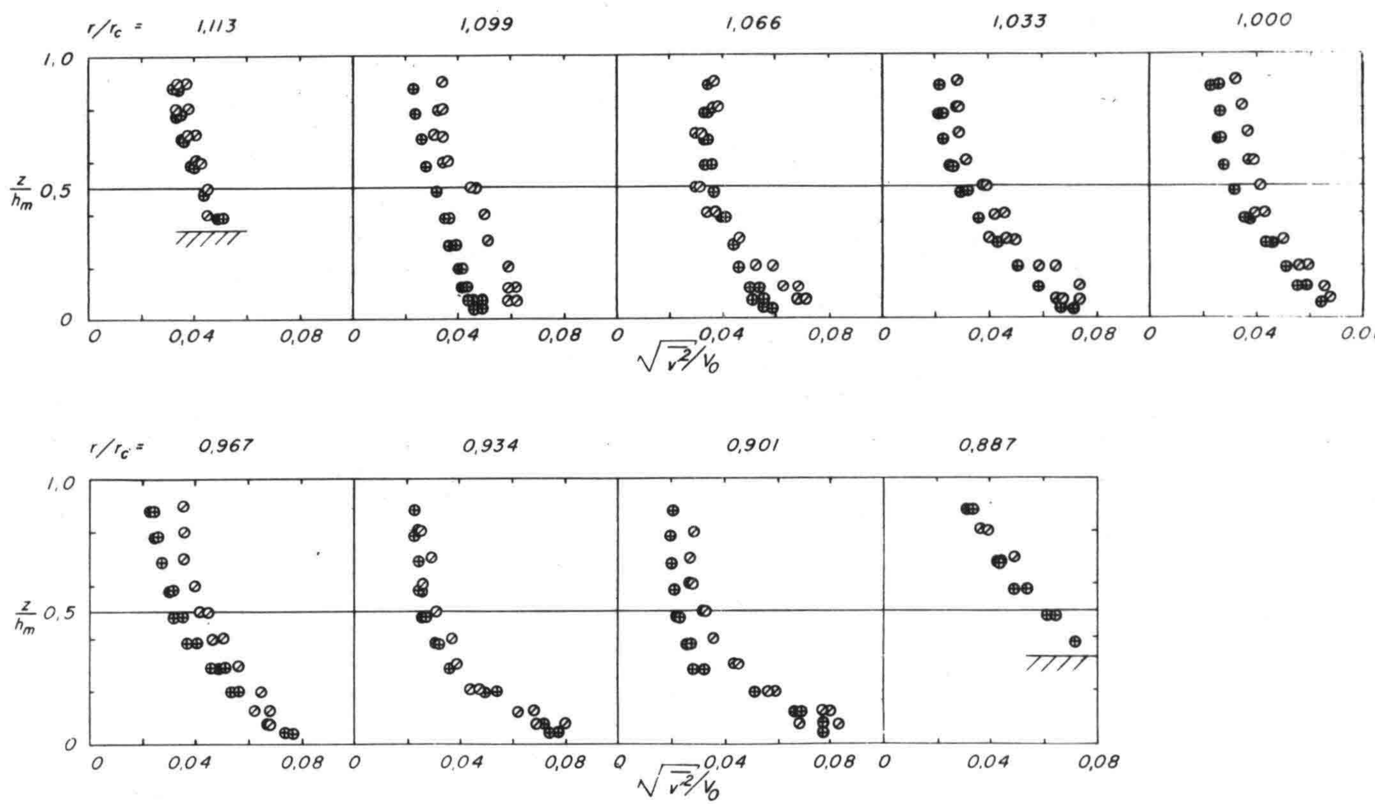

Fig, 23 (e) Section CIIO

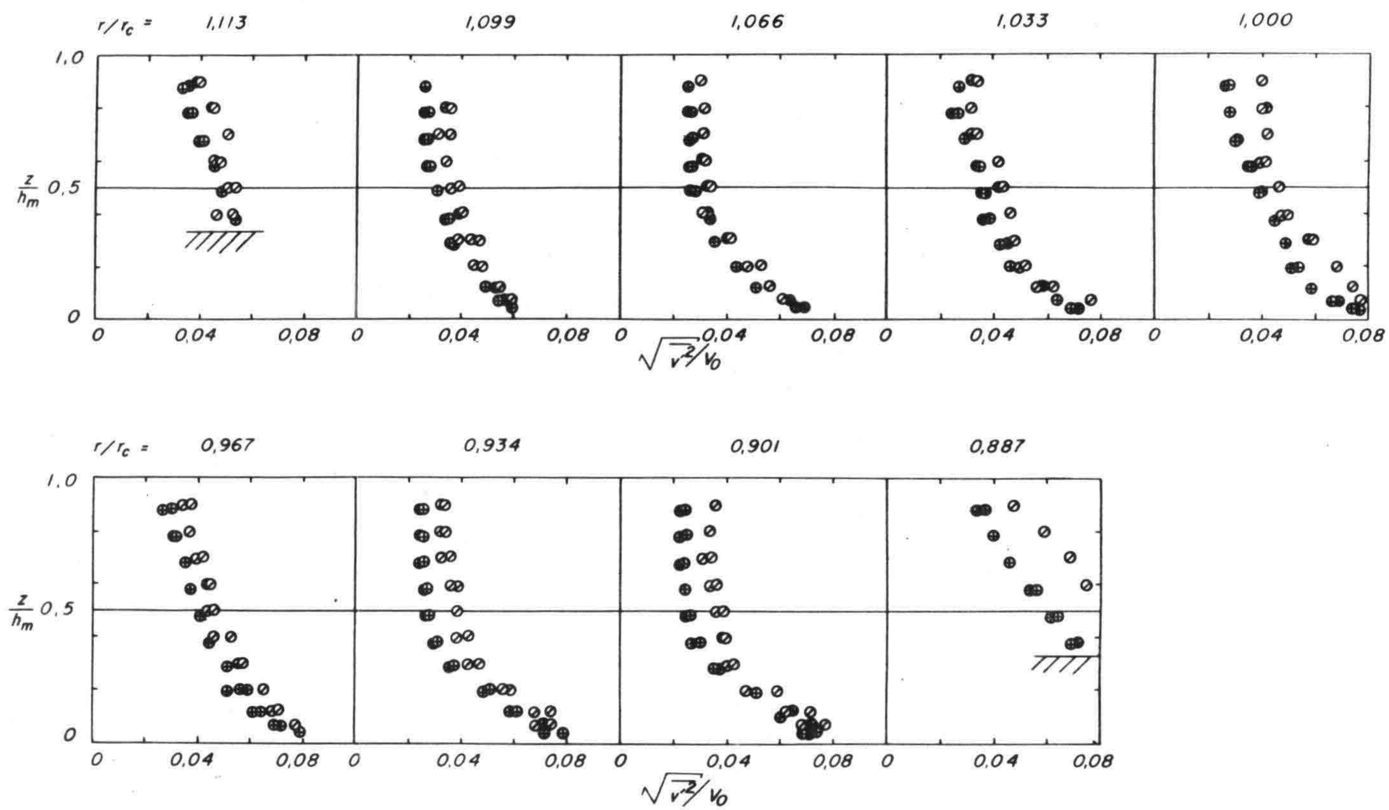

Fig, 23 (f) Section $\pi/16$

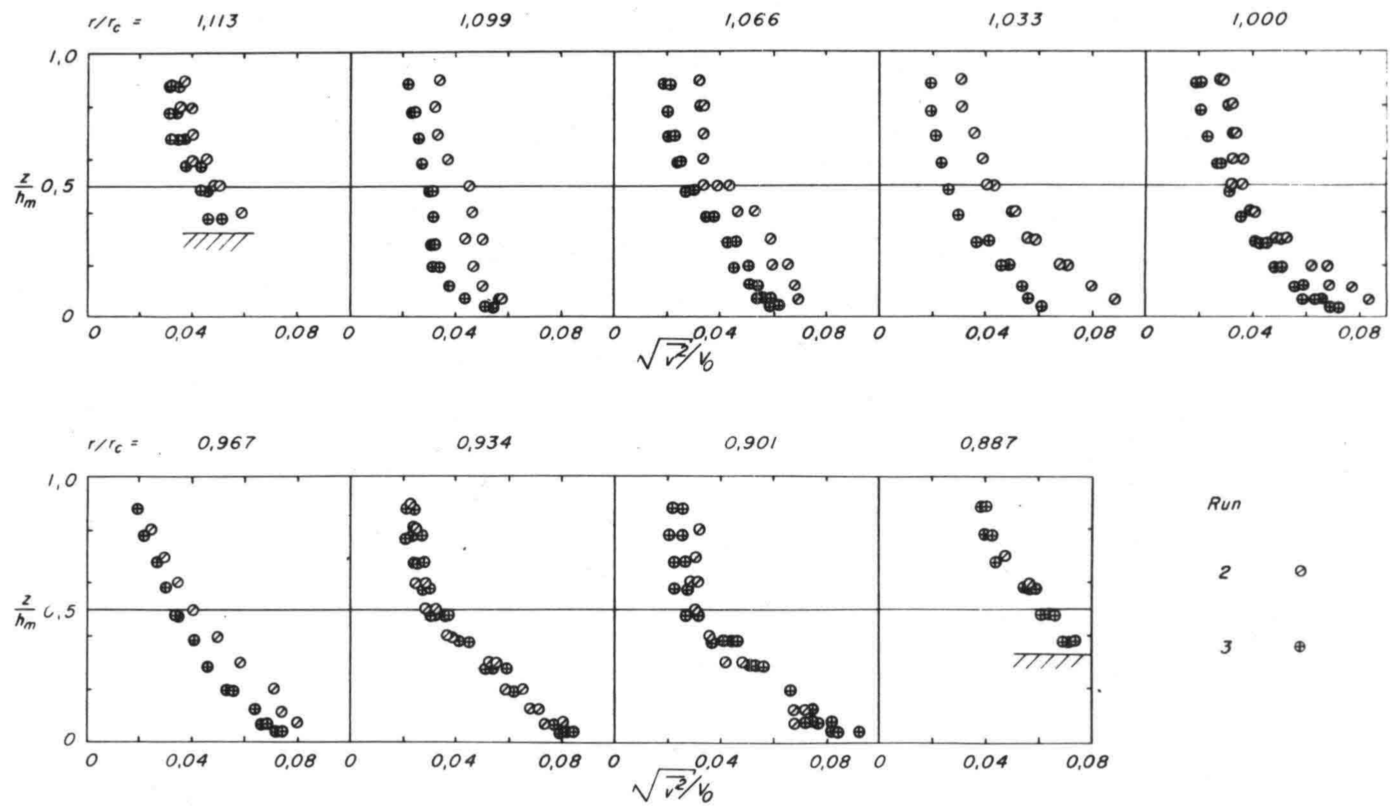

Fig, 23 (g) Section $\pi/8$

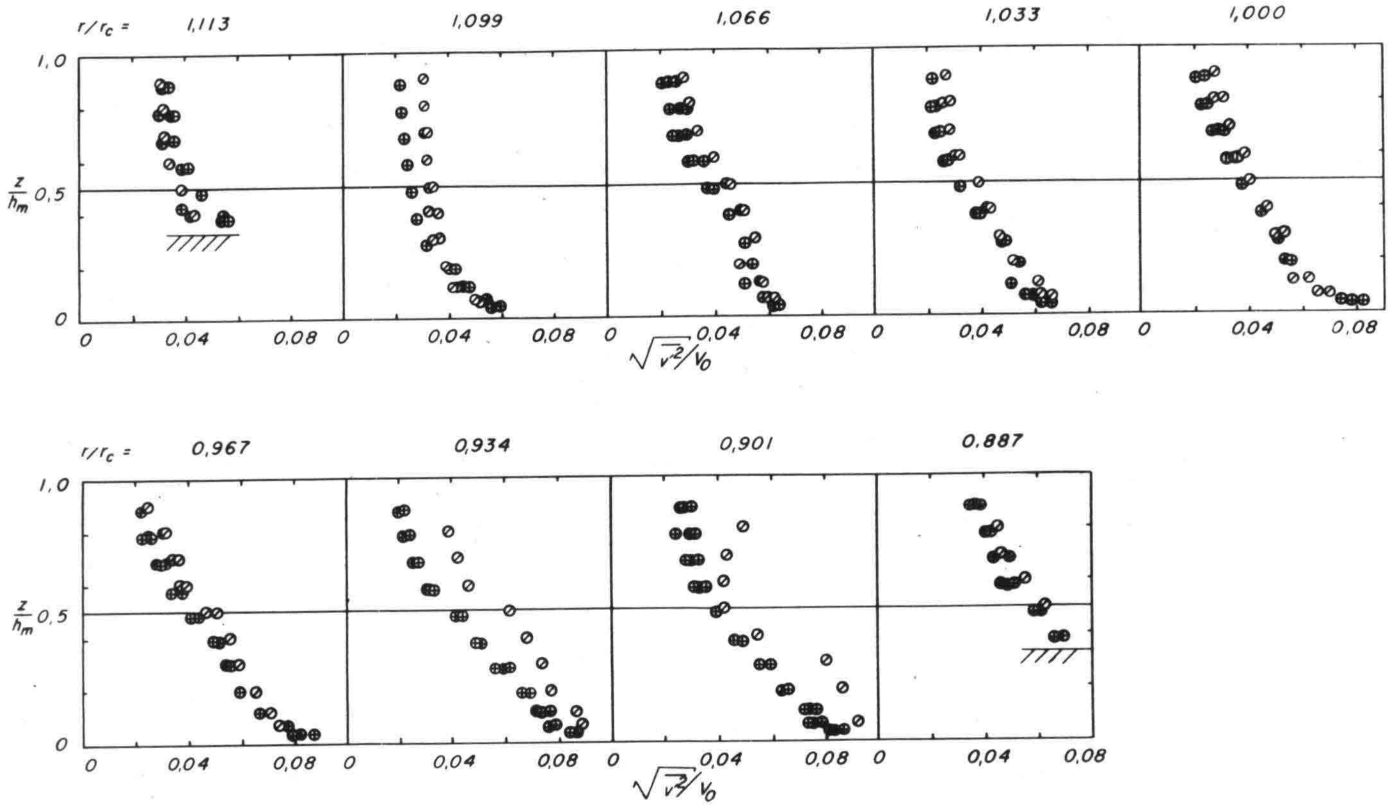

Fig, 23 (h) Section 3π/16

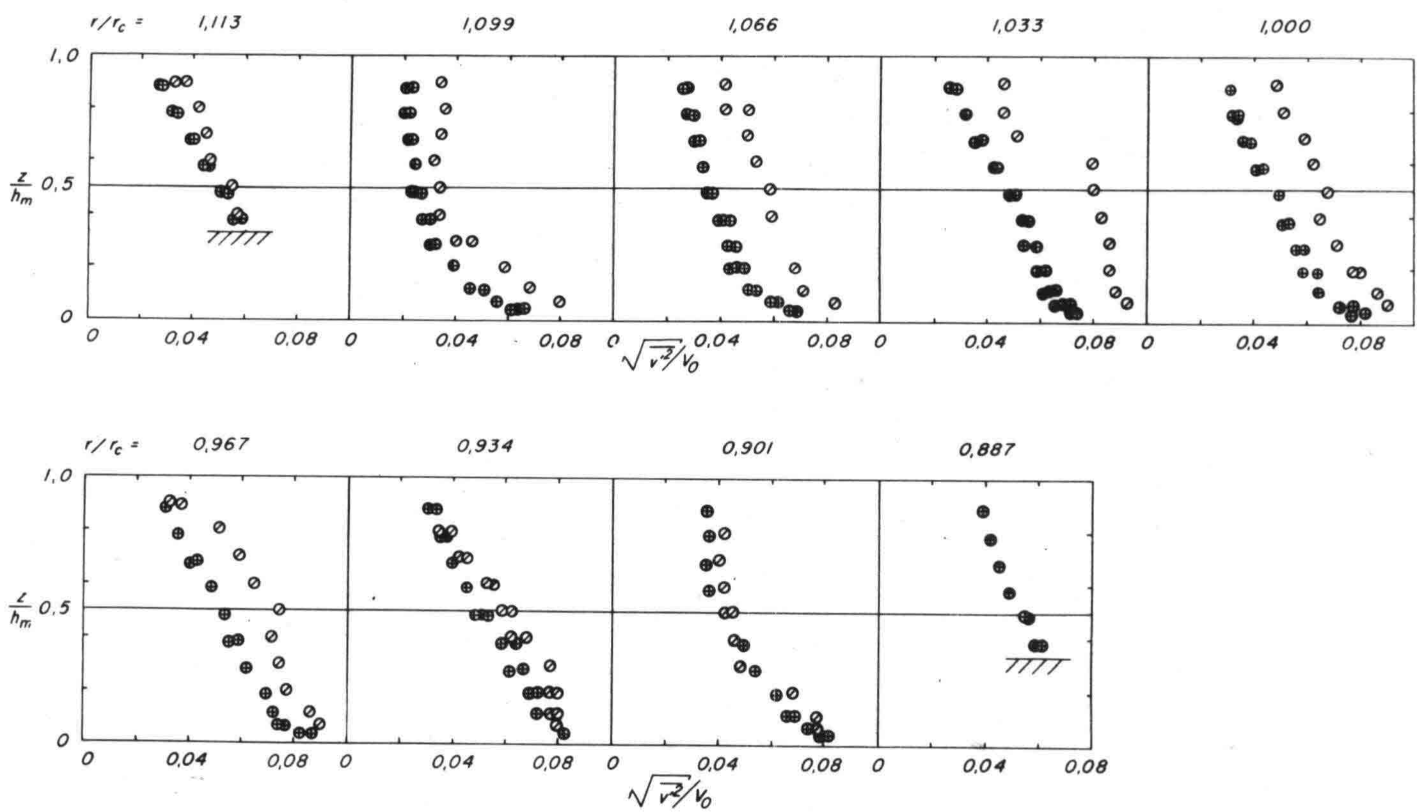

Fig, 23 (j) Section $5\pi/16$

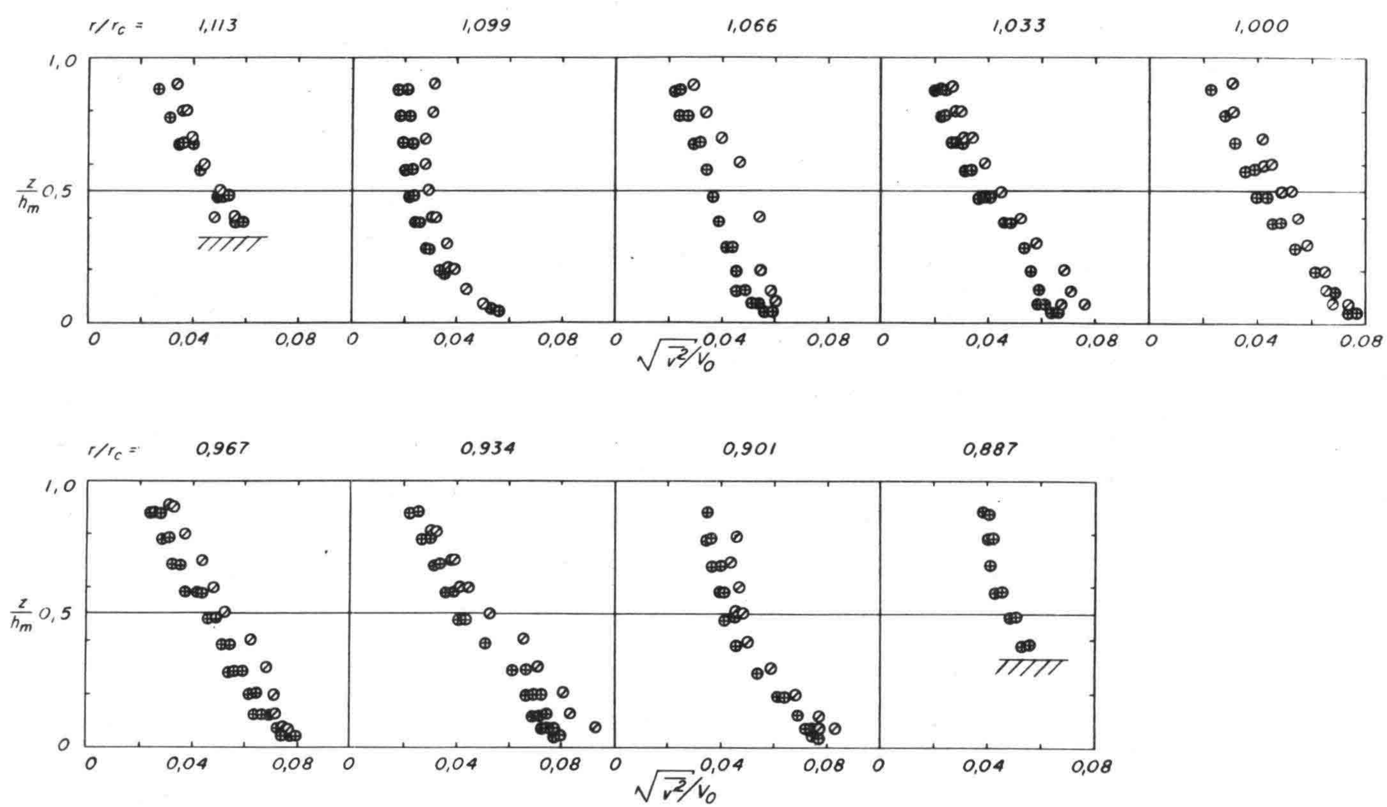

Fig. 23 (i) Section $\pi/4$

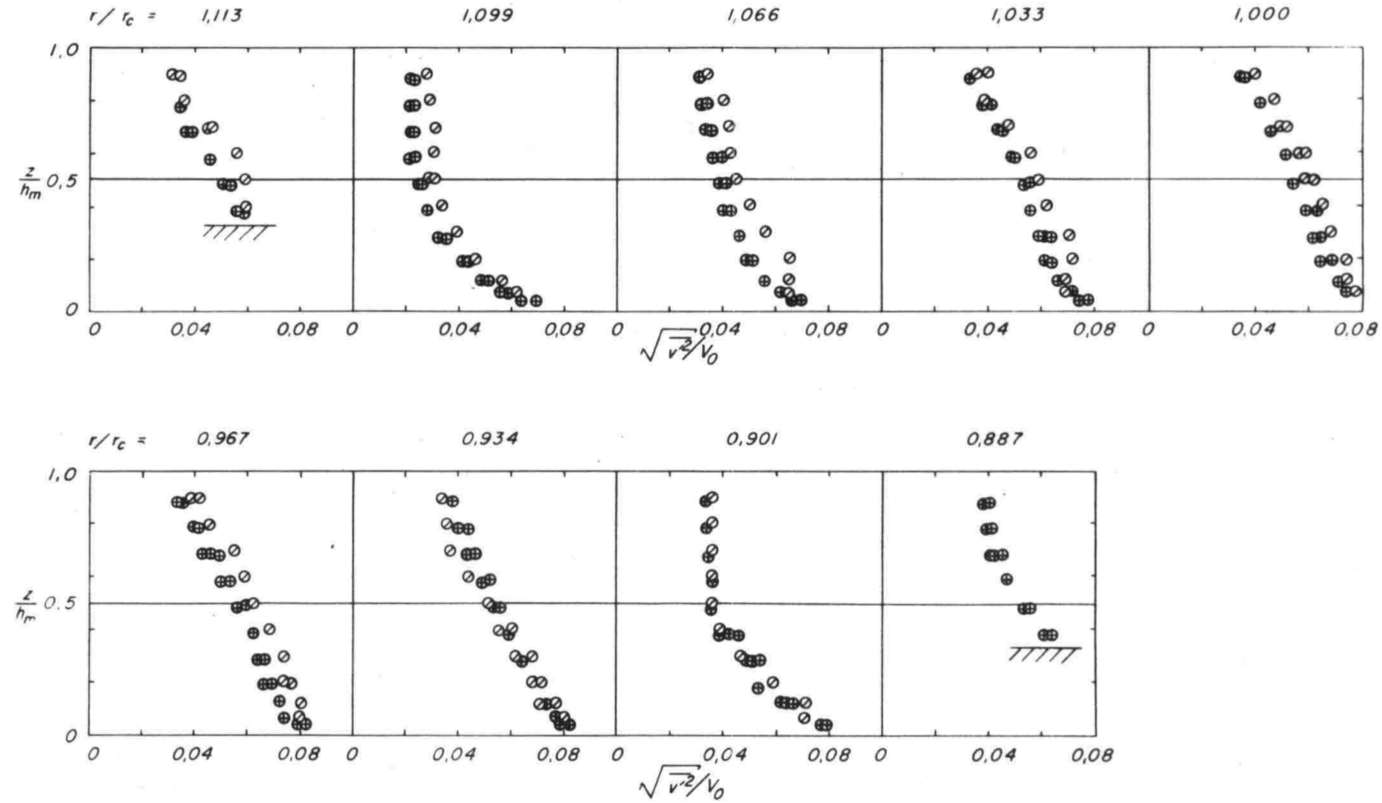

Fig, 23 (k) Section 3π/16

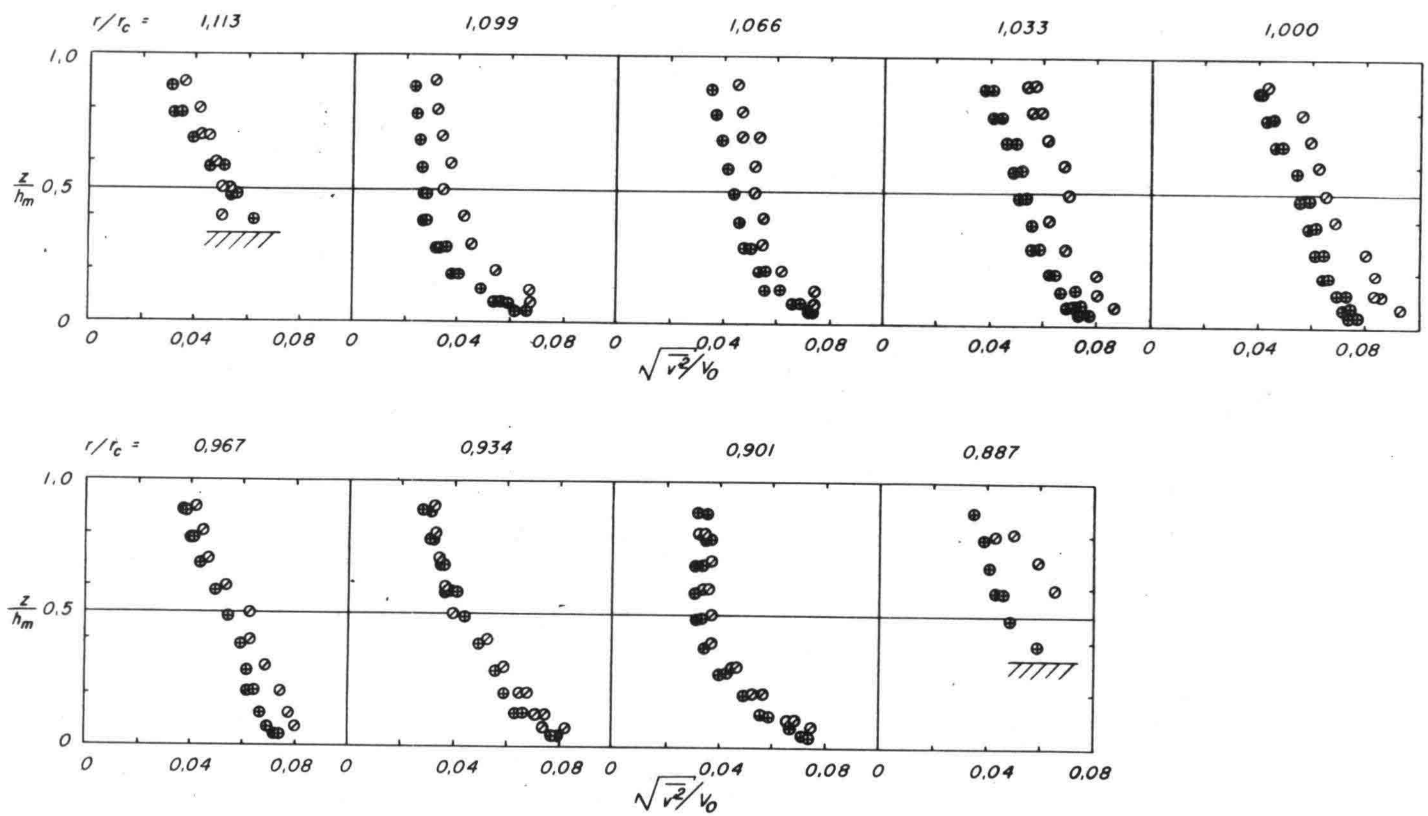

Fig. 23 (1) Section 7π/16

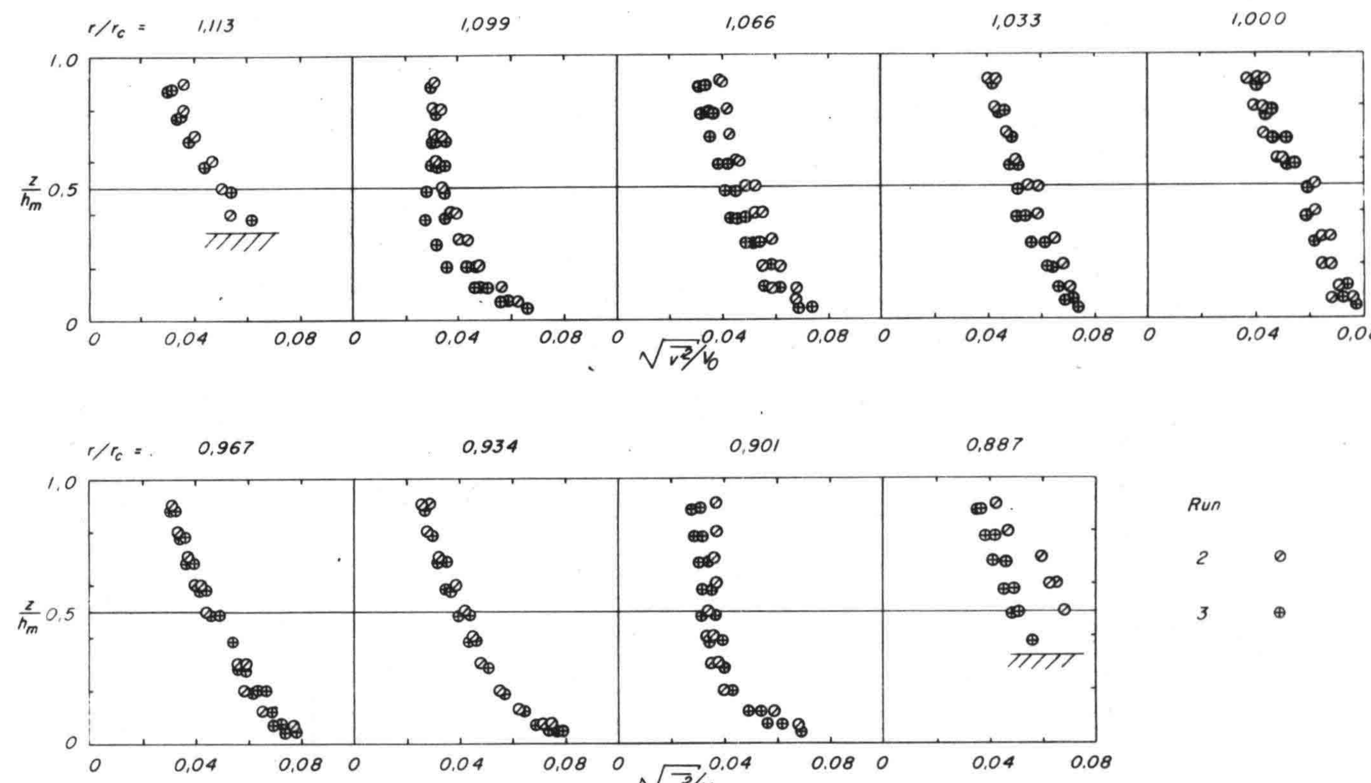

Fig, 23 (m) Section $\pi/2$

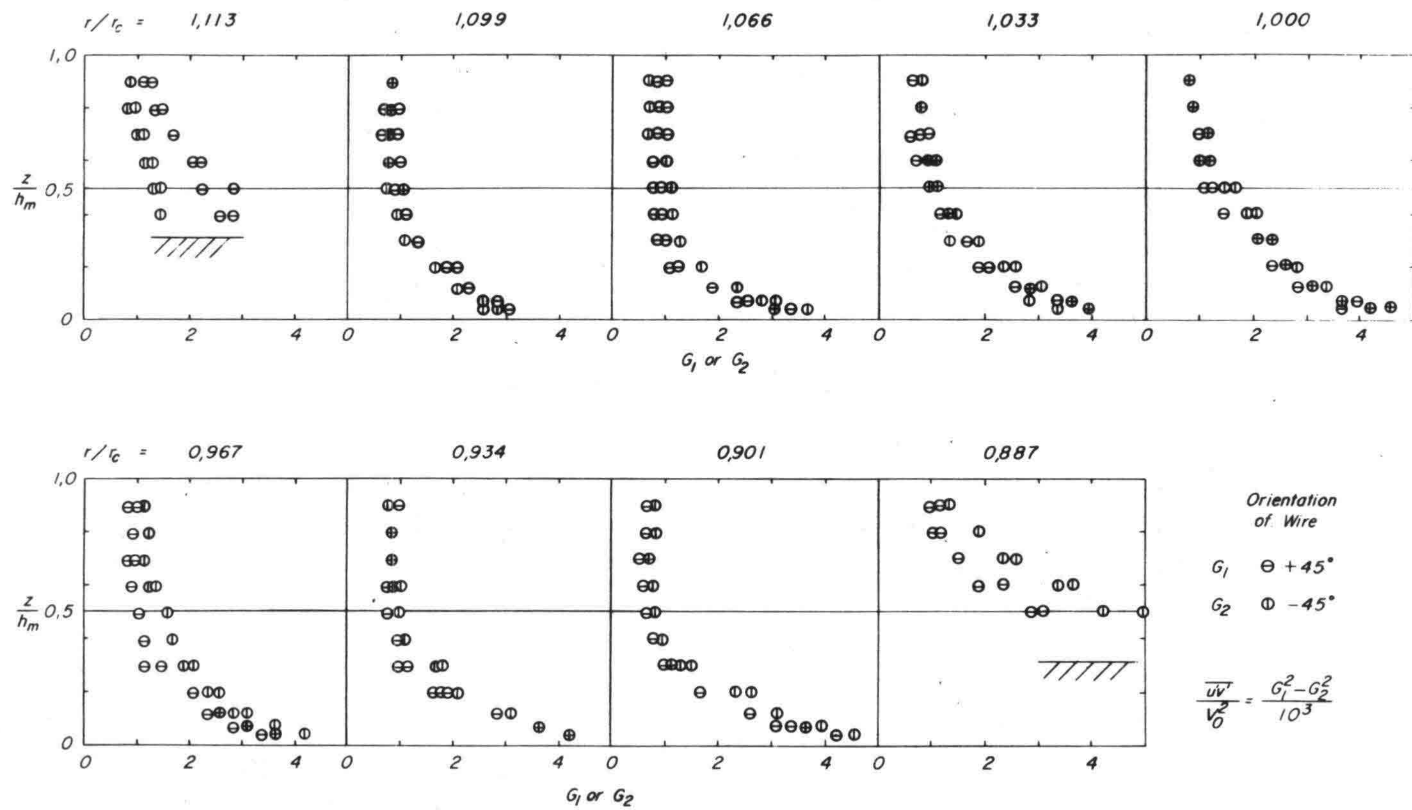

Fig, 24 Measurements of Turbulent Shear $\overline{u'v'}$ at Section CIIO

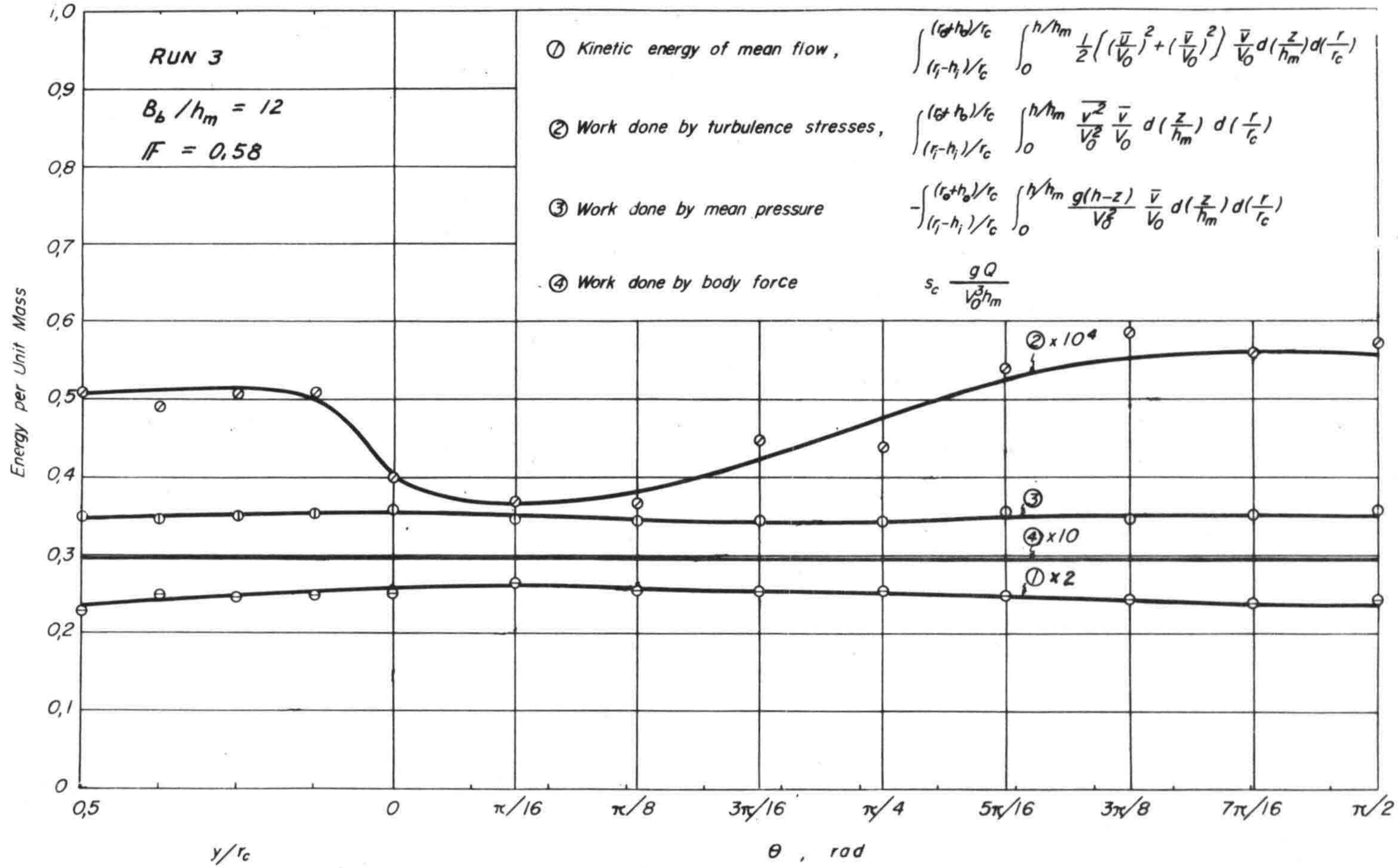

Fig. 25 Evaluation of Work Energy Relationship according to Eq.(57)